IMPERIAL COLLEGE LONDON

MICROMECHANICAL STUDY OF RECRYSTALLIZATION IN ALUMINIUM ALLOYS

By

Qinmeng Luan

Department of Mechanical Engineering

South Kensington Campus

Imperial College London

London SW7 2AZ

U. K.

A thesis submitted for the degree of Doctor of Philosophy of Imperial College London

2020

Declaration of Originality

The entire content presented in this thesis is the result of my independent research in the past 40 months under the supervision of Dr Jun Jiang. I have provided appropriate references wherever required in the thesis.

Qinmeng Luan 22/06/2020

Copyright Declaration

The copyright of this thesis rests with the author (Qinmeng Luan). Unless otherwise indicated, its contents are licensed under a Creative Commons Attribution-Non Commercial 4.0 International Licence (CC BY-NC).

Under this licence, you may copy and redistribute the material in any medium or format. You may also create and distribute modified versions of the work. This is on the condition that: you credit the author and do not use it, or any derivative works, for a commercial purpose.

When reusing or sharing this work, ensure you make the licence terms clear to others by naming the licence and linking to the licence text. Where a work has been adapted, you should indicate that the work has been changed and describe those changes.

Abstract

An in-depth understanding of the recrystallization (RX) process in alloys to achieve an optimised microstructure is critical to manufacturing metal parts with superior properties. However, the prediction of the RX process under various processing conditions is still in its early research stage and becoming an urgent demand for both the manufacturing industry and scientific research.

Regarding this long-standing microstructure formation problem, deformation bands (DBs) formed in metals are known to contribute to the unsolved problems in the RX process by giving rise to the microstructural heterogeneities. Previous experimental transmission electron microscope (TEM) work has identified the type of DBs at the microscopic scale, showing the importance of understanding the slip activation for DBs. However, the exact mechanisms of how DBs are formed and lead the RX during the subsequent annealing still remain unclear.

Firstly, to clarify the mechanism of DBs formation, single crystal, multi-crystal, polycrystalline pure aluminium (Al) and commercial Al alloys, as well as their corresponding crystal plasticity finite element (CPFE) models, were deformed to explore the effect of grain orientation, strain level and neighbouring grains on the formation of DBs regarding the orientations formed in DBs and the distribution of DBs. It is demonstrated that slip band intersection of primary and secondary slip can constrain the lattice sliding but facilitate the lattice rotation for the formation of DBs including the boundary of DBs and its orientation. It is found that the impact of the above factors on the formation of DBs is caused by the slip field of primary slip. The activation of a sufficient amount of primary slip in grains would be crucial to the formation of a large amount of distinct DBs.

Next, to explore the effects of DBs on the grain nucleation and the subsequent grain growth, specimens were annealed to observe the RX process. Regarding the recrystallized (RXed) texture, it is noticeable that the orientations of nucleated grains nearby DB are originated from the orientation in DB. Regarding the nucleated positions, it is demonstrated that potential nucleation sites are more likely located in DBs in the comparison with the initial grain boundary. Regarding the rate of RX, the number of nucleated grains is found to have a strong positive correlation with the area fraction of DBs which would consequently affect the kinetics of the

grain growth in the deformed microstructure. All the above observations imply that the RX process is strongly controlled by the ensemble characteristics of DBs rather than the initial grain boundaries.

On the basis of the above experimental observations, an improved and validated numerical model that is capable of predicting the RX process was developed using a Kobayashi, Warren and Carter (KWC) phase-field model coupled with CPFE analysis. It has been validated by the Electron Backscatter Diffraction (EBSD) mapping that this model enables a reliable and accurate prediction of RX in terms of the incubation time for grain nucleation and the evolution of RXed grain structure and texture. The model provided by this work offers a versatile tool for the manufacturing industry to solve many long-standing problems in the microstructure formation.

Publications

8. Y. Xiong, **Q. Luan**, J. Jiang, **Understanding the effect of strain path on the deformation state in pure aluminium**, in manuscript.

7. **Q. Luan**, J. Jiang, **How would the deformation bands affect recrystallization in pure aluminium?**, under review at Acta Mater.

6. **Q. Luan**, H. Xing, J. Zhang, J. Jiang, **Experimental and crystal plasticity study on deformation bands in single crystal and multi-crystal pure aluminium**, Acta Mater. 183 (2020) 78–92.

5. **Q. Luan**, J. Lee, J.-H. Zheng, C. Hopper, J. Jiang, **Combining microstructural characterization with crystal plasticity and phase-field modelling for the study of static Fewer in pure aluminium**, Comput. Mater. Sci. (2019) 109419.

4. **Q. Luan**, J. Lee, Z. Zheng, J. Lin, J. Jiang, **Static recrystallization study on pure aluminium using crystal plasticity finite element and phase-field modelling**, Procedia Manuf. 15 (2018) 1800–1807.

3. **Q. Luan**, T.B.B. Britton, T.-S. Jun, **Strain rate sensitivity in commercial pure titanium: The competition between slip and deformation twinning**, Mater. Sci. Eng. A. 734 (2018) 385–397.

2. J. Jiang, P. Hooper, N. Li, **Q. Luan**, C. Hopper, M. Ganapathy, J. Lin, **An integrated method for net-shape manufacturing components combining 3D additive manufacturing and compressive forming processes**, in: Procedia Eng., 2017.

1. W. Li, Y. Liu, S. Jiang, **Q. Luan**, Y. Li, B. Gu, Z. Shi, **A study of thermomechanical behaviour and grain size evolution of AA7050 under hot forging conditions**, Int. J. Light. Mater. Manuf. (2018).

Conferences

3. <u>**Q. Luan**</u>, J. Lee, J. Jiang, **Phase-field modelling coupled with crystal plasticity theory on static recrystallization of pure aluminium**, Metal Forming 2018 (Toyohashi, Japan)

2. <u>**Q. Luan**</u>, J. Lee, J. Jiang, **Static recrystallization study: phase-field modelling and quasi-in-situ EBSD**, EBSD 2018 (University of Plymouth, UK)

1. <u>**Q. Luan**</u>, J. Jiang, **EBSD for the study of recrystallization**, EBSD 2017 Workshop (University of Oxford, UK)

Acknowledgement

格物致知   Study the nature of things to acquire knowledge.

------礼记·大学   *------The Book of Rites*

(770 BC-476 BC, 春秋)   *(770 BC-476 BC, Spring and Autumn period, China)*

First of all, I like to express my most sincere gratitude to my primary supervisor, Dr Jun Jiang, for his continued encouragement, endless patience and instant guidance. He is never too busy to help and is concerned for all his students both academically and mentally. From him, I have not only learned the academic knowledge, but also the spirit of being positive for any incoming problems. I would also like to express my deepest gratitude to my secondary supervisor, Prof Jianguo Lin, for his availability throughout the study, his insights on many complicated problems and the financial help towards the writing-up period. I also want to thank them for providing an inclusive, encouraging working atmosphere. I am glad to be a part of the great research groups − Novel Metal Forming group and Metal Forming group.

A special thank must be made of Dr Junyi Lee for the step by step help on the phase-field modelling, Dr Zebang Zheng for guidance in crystal plasticity modelling, Dr Vivian Tong for training me with many important skills on metal preparation. They are a constant source of help during my PhD study. Moreover, I would like to thank Dr Yan Huang from Brunel University who shared his valuable thoughts on my confusions when I was at the bottleneck of the research. To them, I give my deep appreciations.

I must thank all staff, technicians, my previous and current colleagues in the MoM group for their help, for creating a very enjoyable working environment, and for brightening many long days. I would also like to extend my thanks to members in office CAGB 488C, Dong Yang, Yang Zheng, Zhaoheng Cai, Jun Liu, Qunli Zhang, Yuhao Sun, Yuehan Liu, Qi Rong, Kailun

Glossary

Al	Aluminium
CPFE	Crystal plasticity finite element
DB	Deformation band
DIC	Digital image correlation
EBSD	Electron back-scattered diffraction
FCC	Face centred cubic
GND	Geometric necessary dislocation
GOS	Grain orientation spread
HAGB	High angle grain boundary
KAM	Kernel average misorientation
KWC	Kobayashi, Warren and Carter
LAGB	Low angle grain boundary
MC	Multi-crystal
ND	Normal direction
IPF	Inverse pole figure
ODF	Orientation distribution function
OM	Optical microscope
PC	Polycrystalline
RD	Rolling direction
RX	Recrystallization
RXed	Recrystallized
SC	Single crystal
SEM	Scanning electron microscopy
SIBM	Strain induced boundary migration
SF	Schmid factor
SFE	Stacking fault energy
SSD	Statistically stored dislocations

Contents

List of Figures

List of Tables

1 Introduction

1.1 Background and motivation

The required engineering properties for aeroplane components, such as high strength, high toughness and good fatigue resistance, are attributed to a designed microstructure with homogeneous small grains, minimum impurity segregation and a large amount of finely dispersed precipitates [1]. The recrystallization (RX) takes place during thermomechanical processing routes (TMP) to achieve the desired microstructures in final products [2,3]. Therefore, in order to optimize the microstructure and hence obtain specific material properties for structural alloys, it is vital to understand, predict and manipulate the RX process based on the understandings from experiments, physical concepts and computational models [1,3].

In the manufacturing industry, the capability to accurately control basic microstructural parameters during RX such as the evolution of RX fraction and grain size under the real-world processing conditions is in high demand [4]. If a computational model that is capable of accurately predicting the RX process is valid for the engineering manufacture, the understanding of microstructure control as well as its corresponding mechanical properties in structural components would be substantially advanced [4–6].

However, current models have limited accuracy when the alloy is changed and processing routes contain temperature gradients or complex strain paths. This is because the deformed microstructure and its relation to RX are not well understood by experiments [4]. Constructing a computational model on the basis of the experimental understandings on inhomogeneities in the deformed structure, therefore, becomes a vital topic in both science and engineering [7,8].

In the previous experimental work, most of the developed theories about RX are limited to qualitatively explanations of the RX mechanism, without further quantitative discussions on how the deformed structure affect the grain nucleation and the consequent grain growth [9]. For example, previous work focuses on discussing the general effects of various factors, e.g. strain level, grain boundary and initial grain size, on the occurrence of grain nucleation [10]. Although the analysis on nucleated orientations [11,12] and the nucleation conditions [13–15]

start to attract some interests nowadays, the quantitative criteria still need further rigorous examinations. This missing brick in the wall of RX study directly hinders the understanding of RX process as well as its simulations especially for the prediction of recrystallized (RXed) texture and RXed grain size.

In the previous modelling work, criteria for the grain nucleation are normally too simple and not directly validated by experimental findings [6,16,17]. For instance, the simulated nucleation sites are normally randomly chosen among the grit nodes [18] and the orientations of the nucleated grains are generally allocated by a stochastic process [18–21] which neither include the information of dislocation structure nor consider the orientation relationship between the nucleated and the initial grains. However, revealed by the microscopic observations, it is very rare to have homogeneous or even nearly homogeneous distributions of RX nuclei [9]. Even though some recent work has tried to include the dislocation structure and the misorientation relationship into the modelling, the assignment of the nucleated grains still needs further experimental support [22,23]. As a consequence, current RX models have limited usage in the manufacture due to the unknown relation between dislocation structure and RX.

Deformation bands (DBs) have been demonstrated to be crucial for the RX study. Compared with the other features of the deformation structure, such as slip bands which provide a high level of dislocation density, or initial grain boundaries which mainly provide orientation shifts, DBs are able to provide both the heterogeneous dislocation distribution and high orientation gradients regarding the crystallographic features. The amount of stored energy and orientation gradients formed in DBs would act as important prerequisites for the grain nucleation [11,22], thus affecting the RX rate, RXed grain size and RXed orientation eventually.

Furthermore, DBs which help the deformed structure to acquire new orientations could be critical to the prediction of RXed texture. In order to accurately predict the developed texture [4] after grain nucleation and grain growth, understanding the deformed texture, i.e. orientation formed in DBs, could shed some lights on the orientations in the nucleus during RX. For instance, in {100}<001> orientated silicon-iron single crystals, the recrystallized orientation kept the same with the orientation in the deformed structure which was {001}<210> [24]. Hence, it is extremely important to thoroughly understand the DBs in deformed microstructure for the prediction of RX regarding the RX kinetics and RXed texture.

This thesis aims to solve the unclear problems in the process of RX through understanding the fundamental mechanism of DBs formation and its quantitative effect on RX in aluminium alloys. This thesis also aims to improve the models for the microstructural evolution during deformation and annealing through combining the knowledge from experiments. This work can be applied to achieving a reliable prediction of the RX process in various alloys and thus controlling their mechanical behaviour through the design of processing, e.g. forging, routes. This will aid in the design of processing routes for the target microstructure and the improvement of the manufacturing efficiency, in the meanwhile of maintaining the good mechanical property for the structural components.

1.2 Outline of the thesis

The main contributions of this thesis are generally divided into four chapters as shown in Figure 1 with a clear logical flow. The first contribution serves as an essential prerequisite for the second contribution. The later two contributions validate the new findings and broaden the research from single crystal pure Al to polycrystalline pure Al and industry Al alloys.

Chapter 3 investigates the development of DBs in the single crystal (SC) and multi-crystal (MC) pure aluminium which is used as a basis for Chapter 4 to analyse the occurrence of RX. Chapter 5 not only validates the findings generated from Chapter 3 and 4 for polycrystalline (PC) pure aluminium, also couples the CPFE model and phase-field model to predict the RX process. Chapter 6 validates the findings of the effect of DBs on RX in PC commercial 7050 aluminium alloys used in aviation.

Chapter 2 first reviews the definition of RX and its classifications. The purpose of this chapter is to provide the reader with prior knowledge of the RX in alloys. The current progress and unsolved problems are introduced for later chapters.

Chapter 3 utilizes experimental EBSD study and micromechanical crystal plasticity modelling in mesoscale to provide new insights in understanding the mechanism of DBs formation. The CPFE model is validated by various aspects including the deformed specimen shapes, digital imaging correlation (DIC) technique and the slip trace analysis.

Chapter 4 combines EBSD mapping with KWC (Kobayashi, Warren and Carter) phase-field model to quantitatively explore the mechanism of how DBs affect the grain nucleation and grain growth. The criteria of grain nucleation at the existence of DBs from experimental EBSD observations are written into the KWC phase-field model for the simulation. Moreover, the simulated kinetics of RX process is validated by the experimental EBSD results.
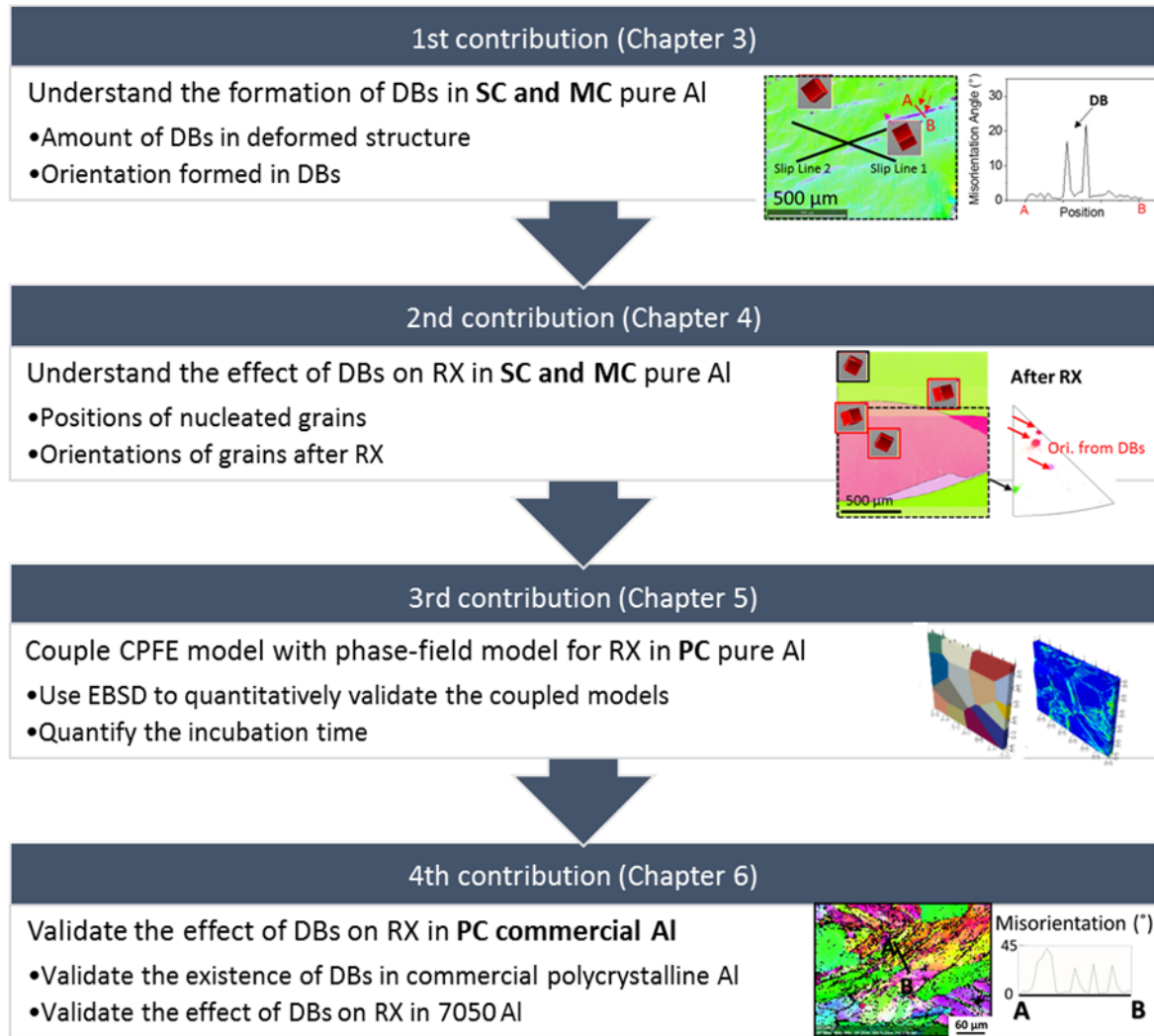
Figure 1 A flow chart showing the logical link between the four contributions of the thesis.

Chapter 5 couples CPFE model and KWC phase-field model to predict the RX process. Quasi-in-situ EBSD maps of the heat-treated polycrystalline pure Al specimen are used to quantitatively validate the simulated grain morphology evolution, texture evolution and the incubation time.

Chapter 6 validates the formation of DBs and its effect on the subsequent RX in commercial polycrystalline 7050 aluminium.

Chapter 7 summarises the new findings in the thesis and proposes future work.

2 Literature review

2.1 Theory and definition

Some 100 years passed after Kalisher used the term *recrystallization* (RX) for the first time in 1881, Doherty, Gottstein, Hirsch et al. [3] defined it in 1988 to describe the formation of a new grain structure in the deformed material by the formation and migration of high angle grain boundaries (HAGBs). The HAGBs are those grain boundaries with misorientation of the lattice >15° [25]. The driving force for the RX, i.e. HAGB migration, is from the stored energy reduction and minimization of surface energy [4].

The plastic deformation process introduces energy into the alloy in the form of dislocations, resulting in the formation of a metastable high energy state [3,25]. Apart from the RX, the other micromechanical process to reduce the stored energy of the system is recovery [3,25]. The process of recovery which occurs prior to RX reduces the energy through the diffusion of point defects to grain boundaries, the annihilation of dislocations or rearrangement of dislocations into lower-energy configurations such as dislocation walls with misorientation of $2°-5°$. These processes in recovery are achieved by glide, climb and cross-slip of dislocations in deformed grain [26], thus it does not involve long-range motion or the movement of high angle boundaries. It would partially restore the properties to their values before deformation. The recovery process has an effect on the nature and kinetics of RX. For example, recovery and RX are competing processes since both are driven by the reduction of dislocation density; the recovered subgrains usually act as the nuclei in the course of primary RX. The grain coarsening which occurs following RX is the process of grain growth driven by reducing the area of grain boundary during further annealing.

The RX could be divided into two steps, i.e. the formation and then the growth of a stable nucleus which are discussed in the following sections [3,27]. Both of the grain nucleation and grain growth involve the migration of HAGBs. The grain nucleation is driven by the reduction of stored energy (i.e. dislocation density) while the grain growth is driven by the reduction of HAGBs area.

2.1.1 Grain nucleation

It is well accepted that the nucleation sites of RX present in the deformed structure can become new grains and grow further once the necessary conditions, such as high angle misorientation and sufficient driving force, are achieved [3,9]. In this regard, the three best-known nucleation theories of RX are the migration of a pre-existing HAGB, the migration of low angle boundaries formed by recovery; and subgrain coalescence [9].

The nucleation by HAGB migration is also known as the theory of strain-induced boundary migration (SIBM), verified by Beck and Sperry [27]. In this mechanism, the minimisation of system energy is taken into account by the migration of pre-existing HAGBs toward the interior of a highly strained grain. As shown in Figure 2 a), grain A with low stored energy bulges into grain B with high energy. Hence, the energy reduction associated with the elimination in defects should be larger than the increase of total grain boundary energy due to bulging to initiate this mechanism [9].

For the theory of nucleation by the low angle boundary (i.e. subgrain boundaries) migration suggested by Beck [28] and Cahn [29], subgrains are capable to grow at the expense of its neighbours by the migration of subgrain boundaries. The subgrain boundaries absorb dislocations during growth to increase their misorientation and energy until they transform into high angle grain boundaries (see Figure 2 b).

For the theory of nucleation by subgrain coalescence [30], two adjacent subgrains coalescent to form a new grain by lattice rotation (see Figure 2 c). The occurrence of any of these three mechanisms depends on the strain level, heat treatment temperature, stacking fault energy (SFE), subgrain size distribution and the distribution of subgrain misorientation [9].
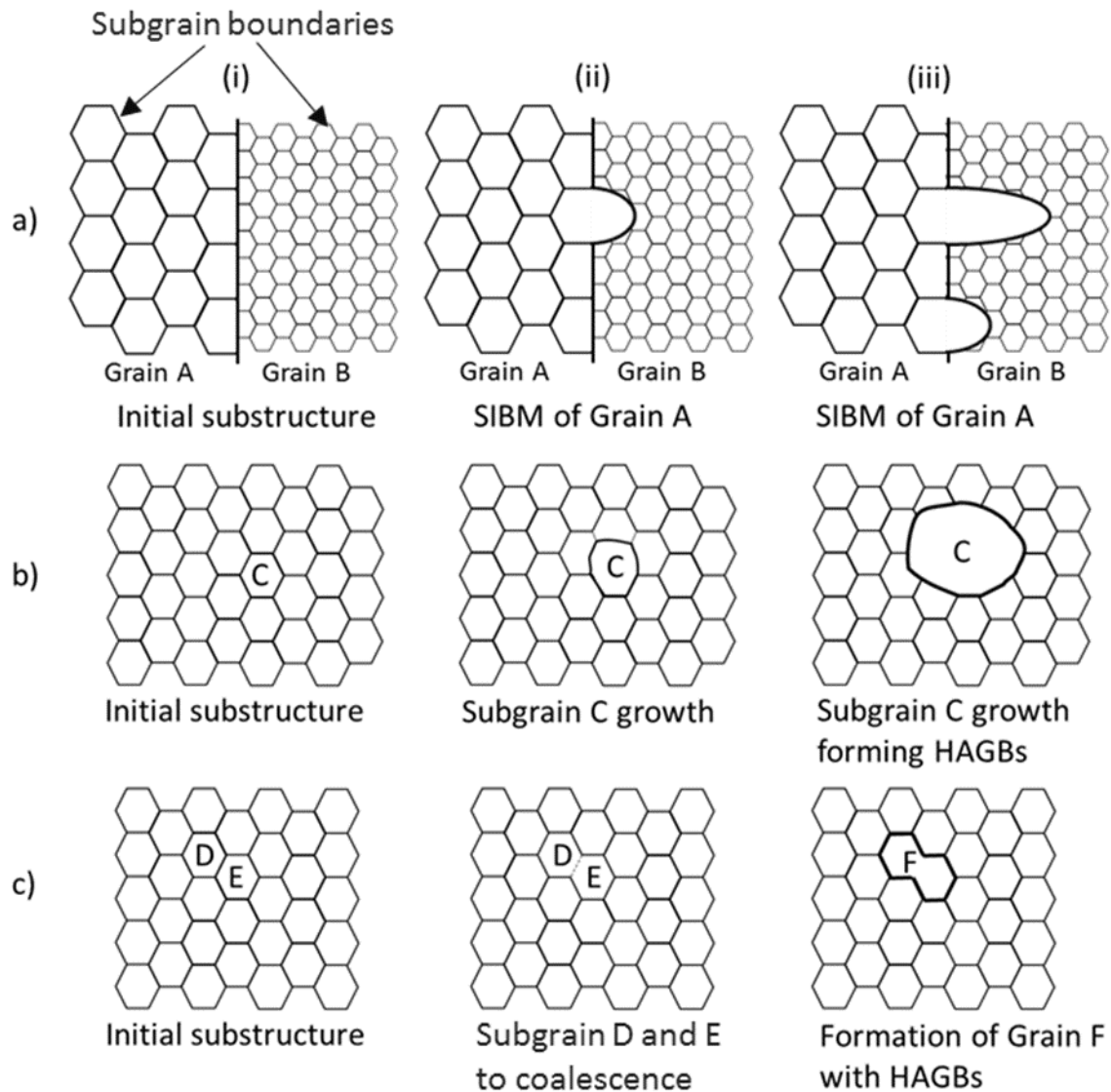
Figure 2 *Schematic representations of three nucleation mechanisms for a recrystallized grain (After Rios* [9]*). The sequence of (i)-(iii) in a) shows the nucleation by the migration of pre-existing HAGBs; b) shows the nucleation by subgrain boundary migration and HAGBs.*

2.1.2 Grain growth

The driving force of grain growth by the reduction of the grain boundary area, can be continuous (normal grain growth, i.e. primary RX) or discontinuous (abnormal grain growth, i.e. secondary RX) [31].

During normal grain growth, the smallest grains disappear resulting in a uniform distribution of individual grains size (see Figure 3 a)). During abnormal grain growth, some of the grains

grow rapidly and consume the matrix of smaller grains resulting in a bimodal grain size distribution (see Figure 3 b)) [25,31]. Unlike the grain nucleation driven by the reduction of stored energy, both of these two types of grain growth (i.e. coarsening) are driven by the reduction in grain boundary area during annealing [9,25].
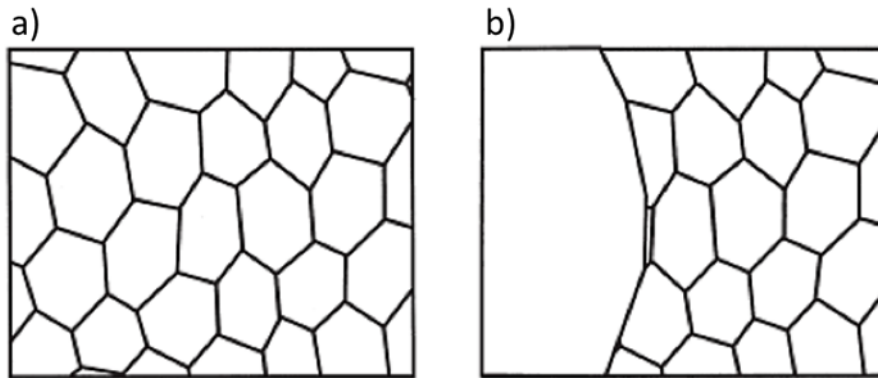
Figure 3 *Schematic of the a) normal grain growth and b) abnormal grain growth* [3]

2.2 Deformed microstructure

RX of a deformed structure involves a reduction of stored energy and a corresponding change of microstructure. It is obvious that the development of RXed microstructure is controlled by the formation and growth of nuclei, while both are dominated by the dislocation density distribution and heterogeneities of the deformed structure. Deformation heterogeneities are regions that contain a larger amount of crystalline defects and show a larger variation in lattice orientation. The larger number of defects in these regions create preferential sites for the formation of "potential nuclei" or "embryos".

As a result, in order to understand and predict the microstructural evolution during RX and grain growth, it is essential to examine the heterogeneities in the deformed state [3].

2.2.1 Dislocation structure

2.2.1.1 Slip, slip line and slip band

A basic deformation method for cubic metals is a **slip**. The slip always occurs on the most closely packed planes (i.e. slip planes) and in most closely packed directions (i.e. slip directions), which is also known as the slip system, e.g. {111}<110> for FCC alloys.

Slip line is a numerous surface step caused by dislocations propagation along the slip plane in the slip direction [32] that can be observed on the surface of the plastically deformed single crystal specimen (see Figure 4 a)). The Burgers vector of these dislocations are all parallel to the slip plane [32] (see Figure 4 b)).

Slip bands are localized aggregate of parallel slip in individual grains whose orientation is affected by the orientation of the grain. Thus, slip bands cannot across the grain boundary [32].
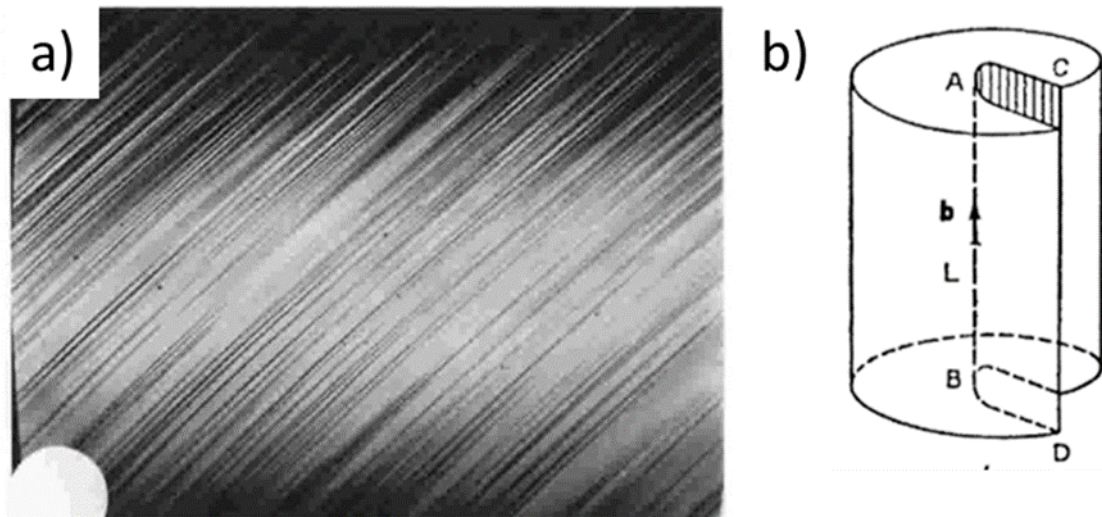
Figure 4 a) Slip lines on plastically deformed aluminium (after Jaoul); b) screw dislocation at position B [32].

2.2.1.2 Deformation band

The term **deformation band** (DB) defined by Barrett et al. [33] in 1939 describes a volume of approximately constant orientation that is significantly different to the orientation elsewhere in that grain (shown in Figure 5 c)). With the help of Digital Image Correlation (DIC) technique for the measurement of the strain distribution on surfaces, it has been demonstrated that DBs have concentrated strains giving rise to orientation gradients and eventual fragmentation of grains [3]. Same with the slip band, DB is determined by the crystallographic nature of the deformation process [3].

The edge of the DB, such as the area with orientation changes from B to A in Figure 5 c), may have a finite width which is known as the **transition band** [34]. It becomes a deformation-induced grain boundary if the orientation change is sharp.
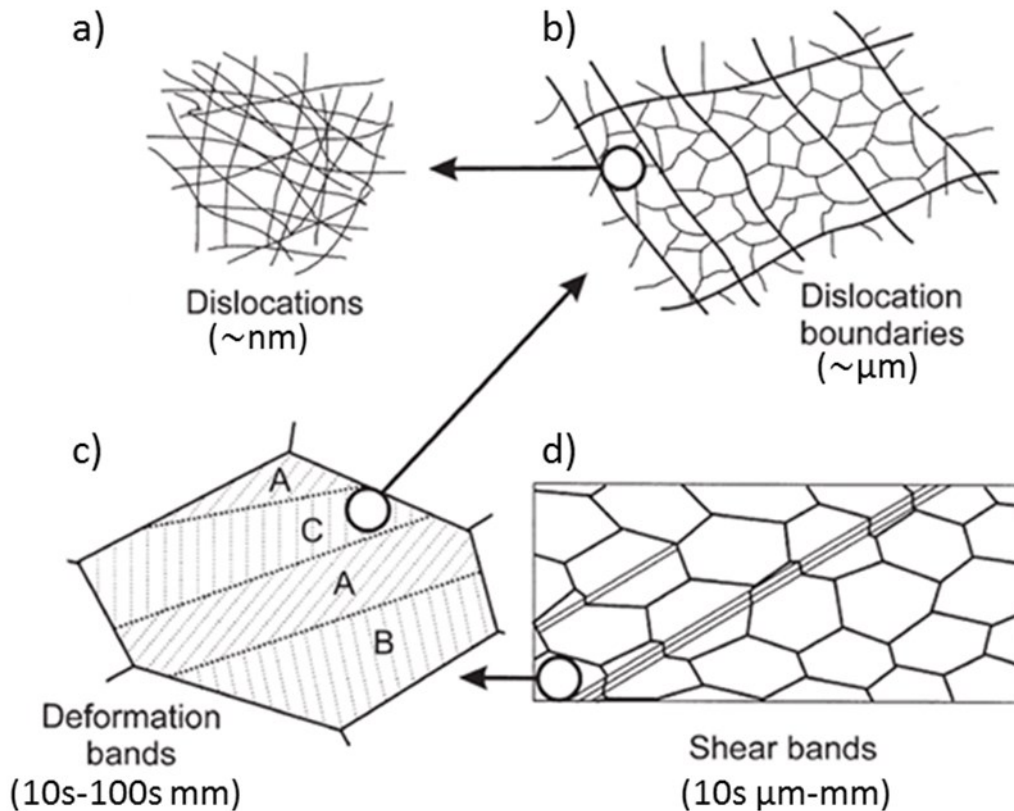
Figure 5 *The various features in a deformed polycrystalline metal at increasing scale: a) dislocations; b) dislocation boundaries; c) deformation and transition bands within a grain; d) specimen and grain-scale shear bands* [3].

The formation process of two kinds of DBs, i.e. kink bands and bands of secondary slip, was identified by etch pit tests and Laue back-reflection method with an X-ray beam in face centred cubic crystals (FCC) in tension in the 1990s by Higashida et al. [35]. These dislocation structures of two kinds of DBs observed by etch pit technique have an excellent agreement with the observations by transmission electron microscope (TEM) [36,37] and X-ray topography.

The **kink band** is found to be a wall perpendicular to the primary slip direction (see Figure 6 a)) and the **band of secondary slip** is a zone approximately parallel to the primary slip plane (see Figure 6 b)) in which secondary slip are operating more actively than the primary slip [35]. Kink bands and bands of secondary slip are transmuted from the local bend-gliding regions and the coplanar slip zones of primary slip respectively.
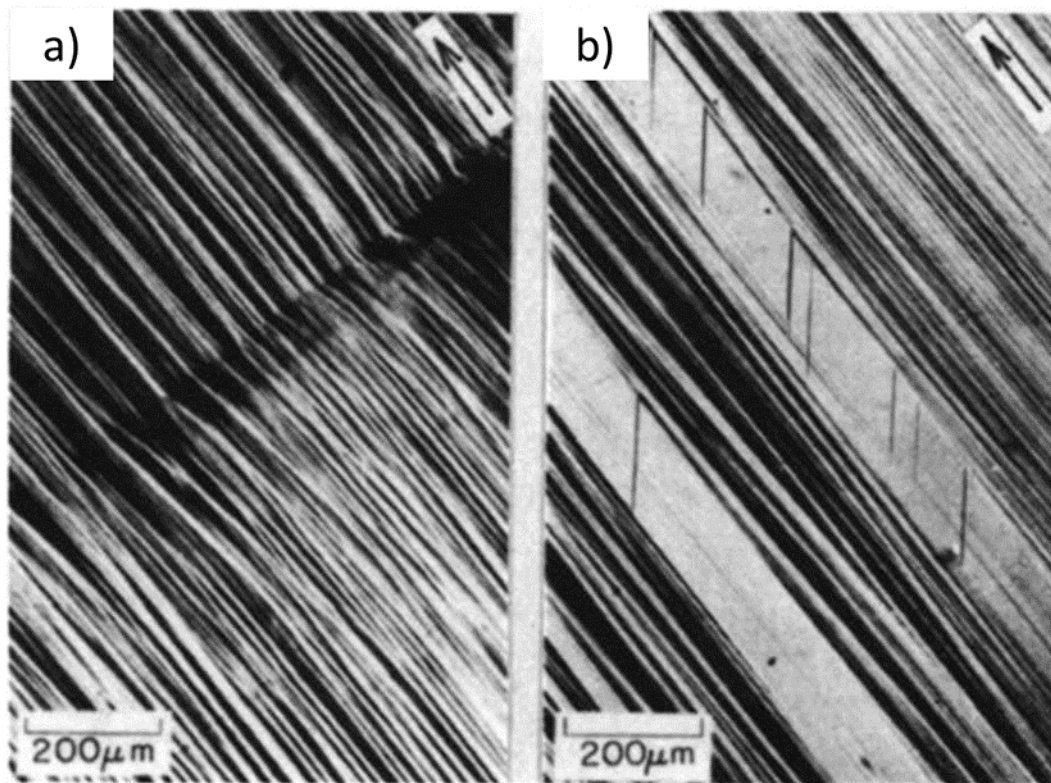
Figure 6 *Deformation bands in an as-deformed Cu-1at.%Ge alloy crystal initially oriented near [321] (shear strain = 40.4%): a) kink band; b) band of secondary slip. The arrows indicate the direction of the primary slip system.*

The stress-strain curves of single crystals can be divided into different stages [3,35,38,39] to study the formation of DBs (see Figure 7 d)). Stage I indicates that only the primary slip are activated for the single crystal that undergoes easy glide. Stage II indicates that the secondary slip are activated. The transition from stage I to II is found to be accompanied by noticeable structure changes including the onset of secondary slip and the formation of deformation bands [35,40].

An example of the formation of kink bands, as well as the generation of forest dislocations, is shown in Figure 7 a)-c) for single crystal copper deformed by different amounts of uniaxial tensile strain up to early stage II. It is notable that the rapid generation of forest dislocations at early stage II is very likely correlated with the formation of kink bands as defined in Figure 7 b) to c), which is accompanied by the sudden activation of secondary slip [35].
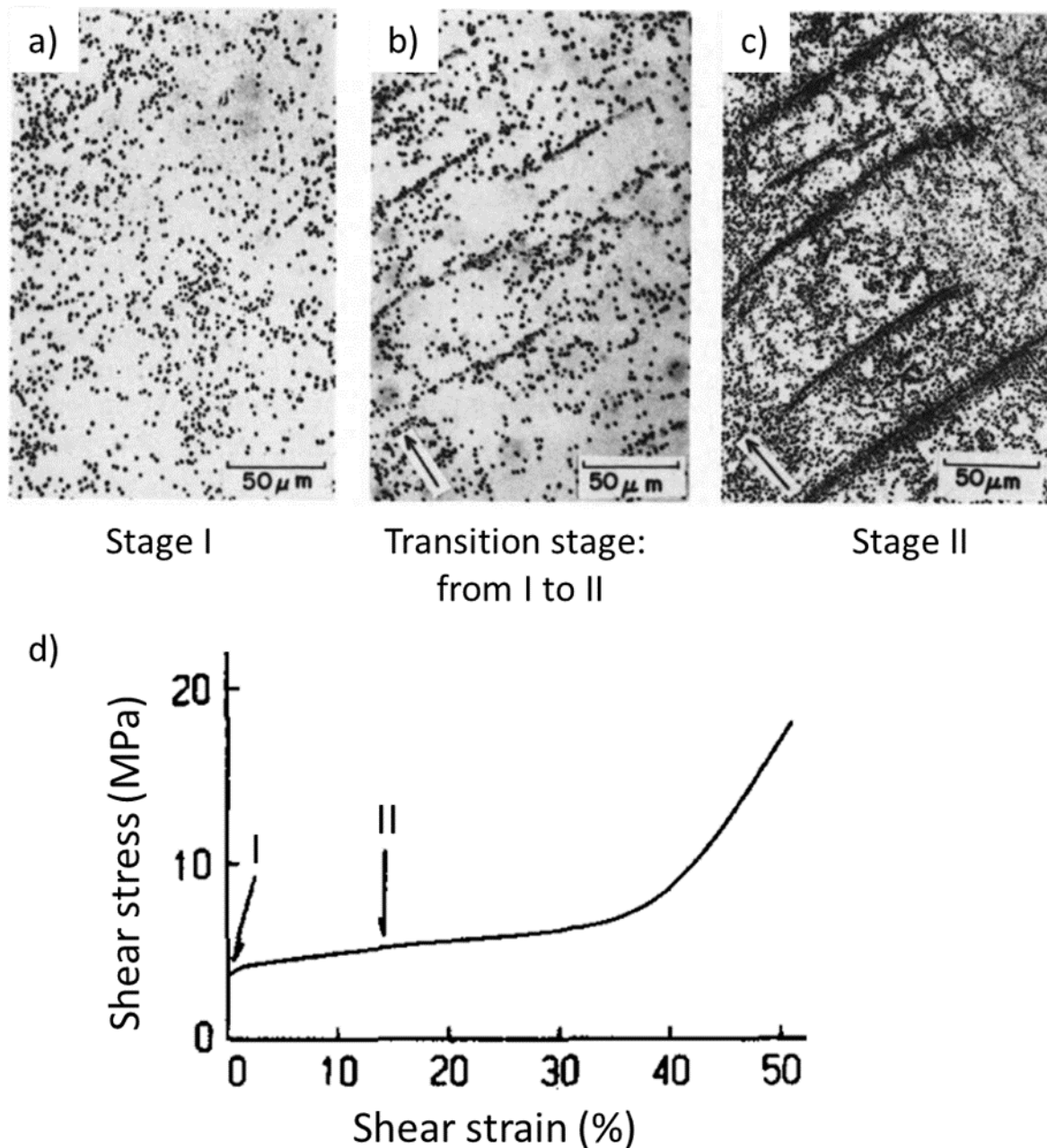
Figure 7 Etch pits on image a)-c) reveal the activation process of forest dislocations at kink bands on the primary plane in copper crystals oriented near [321]: a) early stage I (shear strain = 2.2%); b) transition Stage from I to II (shear strain = 5.0%); c) early stage II (shear strain = 8.3%). The arrows indicate the direction of the primary slip system. d) The stress-strain curve in a Cu-1at.%Ge alloy crystal.[35]

According to the previous study on the generation of DBs [34,35], at least three cases listed below are needed to be considered:

a) **Kink band walls:** Once kink band walls are built up, secondary slip are triggered at the walls due to the stress concentration caused by primary slip piled up against the walls.

b) **Additional stress field:** On building up the kink band walls, additional stress arises on the coplanar slip system, giving rise to long-range stress fields. As a consequence, secondary slip are activated in the coplanar slip zone, transforming it into a band of secondary slip.

c) **Stress of dipolar arrangements of primary dislocations:** These stresses are relieved by forest dislocations in the matrix between kink bands.

The formation of DBs, as well as the initial grain orientations, are relevant to the generation of deformation textures. The grain orientation is a dominating factor for grains either to be deformed homogeneously or deformed into fragments by DBs [3]. For instance, the {110}<001> Goss orientation in FCC material is found quite stable under compression in both single crystal and polycrystals with large grains without forming an extensive amount of DBs [3]. As a result, it has been found that RX is hard to occur in the **Goss** orientated grain (as shown in Figure 8). The orientation information for important texture components in rolled FCC metals is shown in **Table 1** and plotted in an orientation distribution function (ODF) map in **Figure 9**.
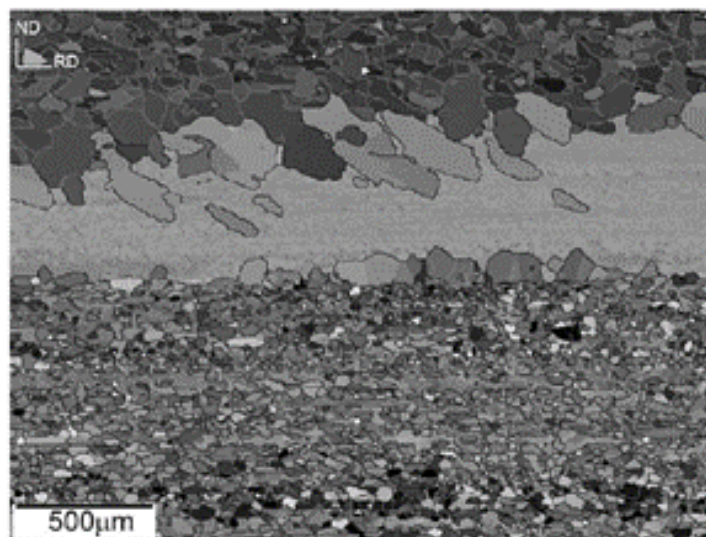
Figure 8 *EBSD map of a partially RXed cold-rolled, coarse-grained Al-0.05 wt.% Mn alloy. The area originally contained three deformed grains. The upper and lower grains have recrystallized to different grain sizes, whilst no RX has occurred in the central (Goss-oriented) grain* [3].

Table 1 *Important texture components in rolled FCC metals* [3].

Component	{hkl}	<uvw>	ϕ_1	Φ	ϕ_2
Copper	112	111	90	35	45
Goss	011	100	0	45	90
Brass	011	211	35	45	90
Cube	001	100	0	0	0
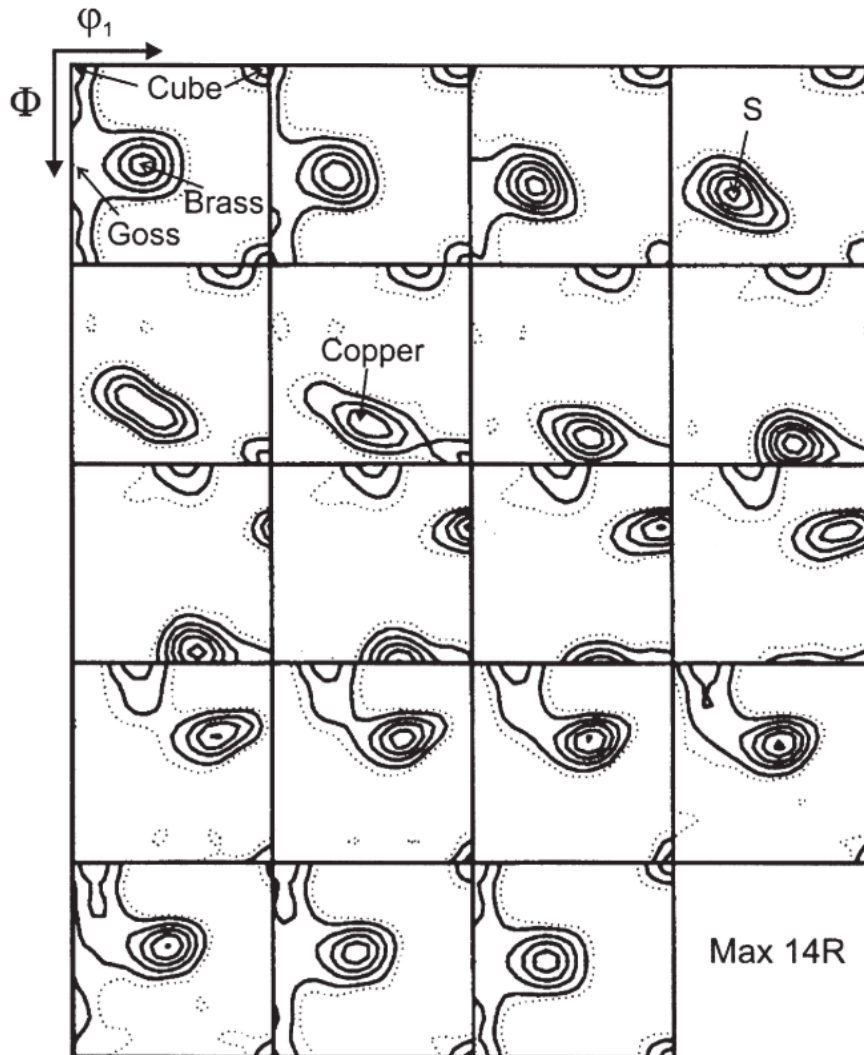
Figure 9 *ODF of 90% cold-rolled aluminium showing the positions of some important texture components in Table 1* [3,41].

2.2.1.3 Shear band

Unlike slip bands and deformation bands, the formation of **shear bands** follows non-crystallographic directions. Hence, shear bands are independent of crystallographic considerations and can cross existing grain boundaries. In rolled alloys, they normally occur at ~35 degrees to the rolling plane and parallel to the transverse direction.

Shear bands are characterised by non-crystallographic bandlike narrow regions of highly concentrated flow while the abutting matrix undergoes comparably low and homogeneous plastic flow [42]. As a result, intense shear is always found in shear bands providing both extensive amounts of dislocations and orientation gradients for the occurrence of RX [3].

It has been demonstrated in previous literature that the formation of shear bands is promoted when homogeneous slip are inhibited or when the number of crystallographic slip systems is insufficient. In such cases, shear banding acts as an alternative mesoscopic deformation mode, often associating with a sudden drop in the local flow stress. Such that, shear banding is recognised as a softening mechanism [43].

2.2.2 Deformation texture

The orientation changes caused by most favourably orientated slip or twinning are not random, thus, a preferred orientation or texture would be formed in the deformed structure which is named as **deformed texture**. During the subsequent annealing, nucleated grains would nucleate in the deformed microstructure having certain orientation relationships with the deformed texture. The ability of the nuclei to grow would also be affected by the orientation relationship between the adjacent regions in the microstructure. Therefore, it is essential to understand how the deformed texture is formed and how it affects the RXed texture for the prediction of the RXed texture development in the course of grain nucleation and grain growth. The factors could affect the deformed texture are discussed in the sub-sections below.

The change of orientations during the plastic deformation is relevant to the activation of slip systems and the amount of slip occurring on each system which is an integrated behaviour of the initial grain orientation, crystal structure, the strain level and the geometry of the deformation process [3]. Factors affecting the deformation texture are discussed and summarised below:

a) **Orientation effect:** An example of the initial orientation effect on the deformation texture would be the formation of DBs. As mentioned in Section 2.2.1.2, some orientations will alter significantly during deformation and form DBs while some (e.g. **Goss**-oriented) grains will not.

b) **Geometry of the deformation process:** The geometry of the deformation process is also found to be crucial for the formation of deformation texture. For instance, in the

rolled copper-manganese system, a significant formation of shear bands and the development of a strong **Brass** component (check Table 1 and Figure 9 for more information) were reported by Pfeiler [44] and Engler [45]. By contrast, it was not observed such deformed texture after uniaxial compression. Therefore, the geometry of the deformation process is important for the study of deformation texture which affects the boundary conditions of loading and the yield stress [3].

c) **Stacking fault energy effect:** In FCC alloys, the stacking fault energy (γ_{SFE}) has been found to be a crucial factor for the formation of deformed textures. In this case, the deformation mode is the same for both alloys (i.e. {111}<110> slip system), but the stacking energy varies in the different alloys. For example, the rolling texture of FCC alloys with high γ_{SFE}, such as aluminium with $\gamma_{SFE} \sim 170$ mJ/m^2 and copper with $\gamma_{SFE} \sim 80$ mJ/m^2, is very similar to that of Figure 10 a). By contrast, the rolling texture for the metals with low γ_{SFE}, such as 70:30 brass, austenitic stainless steel or silver with $\gamma_{SFE} < 25$ mJ/m^2, is similar to that of Figure 10 b).
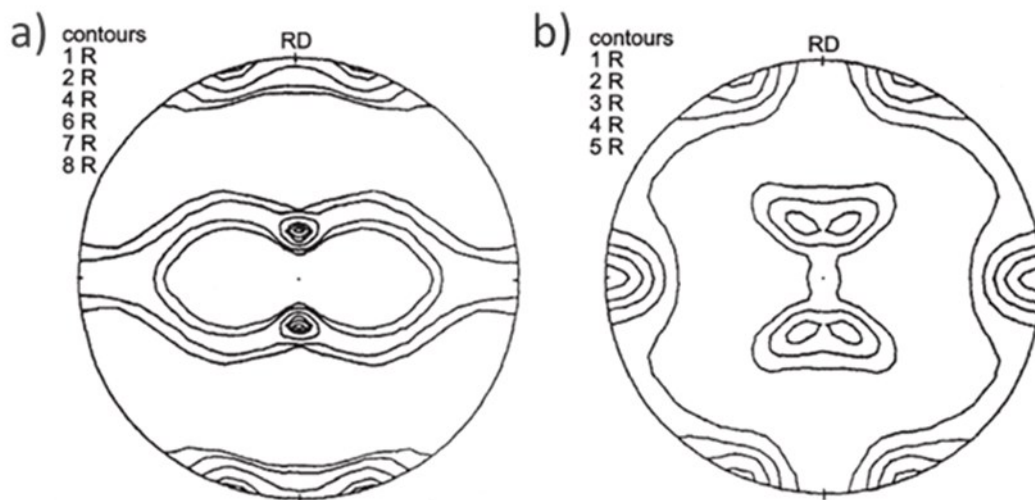
Figure 10 *{111} Pole figures of 95% cold-rolled FCC metals: a) copper; b) 70:30 brass* [3].

d) **Shear banding effect:** The formation of shear bands could change the deformation texture by causing rotation of the material about the transverse direction. Overall, shear banding represents an inhomogeneous characteristic of deformation and thus tends to weaken the texture [3]. In FCC metals with medium to high γ_{SFE} such as aluminium alloys, shear banding may occur when the material has extensive solid solution

hardening [46] or deformable second-phase particles [47]. Particularly, the texture component **Copper** in FCC metals is weakened and the **Brass** and **Goss** components strengthened by shear banding under the plane strain compression [3].

2.3 Current understandings of RX

2.3.1 Conditions and energy for recrystallization

RX can only occur when the following three conditions are satisfied [48]:

a) **Critical dislocation density:** The adequate plastic deformation is required to generate sufficient dislocation density (i.e. stored energy) to drive the grain nucleation and grain growth. This is the main driving force for RX to occur [9].

b) **Critical temperature:** A minimum temperature is required at a certain level of dislocation density for the occurrence of RX. For dynamic RX, the critical temperature is normally $>0.6T_m$. For static RX, the critical temperature decreases with the stored dislocation density and allocated annealing time.

c) **Incubation time:** A minimum annealing time is required for new grains to nucleate at the high energy sites in the heterogeneous deformed microstructure. The incubation time can be reduced by increasing the stored dislocation density and/or the annealing temperature.

Once the stable nucleus formed, RX, as discussed in Section 2.1, is then controlled by the migration of HAGBs. The HAGBs would migrate over the strained matrix (non-RXed area) removing the crystalline defects (i.e. dislocations mainly) until RXed grains meet mutually [9].

The forces that act on a HAGB can be understood as "pressures" applied to it with [J/m^3] or [N/m^2] units. The main forces are: driving force due to straining, grain boundaries and discontinuous precipitation; retarding forces due to solute atoms and precipitated particles.

The driving force due to stored dislocations is given by

$$F_N = \frac{1}{2} G \cdot b^2 \cdot \rho \qquad (1)$$

where G is the shear modulus and b is the modulus of the Burgers vector and ρ is the stored dislocation density.

The driving force due to the grain boundaries which is the main driving force for the grain growth can be expressed by the surface energy (γ) associated with GBs with average diameter D as following

$$F_{gg} = 2\gamma/D \qquad\qquad (2)$$

The driving force due to discontinuous precipitation and retarding force due to precipitates and solute atoms are avoided in this work for discussions. More details can be found in reference [3] and [9].

2.3.2 Factors affecting the RX kinetics

The **deformation mode** has an effect on the rate of RX, for instance, single crystals that are deformed in single glide (e.g. that in Figure 11) and recovered during annealing may not recrystallize. The dislocation structure which does not contain the heterogeneities and orientation gradients cannot provide nucleation sites during annealing [3].
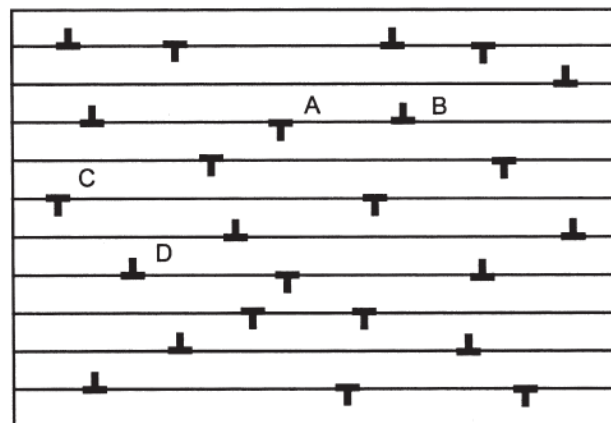
Figure 11 *Schematic of edge dislocations in a deformed crystal* [3].

As discussed for deformation mode, the heterogeneous deformed microstructure and stored energy distribution depend strongly on the activated slip systems and deformed orientation [3]. Hence, the **crystal orientation** is found to affect the RX rate and RXed orientation through changing the deformation mode and the deformed texture.

An example is shown in Table 2 for silicon-iron single crystals done by Hibbard and Tully in 1961. It has been found that the single crystals of various orientations which were all cold rolled 80% are significantly different in RX rates. The general conclusions for the different rates are explained by the stored energy after deformation which relates to the crystal

orientation. It is also clearly seen in Table 2 that the orientation after RX is associated with the deformed orientation which was originated from the initial orientation, such as the first two samples in Table 2.

Table 2 Recrystallization of 80% cold rolled silicon-iron single crystals at 600 °C [24].

Initial orientation	Final orientation	Time for 50% recrystallization (s)	Orientation after recrystallization
{111}<112>	{111}<112>	200	{110}<001>
{110}<001>	{111}<112>	1000	{110}<001>
{100}<001>	{001}<210>	7000	{001}<210>
{100}<011>	{100}<011>	No recrystallization	{100}<011>

The prior **strain level** also has an effect on the number and type of effective nucleation sites as it alters the deformation mode of the crystals which would contribute to the amount of stored energy and orientation gradient after deformation. An example of the effect of strain on the RX kinetics and RXed grain size is shown in Figure 12 a) and b) respectively. The higher the prior strain level is, the faster the RX and the smaller the RXed grain size would be.
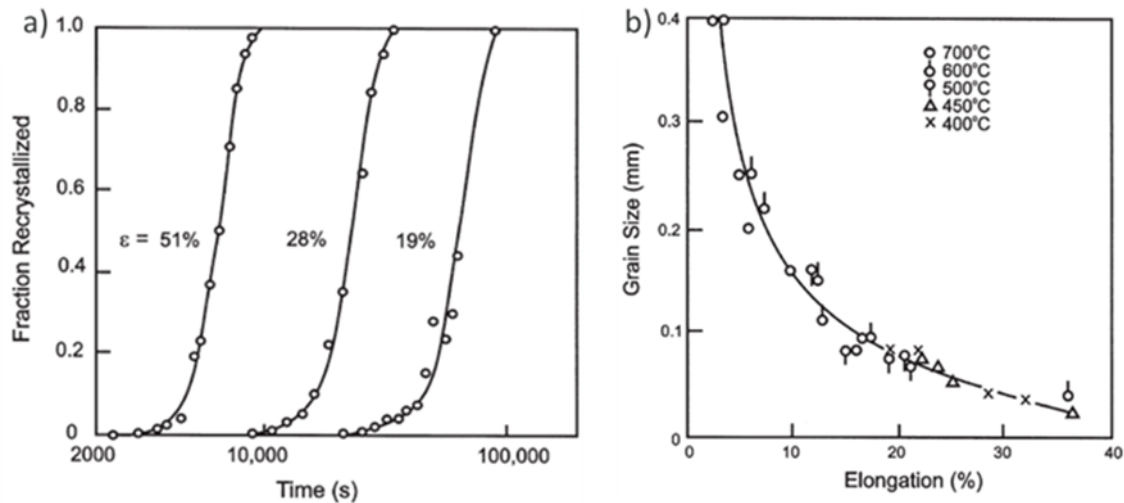
Figure 12 The effect of tensile strain a) on the RX kinetics of aluminium annealed at 350 °C; (b) on the final grain size in α-brass RXed at various temperatures [3].

During the heat treatment, the increase of **annealing temperature** accelerates the RX kinetics (see Figure 13). The heating rate to the annealing temperature also influences the RX rate by governing the competition between recovery and RX process. It is expected that in pure metals, boundary migration controls RX and lattice diffusion controls recovery. Normally, a low

heating rate would promote RX by suppressing recovery in pure metal [3]. Furthermore, the phase transformation of precipitation may occur before RX and hinder it.
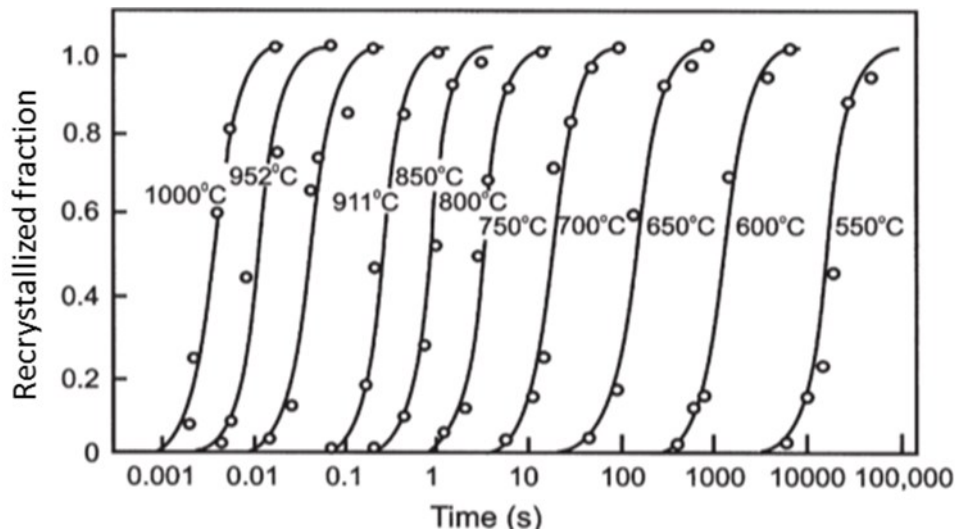
Figure 13 *The effect of annealing temperature on the RX of Fe-3.5% Si deformed 60%* [3].

Strain path, that controls the deformation, is always complex in the standard industry which could be a combination of uniaxial compression, channel-die, plane strain compression, tension, torsion, forging and rolling [25]. It has been demonstrated by experiments that the strain path has an impact on the deformed microstructure and its subsequent RX behaviour.

The experiments to study the strain path effects are simplified and carried either in the reversal of strain path (e.g. tension-compression and torsion-reverse-torsion) or in multiaxis loading compared with uniaxial loading. The specimens used for comparison are normally deformed to the same total permanent strain or the same stress [3].

It has been found that the specimen, at the same total strain level, under a complex strain path normally requires higher RX temperature and longer annealing time. As shown in Figure 14, Lindh et al. [49] noticed that the specimens under the reversal of the strain path (i.e. combined tension and compression) were found to require a higher RX temperature than the specimen under tension solely.
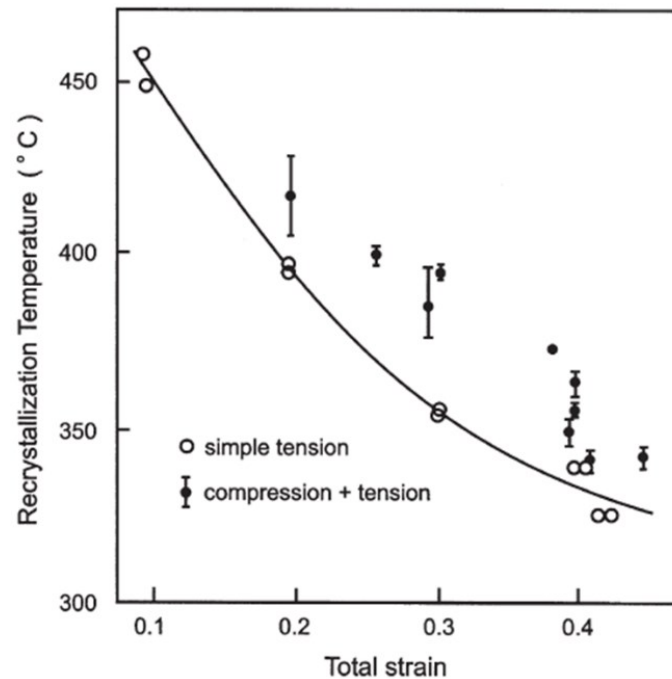
Figure 14 *The RX temperature of copper as a function of the total applied strain in specimens deformed by tension or by a combination of tension and compression* [49].

A similar case is found by Embury et al. [50] (see Figure 15 a) that the specimens which were multiaxis compressed to the same equivalent strain (0.7) recrystallized more slowly than the uniaxial deformed specimens. However, for specimens which were deformed to the same equivalent stress, the RX kinetics for uniaxial compression were similar with the multiaxis compression (see Figure 15 b))[50].

To explain the slower RX rate caused by multiaxial compression, a simple interpretation has been proposed that the development of orientation gradients could partially uncompleted due to the reversal in the strain path. As a result of the decreased orientation gradients, fewer nucleation sites are formed contributing to a slower RX rate and a larger RXed grain size [3]. However, the effect of the strain path on the formation of orientation gradients, as well as the dislocation structure, still need further investigations for the understanding of the effects of redundant deformation on the microstructure [3].
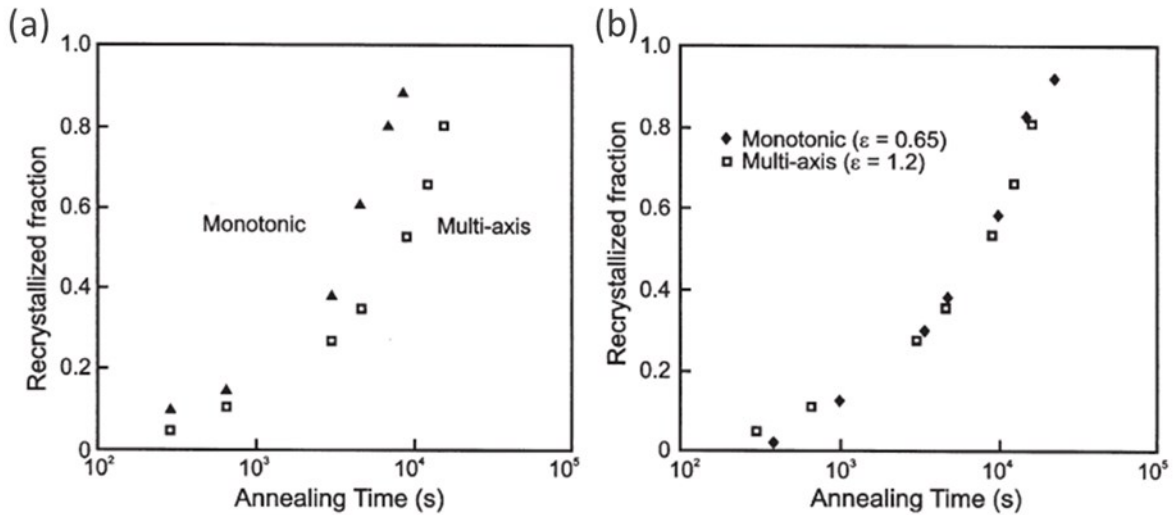
Figure 15 *The RX kinetics for specimens deformed monotonically compared with those of multiaxial deformed specimens: a) specimens deformed to the same equivalent strain (0.7); b) specimens deformed to the same equivalent stress* [50].

To summarise, the kinetics of RX process is controlled by the thermomechanical processing factors that are able to manipulate the stored dislocation density and affect the development of orientation gradients in the deformed microstructure.

2.4 Modelling of recrystallization

2.4.1 Kinetics of recrystallization

Under isothermal conditions, RX generally shows an incubation time for the formation of nuclei and completion when the recrystallized grains meet mutually [9]. The classic John-Mehl-Avrami-Kolmogorov (JMAK) [51–54] equation has been widely used to predict the overall kinetics of primary RX in deformed metals. The RX fraction X is described by the equation $X = 1 - \exp(-kt^n)$, where $X = 0$ is for the onset of RX and $X = 1$ is for the fully recrystallized material, t is the time, k and n are commonly referred to as the Avrami coefficient and Avrami exponent. In theory, n is equal to 4 if the RX nuclei are randomly distributed, the nucleation rate is constant during annealing, the growth rate is isotropic in three dimensions, and the growth rate of the nuclei remain constant during growth [25]. If the nucleation is site saturated and growth is isotropic in two dimensions [6], then n is equal to 2.
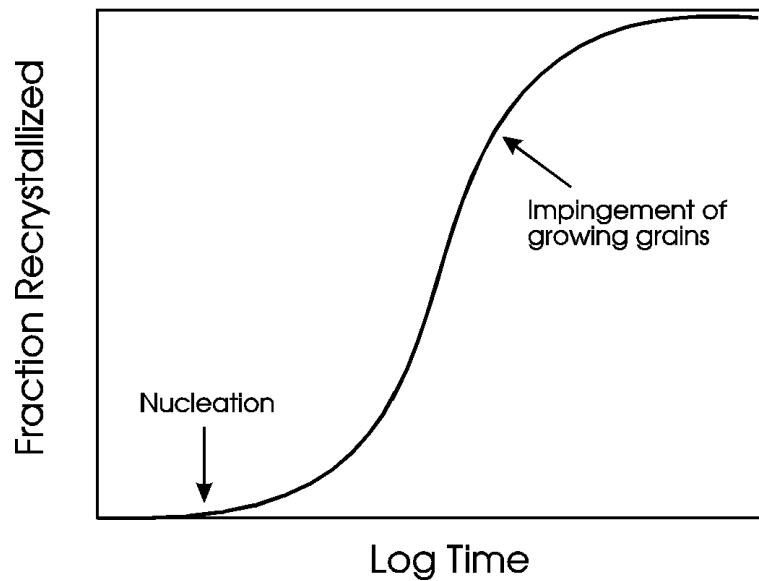
Figure 16 *Typical features of nucleation and growth kinetics of recrystallization* [3].

2.4.2 Crystal plasticity theory

The initial deformation state for the phase-field modelling can be obtained from microstructure characterisation (e.g. EBSD mapping) and deformation state modelling (e.g. crystal plasticity finite element (CPFE) simulations) [55,56].

The CPFE model [57–59] used herein is able to predict the deformation heterogeneities (e.g. phase interfaces, grain boundaries and their triple points) through coupling the dislocation density with slip rules [60]. CPFE simulations can help to identify the heterogeneous distribution of nucleation positions and nucleated orientations in the KWC phase-field model [20]. Similarly, the recrystallized microstructure generated by the phase-field model can be imported into the finite element model to predict the mechanical behaviour of the alloy.

2.4.3 KWC phase-field model

The computational model used in this work to study primary RX is the KWC phase-field model proposed by Kobayashi, Warren and Carter [61]. The energy term in the KWC phase-field model is developed as functions of variables and their gradients, aiming to minimise the total free energy of the system. The microstructural evolution at mesoscale is simulated by two variables, the conserved variable (i.e. phase η) and the non-conserved variable (i.e. grain orientation θ) [62]. The diffuse-interface approach implemented in this thesis, instead of the sharp-interface approach, allows the evolution of arbitrary complex morphologies to be

predicted without making any presumptions on the shape of grains [4,22,63]. In the diffuse-interface approach, the grain structure is represented by a set of variables that are continuous in space and time. Within the grain, the phase-field model variables have the same values. At the grain interface, these variables vary continuously over a narrow range between their equilibrium values in the neighbouring grains [63].

To simulate the grain nucleation at particular sites [3], the KWC phase-field model incorporates separate analytical models into the simulation. In terms of computational effort, it is not feasible to simulate nucleation and grain growth at the same time, as an extremely fine resolution and time step over the whole grain structure are required to catch the occurrence of nucleation [62,63]. Furthermore, it is physically rational to simulate the nucleation and grain growth separately, as the RX is mostly site-saturated [9,64].

2.4.4 Comparison of models

Existing numerical methods to simulate the RX process include the continuum mechanical models and discrete methods such as Monte Carlo Potts model, cellular automata, vertex, phase-field and level set models [4]. The brief description of algorithms is made for each model in Appendix B. The features of existing models for the RX process are summarised in Table 3 and compared with the phase-field model as following.

The **Monte Carlo model** simulates the energy change of the system by reorientation the lattice site according to the switch of spin state from the origin [65,66]. Accepting the switch of spin state or not depends on a switching probability [67,68]. The **cellular automata model** simulates the microstructure evolution by dividing the domain into a grid of cells that have a set of variables to define the physical state [69,70]. The state of a cell is switched based on its previous state and its neighbourhood. The switching rule of cellular automata could be deterministic or probabilistic based on the probability criterion [70–72]. These two models are relatively easy to implement and capture many aspects of microstructure physics, thus, are widely used for studying the RX phenomena [20,70,71,73–76]. They also have high computational efficiency compared with the phase-field model, since the discrete algorithms suit well for the code parallelization. However, remedies for the phase-field model such as adaptivity of the discretization grid can help to reduce the computational time. Also, the limitations of these two models can be overcome by the phase-field model, such as the

interpretation of simulation length and time scale, the dependence on the underlying solution grid and the representation of grain boundary curvature [4].

The grain structure in the **vertex model** is defined by the position of grain boundary junctions and their velocities [77]. Thus, the vertex model is able to include the physical time scale and solve the grain boundary curvature by the representation of line segments, but additional numerical scheme regarding the topological changes has to be considered in the 3D problem [78].

The main concept of the **level set model** is to trace the position of a moving interface with time [79]. This model is able to represent the interface and its curvature, but unable to trace textural evolution. As the representation of sharp interfaces in this model requires a fine computational grid, the cost of computational time is added due to the adaptivity [4].

For the phase-field model, the representation of surface is better and the explicit tracing of interfaces is not required unlike the vertex method [4]. A wide array of microstructure processes can be considered through this model based on the thermodynamic formulations as a function of system energy [4,63].

Table 3 *Features of the computational models for RX process*

Models	Features	
Continuum mechanical models	**Pros:**	• Conveniently simulate the macroscopic structural behaviour. • Readily implemented as material models in existing finite element models.
	Cons:	• Less straight-forward to include microstructure parameters such as the grain orientation and re-orientation, i.e. the evolution of crystallographic texture. • The changes in microstructure in terms of grain nucleation, growth and consumption of grains cannot be captured. • The characteristic parameters of the microstructure such as grain size and dislocation density, are only available as homogeneous quantities within each defined element.

Models	Features	
Phase-field model	**Pros:**	• Able to simulate a number of different microstructure processes. • Capable of tracing arbitrary microstructure geometries, e.g. represent grains without the need of explicitly tracing interfaces. • With physical length and time. • Based on thermodynamic formulations.
	Cons:	• Code parallelization can be less efficient as discrete methods, but remedies such as adaptivity of discretization of the grid can reduce the computational time. • Less applicable in studies of texture evolution. • Could need significant computational effort.
Monte Carlo Potts model	**Pros:**	• The algorithm is versatile and flexible enough to represent many physical features and processes. • The numerical implementation is straight-forward. • Decent computational efficiency.
	Cons:	• The algorithm is influenced by the underlying lattice. • Lack of physical length and time scales.
Cellular automata model	**Pros:**	• Excellent scalability for code parallelization making the computation efficient. • High spatial resolution. • Verstatile tool in comupational materials
	Cons:	• Unable to trace texture evolution due to macroscopic deformation.
Vertex model	**Pros:**	• Mostly used in 2D simulations of the RX process. • Include physical time scale. • Grain boundary curvature is resolved well.
	Cons:	• 3D simulation needs to consider the tessellation of surfaces and increased topological changes. • Not widely used in RX modelling.

Models	Features	
Level set model	**Pros:**	• Direct representation of interfaces and curvature which is not possible in Monte Carlo Potts model and cellular automata. • No need to explicitly treat the interface discretization which is required in vertex models.
	Cons:	• Unable to trace the evolution of texture, a possible remedy might be combining with the crystal plasticity formulations. • Need to resolve the sharp interfaces, this poses the need for the adaptivity of the element mesh or solution grid which adds to the computational time. • Local level set formulation is established to reduce computational time.

2.5 Unsolved problems

The first unsolved problem is the determination of **nucleation sites**, i.e. experimental determination of the critical energy required for grain nucleation. This unsolved problem results in challenges for the prediction of nucleation sites, as well as the simulated kinetics of RX [2,21]. To solve this problem, the electron backscattered diffraction (EBSD) technique [80] adopted in this work would give us a solution to visualize the position of nucleation and analyse the evolution of RX features. The grain nucleation criteria generated from experiments can be applied to the computational models. Furthermore, the simulated RX process can be calibrated against the series of EBSD maps.

The **texture formation** during RX is a long-standing problem which is not clearly understood yet. The orientation of nucleated grains is hard to be determined experimentally which makes the prediction of RXed texture formation challenging [2,9,22,27,81]. Therefore, it is essential to apply advanced recent technology, such as in-situ EBSD, to understand the relationship between RXed orientations with its initial and deformed orientations.

The **incubation time** of new grains during static recrystallization (SRX) [2,3,82], is defined as the time necessary for nucleated sites to form large enough subgrains with sufficient driving force (i.e. sufficient energy difference compared with the surrounding deformed grains) to

overcome the opposing pressure from the grain boundary curvature [2,3]. The incubation time determined by this work would provide an important guideline for the processing routes, such as the HFQ technique to avoid RX during hot forming [83] and forging process to optimise the RX [84].

Despite extensive studies on individual deformed microstructure, no clear relationship has been established to link **strain path**, deformed state and RX. As a consequence, the existing empirical equations and numerical models to predict the RX kinetics always become invalid if the strain path is changed which is a significant issue for the manufacturing industry.

2.6 Summary

In this chapter, a thorough review of the RX is provided. Following the explanation of the thermodynamic mechanism of RX, characters of deformed microstructures which would govern the subsequent RX are introduced. The up to date understandings of RX and its simulations are also summarised. The unsolved problems listed in this chapter will be addressed in Chapters 3 and 4 for the formation of texture and nucleation sites by implementing the CPFE model and KWC phase-field model, in Chapter 5 for incubation time and RX kinetics, and in Chapter 6 for validation of RX mechanism in commercial aluminium alloys.

3 Deformation bands (DBs) formation[1]

3.1 Graphical abstract
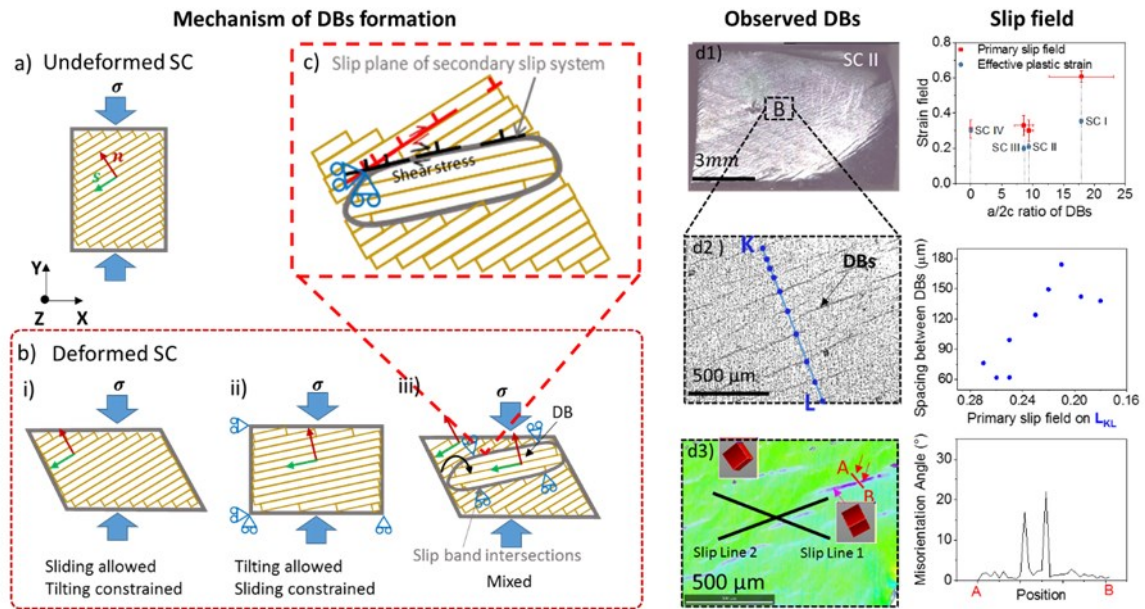
Figure 17 *Graphical abstract to show the mechanism of DBs formation and slip field effect on the formation of DBs.*

---

[1] The work in this chapter has been published in Acta Materialia [40].

3.2 Introduction

DBs are found in various alloys no matter at the single crystal or polycrystalline structure, such as steel [85], zinc [86], aluminium [12], copper [35], nickel [87], magnesium [88], titanium [89] and etc. The formation of DBs is able to effectively accommodate the plastic strain and give rise to the heterogeneities in microstructure by forming noticeable orientation gradients and eventual fragmentation of grains [3].

Therefore, understanding the formation of DBs by examining its crystallographic features might be the key to understanding the grain nucleation in the RX process regarding nucleation criteria and nucleated grain orientations on the basis of heterogeneous deformed microstructure. However, the orientations formed in DBs at the mesoscale and factors affecting the shape and the amount of DBs are not clearly understood.

During the plastic deformation, the lattice sliding occurs which is subject to the simple shear exhibiting the dislocation glide of single slip without creating the lattice rotation [90]. By contrast, the lattice tilting could also occur which is subject to the pure shear [90,91] exhibiting the rotation of a local lattice [92] due to the constraint of lattice sliding (also known as lattice rotation).

In some previous papers, the effect of grain orientation on the formation of DBs is studied for rolling as it is relevant to the generation of deformation textures [3,93]. For instance, the {110}<001> Goss orientation in FCC crystals is stable under rolling in single crystal and polycrystals with large grains, i.e. the Goss oriented grains can undergo extensive deformation without the development of large-scale heterogeneities [3]. By contrast, the Cube oriented FCC crystals are metastable during room temperature compression by virtue of the highly symmetrical nature of its slip systems. The Cube orientation often exhibits very heterogeneous deformation and the splitting of the lattice into strongly misoriented deformation bands [93]. The orientation in DBs is found by rotations about the transverse direction. However, the rotation direction and its reasons are not clearly addressed. Therefore, apart from the orientation formed in DBs, how the strain level and neighbouring grains affect the formation of DBs have not been systematically discussed. This long-standing problem retards the understanding of the subsequent microstructural evolution, such as RX [25,27,94].

The development of RXed microstructure is affected by the formation and growth of nuclei in the deformed structure, while the grain nucleation is dominated by the rate of dislocation accumulation and heterogeneities of deformed structure [3,9]. Therefore, to understand and predict the microstructural evolution during RX and grain growth [21,75], it is essential to examine the development of the heterogeneities in the deformed state [3,25].

In this chapter, single crystals pure aluminium with four different orientations and multi-crystals with different grain morphology were compressed to 0.3 and 0.2 engineering strain. Crystal plasticity finite element (CPFE) models are developed to assess the experimental observations on DBs. Strain distributions were evaluated using the digital image correlation (DIC) technique [95–97] and applied to validate the CPFE model. Deformation activities were evaluated using optical microscopy and electron back-scattered diffraction (EBSD) for the slip lines and DBs, as well as the CPFE modelling for the effective plastic strain and primary slip field calculation.

3.3 Experimental methods and crystal plasticity model

3.3.1 Materials preparation

The work in this chapter used two types of pure aluminium obtained by the Czochralski process [98] from Shanghai Jiaotong University (China) to study the formation of DBs: one is cubic single crystals (SCs) with >99.999% purity (hereafter referred as 5N); the other one is cuboid columnar multi-crystals (MCs) with >99.9% purity (hereafter referred as 3N). The chemical composition of 5N and 3N are listed in Table 4. The crystal orientation information of the samples can be found in Figure C2 and Figure C3.

Table 4 Chemical composition of SC and MC pure aluminium

Sample (wt. %)	Al	Si	Ga	Zn	Fe	Cr	V	Mn	Zr
MC	99.9671	0.0048	0.0045	0.0045	0.0160	0.0009	0.0008	0.0007	0.0003
SC	99.9998	0.00009	0.00004	0.00001	0.00001	0.000004	0.00002	0.000003	0.00001

Face XY and ZY of each sample for EBSD analysis were prepared metallographically with SiC papers (up to 1200 grit) and then polished with ~50 nm OP-S (Oxide Polishing Suspensions) diluted with H_2O by a ratio 1:5 of OP-S:H_2O. Each face was finally electropolished for 40 s in

3. DBs formation

a solution of 9.5 vol% perchloric acid in ethanol at room temperature and 20 V. The electropolished samples were immersed into 0.5 vol% hydrofluoric acid for 6 min to reveal its microstructure under an optical microscope (OM).

3.3.2 Uniaxial compression tests and DIC

The uniaxial compression tests for 3N and 5N samples were carried by Instron mechanical testing frame to achieve up to 0.3 engineering strain at a 0.002 s^{-1} strain rate and room temperature. Sample geometries and stress-strain behaviours from experiments and CPFE modelling can be found in Figure 18. Samples were lubricated by the extremely stable lithium complex grease on both sides to reduce the friction during the compression.

Monochrome time-series 14 bit digital images (see Figure 19) were taken from the compressed front surface (i.e. XY face), by a Canon camera EOS 60D with the function of high-speed continuous shooting. The total number of pixels on the specimen is around 1.6×10^5. The correlation of time-series images for strain responses was performed using software GOM Correlate 2018[2] [99]. The facet size and point distance were set to be 19×19 pixels and 16 pixels with 15.6% overlapping, for the strain calculation. The facet matching was set against the first image with a single pass. The maximum intersection deviation of 0.10 pixels and min. pattern quality of 1.10 were applied for this high accuracy mode. The interpolation method for subpixels was bicubic.

---

[2] https://www.gom-correlate.com/
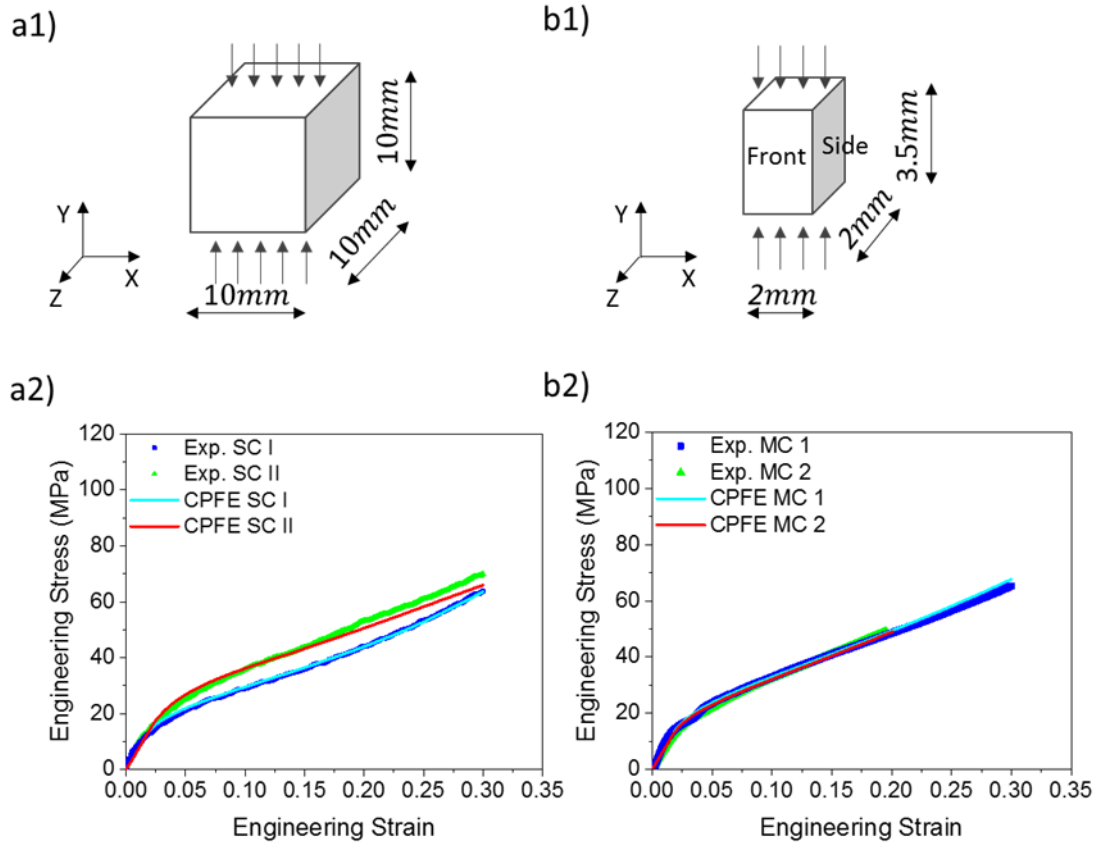
Figure 18 *a1)-b1) show the sample geometry of single crystal (SC) and multi-crystal (MC) samples for testing. a2)-b2) shows the exp. and simulated engineering stress-strain curves of uniaxial deformed SC and MC.*
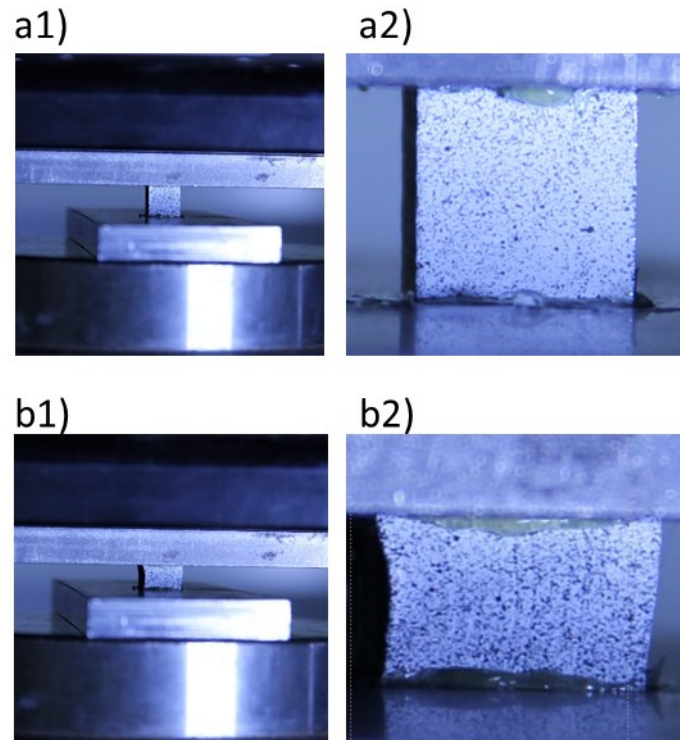
Figure 19 *DIC images of 10cm cubic single crystal a1)-b1) before deformation and a2)-b2) after the deformation.*

3.3.3 Characterisation

OM and EBSD were applied for the microstructural characterisation. Images obtained under an optical microscope equipped with cross polarizers was interrogated using ImageJ software to clearly reveal the DBs. EBSD maps were captured on a Hitachi S3400N with Bruker eFlashHR EBSD system equipped with an eFlashHR camera and Esprit v2.1 software. An accelerating voltage of 20 kV and a step size of 3 μm were used for the EBSD mapping.

3.3.4 Crystal plasticity finite element (CPFE) model

The CPFE model [22,57] is able to predict the heterogeneities of stress and strain distribution, by taking into account of the elastic and plastic crystal anisotropy. It can capture the activation of individual slip systems and the inhibition effect on slip due to the change of grain orientation [60]. The model used in this work is implemented in the UMAT subroutine of ABAQUS software using an explicit scheme.

The deformation gradient, $\mathbf{F}$, is given by $\mathbf{F} = \mathbf{F}^{e}\mathbf{F}^{p}$ where $\mathbf{F}^{e}$ is the elastic deformation gradient and $\mathbf{F}^{p}$ is the plastic deformation gradient. The lattice rotation and stretch are

controlled by the elastic deformation gradient, while the slip and continuum rotation are controlled by the plastic deformation gradient [90].

The rate of deformation, **D**, is given by the sum of elastic and plastic rates of deformation, **D**^{e} and **D**^{p} as follows

$$\mathbf{D} = \mathbf{D}^e + \mathbf{D}^p \tag{3}$$

D^e is determined by the anisotropic Hook's law and **D**^{p} is determined from the symmetry component of plastic velocity gradient, **L**^{p}, as

$$\mathbf{D}^p = \mathrm{sym}(\mathbf{L}^p) \tag{4}$$

where **L**^{p} is the sum of contribution to slip from the active slip systems expressed as

$$\mathbf{L}^p = \sum_{\alpha=1}^{12} \dot{\gamma}^\alpha \mathbf{s}^\alpha \otimes \mathbf{n}^\alpha \tag{5}$$

where $\mathbf{s}^\alpha$ is the line vector along the slip direction and $\mathbf{n}^\alpha$ is its slip plane normal. The dislocation slip rate on the slip system α, $\dot{\gamma}^\alpha$, is given by

$$\dot{\gamma}^\alpha = \rho_{SSD}^m v b^2 \exp(-\frac{\Delta H}{kT})\sinh(-\frac{\Delta V}{kT}|\tau^\alpha - \tau_c^\alpha|) \tag{6}$$

where ρ_{SSD}^m is the density of gliding statistically stored dislocations (SSD), v is the frequency to overcome obstacle barriers, b is the Burgers vector for FCC crystal, ΔH is the Helmholtz energy, k is the Boltzmann constant, T is the temperature in Kelvin, ΔV is the associated activation volume from literature, τ_c^α is the critical resolved shear stress for the slip system α. The accumulated slip after a certain period, $\gamma_{t+\Delta t}^\alpha$, is given by

$$\tau_{t+\Delta t}^\alpha = \tau_t^\alpha + |\dot{\gamma}_t^\alpha|\Delta t \tag{7}$$

A Taylor's dislocation hardening rule to describe the isotropic hardening during plastic deformation is expressed as follows. In this SC and MC work, only SSD is taken into the account in Taylor's dislocation hardening without considering the effect of GND. It has been demonstrated by Jiang et al. [92] and Guan et al. [57] that the presence of GND is not obvious in unconstrained deformation of large size single crystal and multicrystal Ni alloys since GND is sensitive to the length scale. Furthermore, it has technical issues to include GND into the CPFE modelling when the induced strain level is high [100].

$$\tau_c^\alpha = \tau_{c0} + G_{12} \cdot b \cdot \sqrt{\rho_{SSD}^s} \tag{8}$$

where τ_{c0} is the initial critical resolved shear stress, G_{12} is the shear modulus, ρ_{SSD}^s is the density of sessile SSD determined by a phenomenological relation with effective plastic strain p as

$$\dot{\rho}_{SSD}^s = \lambda \cdot \dot{p} \tag{9}$$

where λ is the work hardening coefficient and the effective plastic strain rate $\dot{p}$ is calculated from the plastic deformation rate tensor $\mathbf{D^p}$ by

$$\dot{p} = (\frac{2}{3}\mathbf{D^p} \colon \mathbf{D^P})^{1/2} \tag{10}$$

The physical properties used in this work for pure aluminium were obtained from the literature [57,101–103] and listed in Table 6. Note that the Helmholtz free energy ΔH used in this study did not consider the strain rate effect because the test is conducted at room temperature.

Table 5 *Material properties of SC and MC pure aluminium*

Boltzmann constant (k)	1.38×10^{-23} JK^{-1}
Burgers vector magnitude (b)	2.86×10^{-4} μm
Temperature (T)	293 K
Young's modulus (E)	700 MPa
Initial slip stress (τ_c)	6 MPa
Mobile dislocation density (ρ_{SSD}^m)	0.01 μm^{-2}
Jump frequency (v)	10^{11} s^{-1}
Helmholtz free energy (ΔH)	2.9×10^{-20} J
Activation volume (ΔV)	$6 \times 10^{-15} b^2$
Hardening coefficient (λ)	0.1 μm^{-2}
Strain rate ($\dot{\varepsilon}$)	2×10^{-3} s^{-1}
Possion's ratio (v_{12})	0.35

3D single crystal and multi-crystal CPFE models as shown in Figure 20 were constructed to study the deformation behaviour of pure aluminium. Finite elements with 20 nodes and reduced integration (C3D20R) were used. The orientation information in CPFE model was obtained directly from the corresponding EBSD maps. The bottom, left and back surfaces are fixed in the model to simulate the uniaxial compression to 0.2 and 0.3 engineering strain.
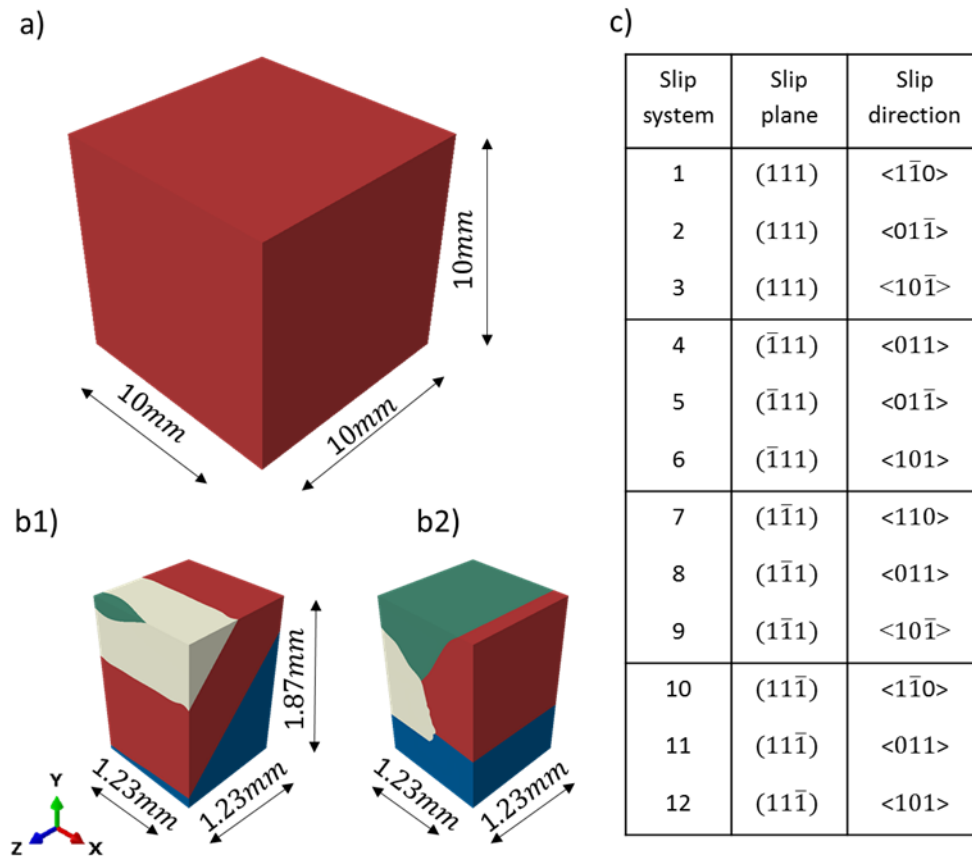
Figure 20 *CPFE models for a) single crystals and b1)-b2) multi-crystals; c) shows the designations of 12 slip systems of aluminium FCC structure with respect to an orthogonal (x, y, z) reference system.*

3.4 Experimental and crystal plasticity modelling results

3.4.1 Validation of crystal plasticity model

The simulated stress-strain curves shown in Figure 18 give reasonably good agreement with experimental data for both single crystals and multi-crystals. Note that there is a very slight stress drop in the stress-strain curve for MC 1 at ~0.06 strain. By checking the deformed shape of MC 1, the slight shift of stress could be attributed to the generation of obvious slip lines (i.e. shifts of lattice structure to sample surface).

In addition, the DIC experimental and CPFE numerical strain yy maps, for deformed single crystal and columnar multi-crystal samples, show a good match, when the total engineering

strain is 0.15 and 0.3. The average value of strain yy on the midline of deformed single crystals and multi-crystals is shown in Figure 21 a). The spread of strains along the midline is shown by their standard deviation as error bars in Figure 21 a). The shape of deformed single crystals are also compared with the deformed CPFE models in Figure 21 b) and c). The above comparisons made between experimental results and CPFE simulated results demonstrate that the CPFE model is able to simulate the deformation behaviour of single, multi-crystal pure aluminium alloys with reasonable accuracy.
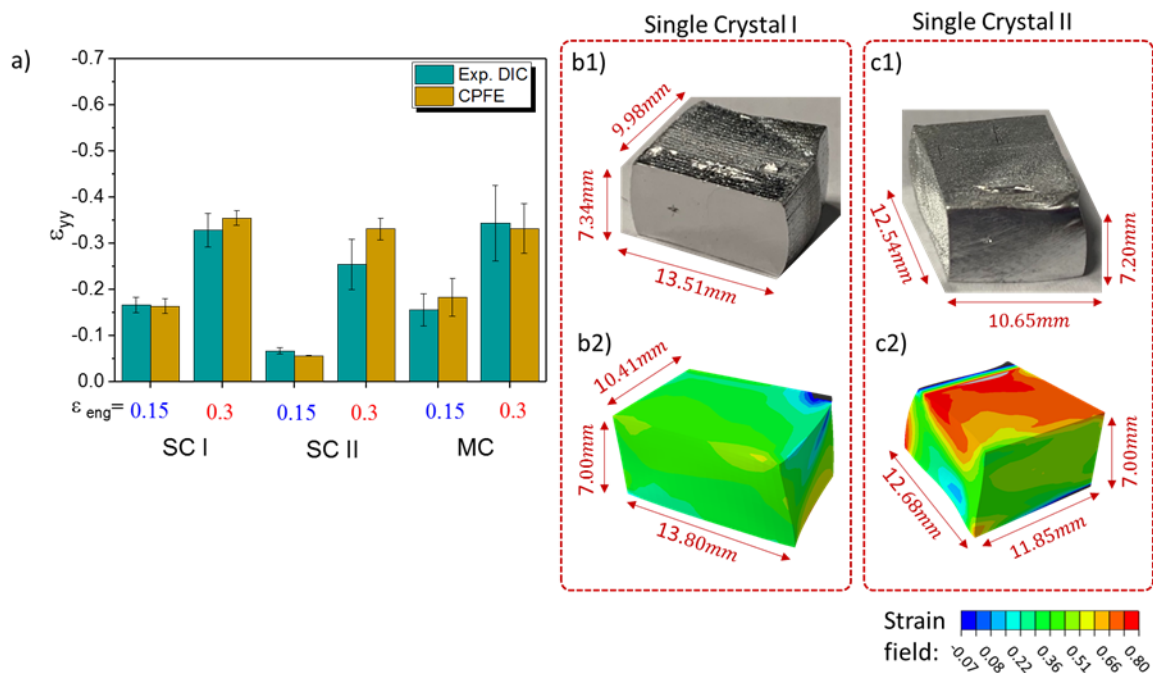
Figure 21 *a) Comparison of average ε_{yy} on the midline of the specimen between DIC calculated and CPFE simulated results when the overall engineering strain is 0.15 and 0.3. b1)-b2) and c1)-c2) compare the geometry of deformed samples from experiments and CPFE simulations.*

3.4.2 Single crystal analysis

3.4.2.1 Slip trace analysis

The traces of 12 slip systems left on the XY face were calculated based on the orientation of the deformed matrix in single crystal I, II, III and IV (see Figure 22 and Figure 23). The slip fields of the activated slip systems were calculated by CPFE modelling according to the initial orientation in single crystals before compression. The primary slip and secondary slip are

defined as the slip systems with the highest and second-highest value of Schmid factors (SF) which contributes to the highest and second-highest value of slip field in CPFE modelling. In this work, the slip line close to the trace of primary slip is defined as slip line 1 and the slip line close to the trace of secondary slip is defined as slip line 2.

Two types of slip lines with different tilting angles were plotted superimposed with the traces of four slip planes. OM results together with the slip trace analysis also show that slip line 1 and 2 are more closely aligned with the traces of slip systems with the traces of primary and secondary slip in all deformed single crystals. It is acceptable that some slip lines are not perfectly aligned with their corresponding {111} slip plane traces, as the slip trace analysis is based on the orientation of deformed matrix while the compressive friction is unavoidable as discussed in [85].
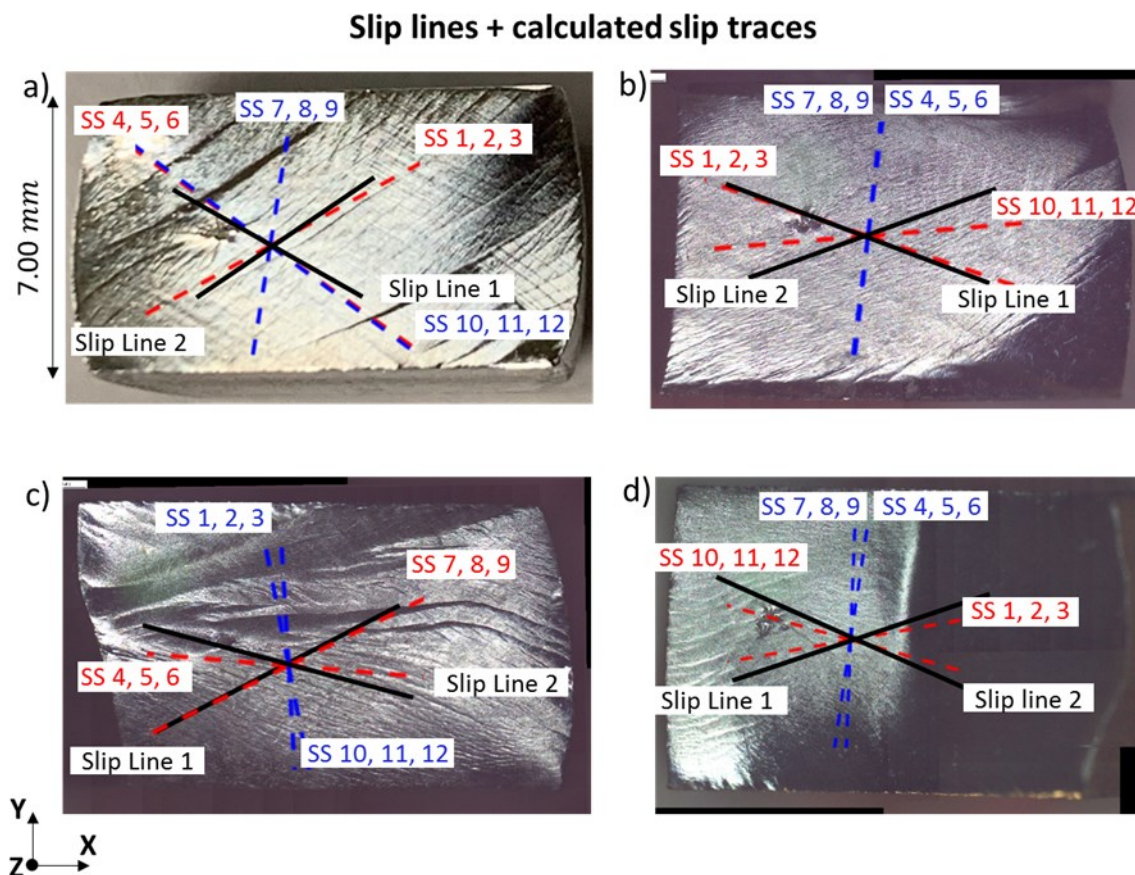
Figure 22 *a)-d) are the optical microscope images of 30% uniaxial deformed single crystal I, II, III and IV. Slip lines left on the sample surface and the calculated traces of 12 {111}<110> slip systems (SS) are superimposed. Traces of primary and secondary slip are highlighted in red and the other {111} traces are marked with blue dashed lines.*

3.4.2.2 Deformation band formation

The EBSD IPF maps according to the deformation axis (i.e. Y-axis) before and after deformation are plotted superimposed with their orientated crystals in Figure 23 a1)-d1). It can be seen that the DBs are formed in these crystals to accommodate the imposed plastic deformation. Unlike the uniaxial tension tests, the top and bottom surfaces of the compressed specimens are free to move horizontally as shown in [88]. As shown in Figure 23, the orientation of the matrix nearly remains the same before and after compression. The slight rotation of crystal orientation in the deformed matrix is attributed to the experimental errors from the sample preparation, imaging alignments and unavoidable compressive friction.

DBs with similar tilting angles are found in deformed microstructure for each grain orientation (see Figure 23 a2)-d2)). Those bands are more likely located parallel to the slip line 2, such as the DBs found in single crystal I, II and III. The secondary slip system for every single crystal and its corresponding slip lines are determined and shown in Figure 23 a1)-d1).

After measuring the misorientation angle across the bands in Figure 23 a3)-d3), a sharp orientation change was observed at the edge of bands (i.e. deformation-induced grain boundary, see Figure 23 a4)-d4)). The misorientation >15˚ (i.e. HAGB) is developed during deformation for the deformation-induced grain boundary. This means the orientation inside the band has an approximately constant orientation that is significantly different from the orientation in the matrix. These observations agree with the definition of DBs by Barrett et al. [33] in 1939.
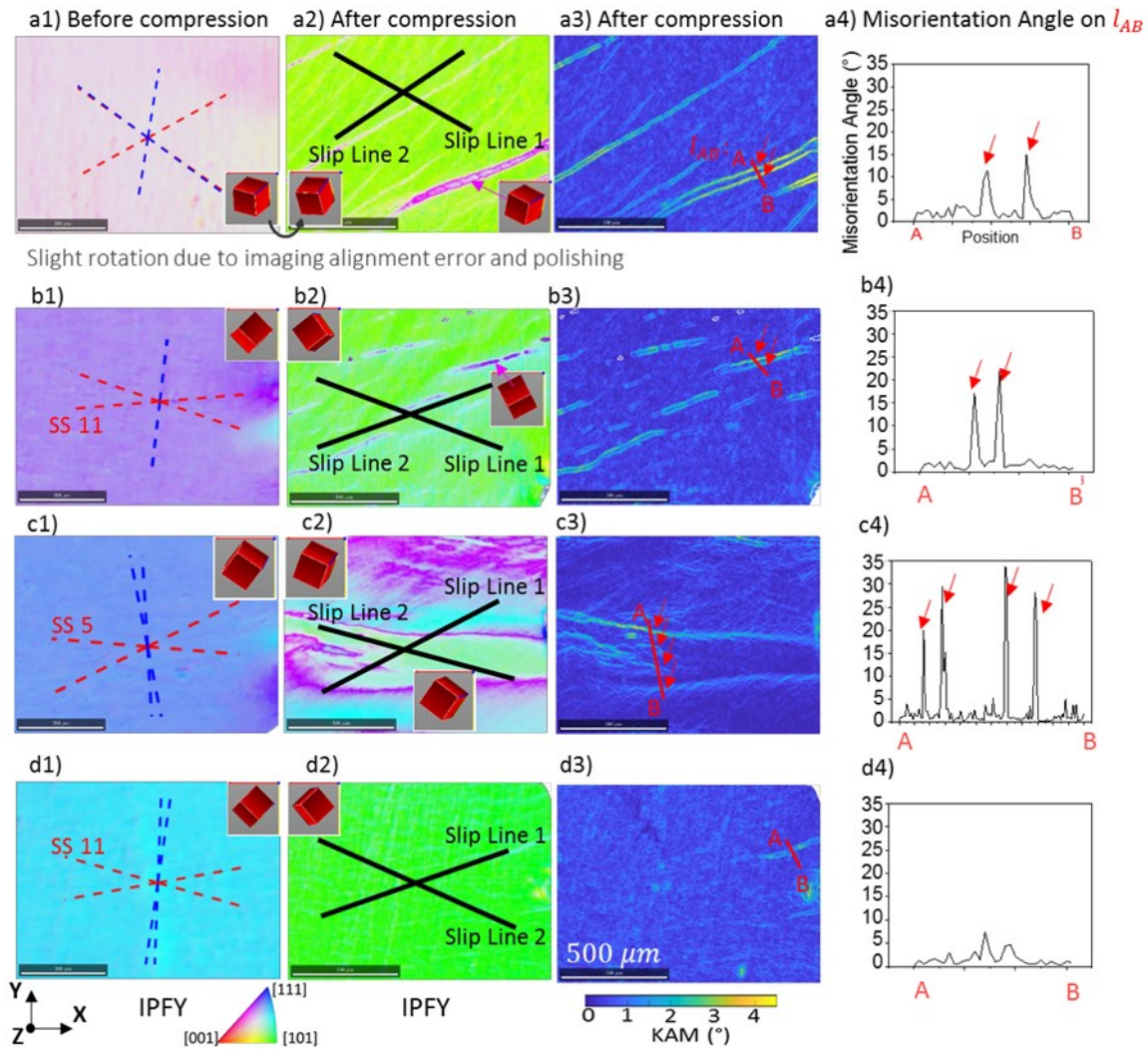
Figure 23 *a1)-d1) and a2)-d2) are the EBSD IPF maps in the Y-axis (i.e. the loading direction) for the single crystal I, II, III and IV before and after uniaxial compression. The secondary slip system (SS) of the deformed matrix and its trace are marked out in b1)-d1) as a comparison of slip line 2. a3)-d3) are the kernel average misorientation (KAM) maps of deformed single crystal a-d respectively. The misorientation distribution on Line AB is plotted in a4)-d4).*

3.4.2.3 Single crystal modelling

CPFE predicted effective plastic strain and slip fields for the primary and secondary slip system are plotted for the front (i.e. XY) faces of deformed SC I, II, III and IV in Figure 24 based on their initial grain orientations. The existence of slip fields demonstrates that more than one slip system is activated in deformed single crystals. The ellipsoidal DB is characterised by its aspect ratio a/2c, where a and c are the longer and shorter length of semi-axes on the DB as shown in Figure 28 f). The a/2c ratios of DBs were measured from their EBSD maps in Figure 23. The

value of 2c was determined as the maximum width of each DB. The longer length of semi-axes, a, was measured from the widest point to the tip of DBs. If the tip of DB was not captured by the EBSD map, the value of a was measured from the widest point of the DB to the edge of the map. By comparing the slip fields in deformed SC I, II, III and IV, it has been found that the primary slip exceptionally dominates in SC I, while it has the highest a/2c ratios of DBs (see Figure 28 e). Also, the primary slip is much less dominated in SC IV while it has the fewest DBs (see Figure 23 and Figure 24 d).
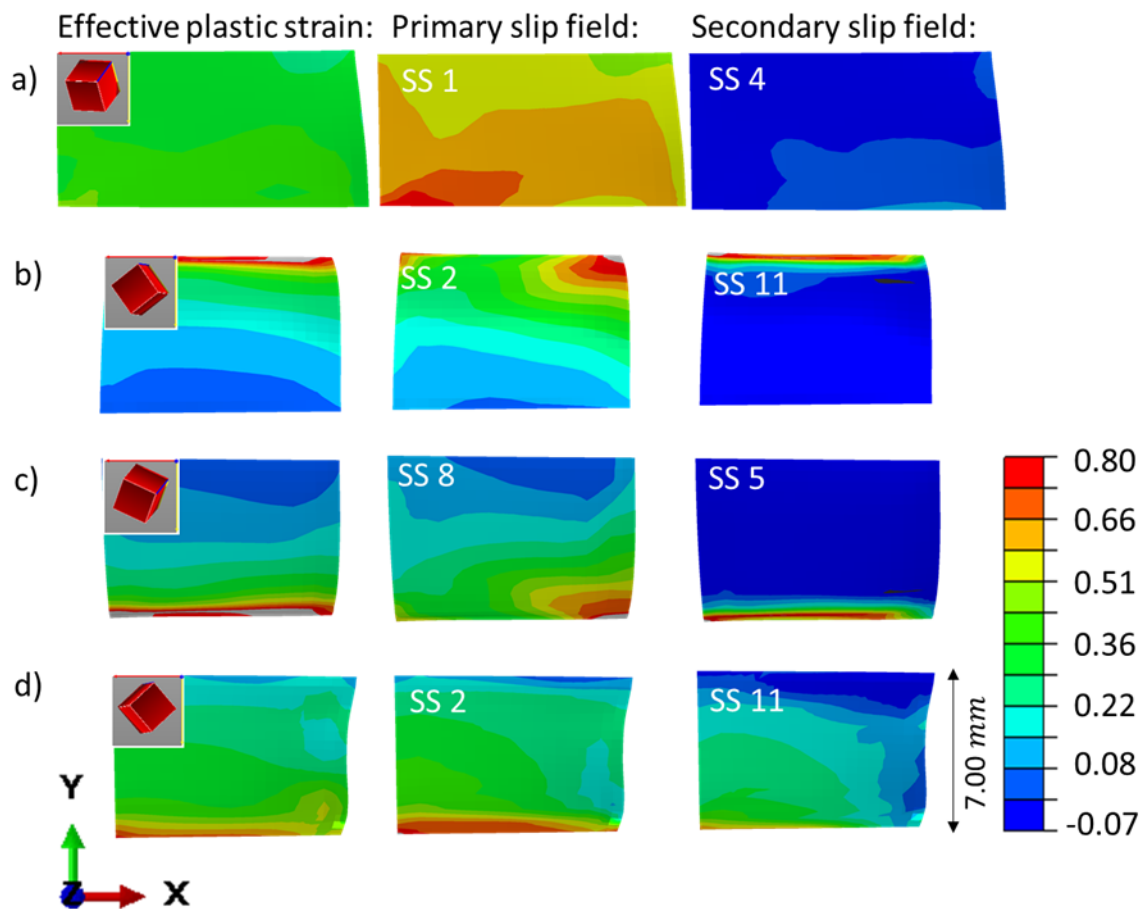
Figure 24 *a)-d) are crystal plasticity predicted effective plastic strain distribution and slip fields for the primary and secondary slip system in single-crystal I, II, III and IV.*

In Figure 25, DBs left on the front (i.e. XY) face and side (i.e. ZY) face of SC II and its CPFE results are compared. It has been shown from Figure 25 a) that the effective plastic strain distribution, primary and secondary slip fields vary for different faces of the same crystal. Figure 25 b1-2) and c1-2) are the OM images to show slip lines and etched DBs for the ZY and the XY face respectively. It has been found that DBs are aligned nearly parallel to the secondary

slip lines. It is very interesting to see that the fraction of DBs and spacing between DBs are strongly correlated with the intensity of the primary slip field (see Figure 25 d1)-d2)). The higher the intensity of the primary slip field is, the higher the DBs fraction and the denser the DBs would be formed.
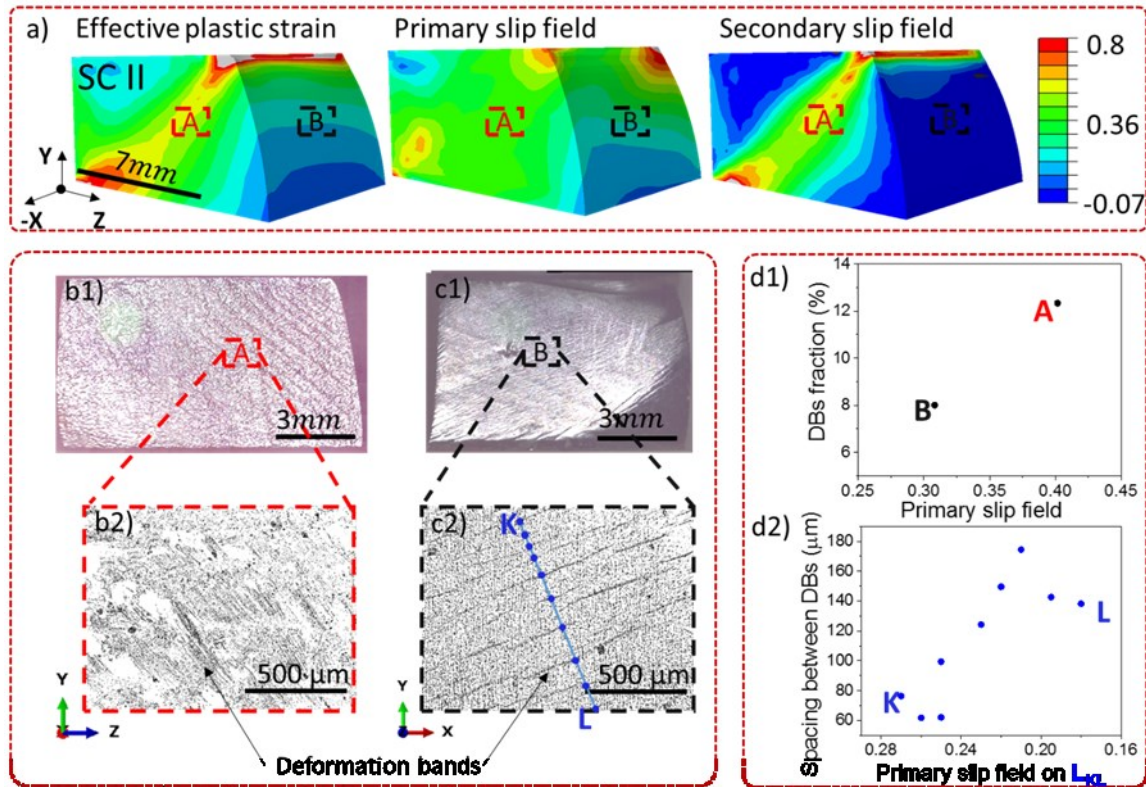
Figure 25 *a) shows the CPFE calculated effective plastic strain distribution, primary slip field and secondary slip field for SC II. b1-2) and c1-2) are the OM images on ZY and XY face respectively to show slip lines and etched microstructure. d1) compares the DBs fraction against its primary slip field. KL is a line vertical to the alignment of DBs with blue dots showing the nonuniform distributed DBs on Line KL. d2) quantitatively compares the spacing between adjacent DBs on Line KL against the CPFE simulated primary slip field at the corresponding position.*

3.4.2.4 Orientation formation

Pole figures (PF) of {111} planes in deformed single crystals are plotted together with the PF before deformation in Figure 26 a1)-d1). Pole figures of {100} and {110} planes are shown in Appendix C Figure C2. It is clearly seen that the newly formed orientation is originated due to the rotation of matrix around Z-axis during deformation in Figure 26 a1)-d1). This indicates that the crystal slip planes are rotating around the loading axis. In Figure 26 a2)-d2), obvious orientation shifts (i.e. misorientation angle >10˚) are also found in the deformation state

resulting in the increase of misorientation angle distribution, especially for the crystals with distinct DBs, i.e. single crystal I, II and III. The increase of misorientation angle demonstrates that lattice sliding was not uniform even in this uniaxial compression of single crystals due to the interaction of multiple slip systems, giving rise to the storage of dislocations in the deformed structure.
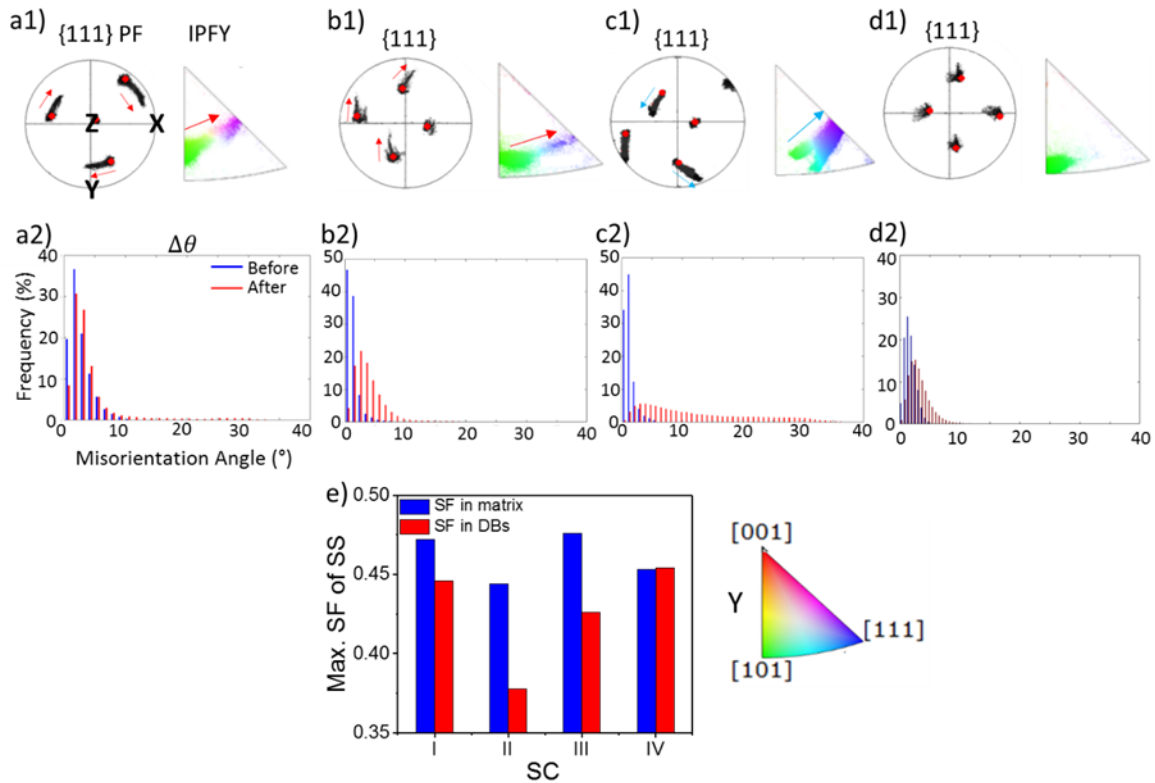
Figure 26 a1)-d1) are the pole figure (PF) and inverse pole figures (IPF) of deformed single crystal I-IV. Red dots show the orientation before compression. Red arrows represent the clockwise rotation and blue arrows represent anti-clockwise rotation around Z-axis. The colour in IPF is consistent with IPF colour key regarding the compression direction (i.e. Y-axis). a2)-d2) show misorientation angle distribution before and after compression for single crystal I-IV.

Through checking the corresponding inverse pole figures (IPF) in Figure 26 a2)-d2), it has been found that the {111} slip planes tend to orientate perpendicular to the loading direction (i.e. Y-axis) in the newly formed DB, which means slip become harder to be activated in DB (see Figure 26 a1)-d1)). This is confirmed by the drop in the highest SF in Figure 26 e) that the orientation in DBs is rotated to a 'harder' orientation. The Schmid factors of 12 slip systems in the deformed matrix and DBs are shown in Appendix C Figure C1.

3.4.3 Columnar multi-crystal

3.4.3.1 Slip trace and deformation band

The slip traces of 12 {111} <110> slip systems in each grain were calculated and plotted superimposed with the inverse pole figure (IPF) maps regarding the Y-axis (i.e. the loading direction) in Figure 27. The traces of two slip planes with the primary and secondary slip system calculated based on the CPFE are highlighted in red and the other two {111} traces are highlighted with blue dashed lines. The most easily activated slip plane is labelled out by red and the second easily activated slip plane is labelled out by black in Figure 27.

It can be seen in the EBSD estimated KAM maps that DBs with high misorientation angle on its transition bands were formed in some grains. By comparing the ZY faces of MC 1 and 2 in Figure 27 a2)-b2), it can be concluded that the total imposed strain level does have a strong effect on the formation of DBs. The ZY faces of MC 1 and 2 have the same grain orientations and tilting angle of GBs but different engineering strain levels, i.e. 0.3 for MC 1 and 0.2 for MC 2. The ZY face of MC 1 has more distinct DBs, while no obvious DB is found on the ZY face of MC 2. Same with the study on single crystals, factors affecting the formation of DBs in multi-crystals are discussed with CPFE modelling in the next section.

It has also been found that DBs are located in parallel to the trace of secondary slip, especially on the XY face of MC 1 and 2 (see Figure 27 a1)-b1)). However, DBs on ZY face are not perfectly aligned along with the secondary slip. This might be caused by the local stress field due to the existence of tilting grain boundaries (see Figure 27 a2)-b2)).
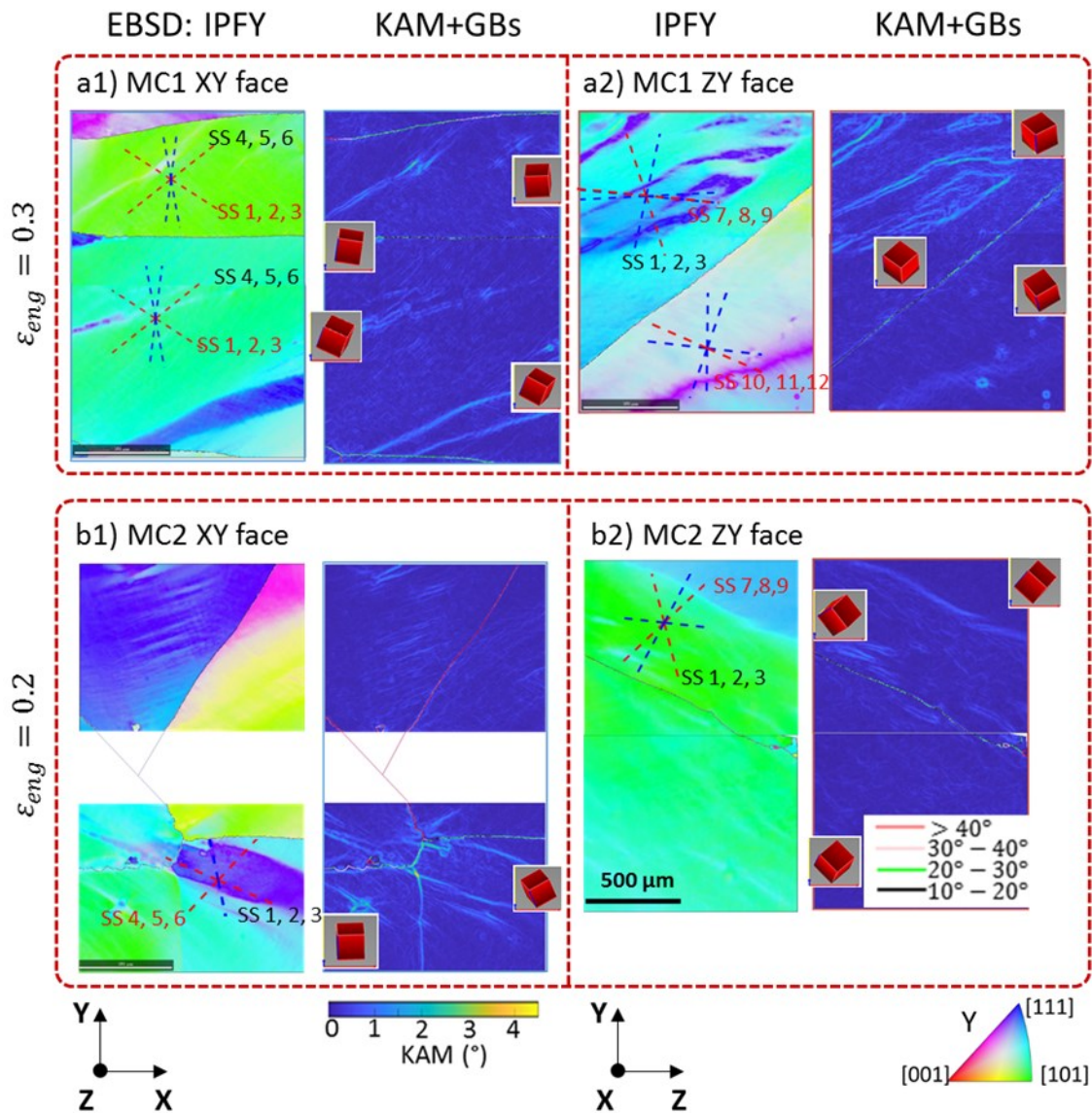
***Figure 27** a1)-a2) and b1)-b2) show the EBSD IPF-Y map and its KAM map for XY and ZY face on MC 1 and 2 respectively. The trace of primary and secondary slip plane are marked out as red dashed line together with the red and black label respectively in IPFY maps. The colour on grain boundaries (GBs) in KAM maps indicates the value of misorientation on GBs. The crystal orientation information at each position is superimposed in the KAM maps.*

3.4.3.2 Multi-crystal modelling

The effective plastic strain and slip field of primary slip on the XY and ZY face is plotted in Figure 28 for CPFE multi-crystal (MC) 1 and 2 which were deformed to 0.3 and 0.2 engineering strain respectively. It is clear that the distribution of the effective (the sum of) plastic strain field is very different from the primary or secondary slip field.

By comparing the simulated results of the two set of microstructure in Figure 27, it is convincing that the formation of DBs is more correlative with the value of primary slip field instead of the effective strain field. For instance, the effective plastic strain distribution is quite homogeneous on the ZY face of MC 1. However, DBs shown in deformed EBSD maps were only formed in the above grain (i.e. grain 2). Also, the effective plastic distribution in the grain 4 on the XY face of deformed MC 2 (see Figure 28 a2)) is low. However, a distinct DB is found in this area. By contrast, the primary slip field explains well for the formation of DBs, i.e. more DBs could be formed in the area with a high primary slip field.

Based on the work of Brown et at. [104], the DBs resulting from plastic strain would be ellipsoidal to balance the applied stress. The stress in the neighbourhood of the tip due to the dislocation pile-up would be proportional to the aspect ratio a/2c of the DBs (see the sketch in Figure 28 f). The relationship between the a/2c ratio of DBs and primary slip field, as well as effective plastic strain, are compared for deformed single crystals and multi-crystals in Figure 28 e) and f). The primary slip field demonstrates a strong correlation with the a/2c ratio of DBs, while no obvious relation is found between the effective plastic strain and a/2c ratio.

The DBs fractions on each face of MC 1 and 2 versus values of the effective plastic strain and primary slip field at the corresponding positions of DBs are plotted in Figure 28 g). It has been found that high DBs fraction is related to high values of the primary slip field, instead of the field of effective plastic strain.
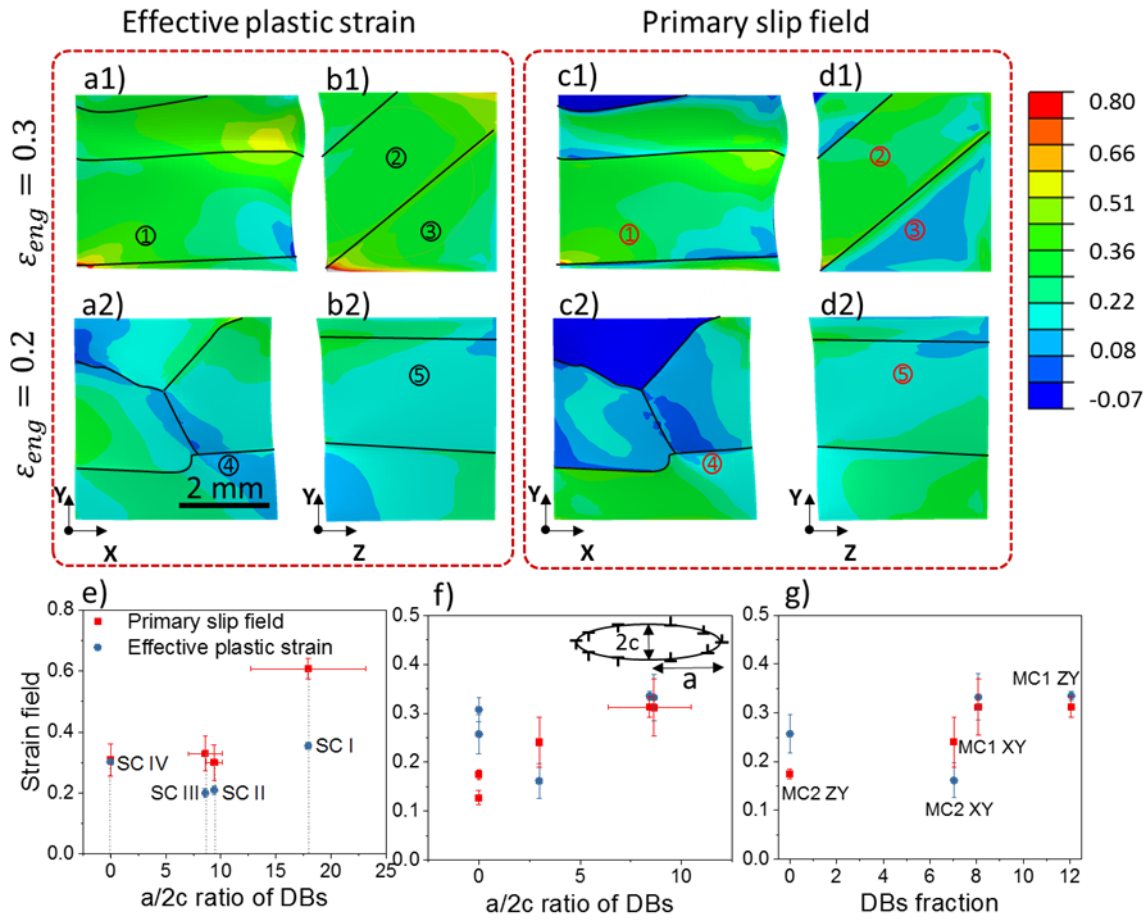
Figure 28 *Crystal plasticity predicted effective plastic strain and primary slip fields for multi-crystals: a1)-b1), c1)-d1) are the front face and the side face of MC 1 which was deformed to 0.3 engineering strain; a2)-b2), c2)-d2) are front face and the side face of MC 2 which was deformed to 0.2 engineering strain. An ellipsoidal DB with semi-axes a and c is drawn after Brown et al. [104]. e) and f) show a/2c ratios of DBs against primary slip field and effective plastic strain value in SC I-IV and MC 1-2. g) shows DBs fractions against primary slip field and primary slip field for each face of multi-crystals. a/2c ratios and DBs fractions of the whole map are measured from EBSD maps while the primary slip field and effective plastic strain are obtained from CPFE modelling at the corresponding position.*

3.4.3.3 Orientation formation

Pole figures (PF) of each grain in deformed samples are plotted together with the PF of undeformed crystal in Appendix C Figure C3. Same with the DBs in deformed single crystals, obvious orientation rotations around Z-axis are found in the distinct DBs in deformed multi-crystals.

The corresponding inverse pole figures (IPF) regarding Y-axis for XY and ZY face are plotted in Appendix C Figure C4 for deformed MC 1 and 2. Keeping the same with the DBs in single

crystals, the {111} slip planes in DBs are found to preferentially orientate perpendicular to the loading direction during compression, which means their slip systems are harder to be activated.

3.5 Discussion

In 1979, the homogeneous distribution of primary and secondary slip lines across all over the sample was already observed by Franciosi et al. [102] in copper and aluminium single crystals under optical microscopes. These crystallographic slip lines were also found by Asaro [105] in 1983 in polycrystalline alloys. Gioacchino and Fonseca [85] in 2012 firstly related the local strain saturation with slip bands (i.e. with respect to slip lines) by using the digital image correlation technique. However, the mechanism of DBs formations has not been clearly understood by relating the slip system activation with the strain localisation. The work in this chapter has systematically analysed the formation of DBs and its characteristics in single crystal and multi-crystal pure aluminium according to the slip trace analysis, EBSD mapping and crystal plasticity simulation.

3.5.1 Mechanism of deformation band formation

In this study, the tabular strain localisation structures defined as DBs are found in uniaxial compressed single crystal and multi-crystal pure aluminium alloys. Through comparing the optical microscope and EBSD maps of all samples at the same area before and after compression (see Figure 23), grain sliding and lattice rotation >15° are observed for the deformed sample matrix and DBs respectively.

According to the slip trace analysis shown in Figure 22, two types of slip lines are proven to be created by the primary and secondary slip system. The EBSD maps show that the DBs tend to align parallel to the trace left by the secondary slip system (see Figure 23 for single crystals and Figure 27 for multi-crystals).

Therefore, it can be concluded that the slip band intersection of the primary and secondary slip system could be the cause for the DB formation since the lattice sliding would be constrained at the slip band intersection area. Meanwhile, similarly with the Eshelby's model for the slip band and grain boundary intersections [106], the dislocations would pile up at the slip band intersection area giving rise to the high stress ahead of the blocked slip band. This local

constraint prohibits the lattice sliding but would trigger lattice orientation rotation to form DBs. These observed DBs in mesoscale can be referred to kink bands rather than the bands of secondary slip since the wall of bands is perpendicular to the primary main slip direction as discussed in [35,88].

The mechanism of DB formation is summarised in Figure 29. Three different types of deformation in single crystal are shown in Figure 29 b): i) describes the lattice sliding (i.e. no orientation change) when only one slip system is activated; ii) describes the single slip system activation and lattice rotation (i.e. tilting) due to constraints; iii) describes the DBs formation due to slip band intersection. In Figure 29 c), a detailed sketch shows the intersection of two types of activated slip systems (i.e. *red* and *black* symbol), as well as the dislocation pile-up at the intersection point along with the secondary slip system. It also explains the strain localisation at the boundary of DBs due to the effective barriers to the dislocation motion, which is similar to the effect of grain boundaries [106].

As shown in Figure 23 and Figure 29, the DBs are more favourable to align parallel to the trace of secondary slip system rather than the trace of primary slip. It has been demonstrated by the CPFE modelling in Figure 24 that the strain field of secondary slip is much less than the primary slip. Hence, the lattice sliding would be mainly caused by primary slip and the blocking of lattice sliding would be caused by the accumulation of enough secondary slip. The slip plane of secondary slip would be the blocking area for primary slip. Therefore, the DBs are found to be parallel to the trace of secondary slip rather than the primary slip.
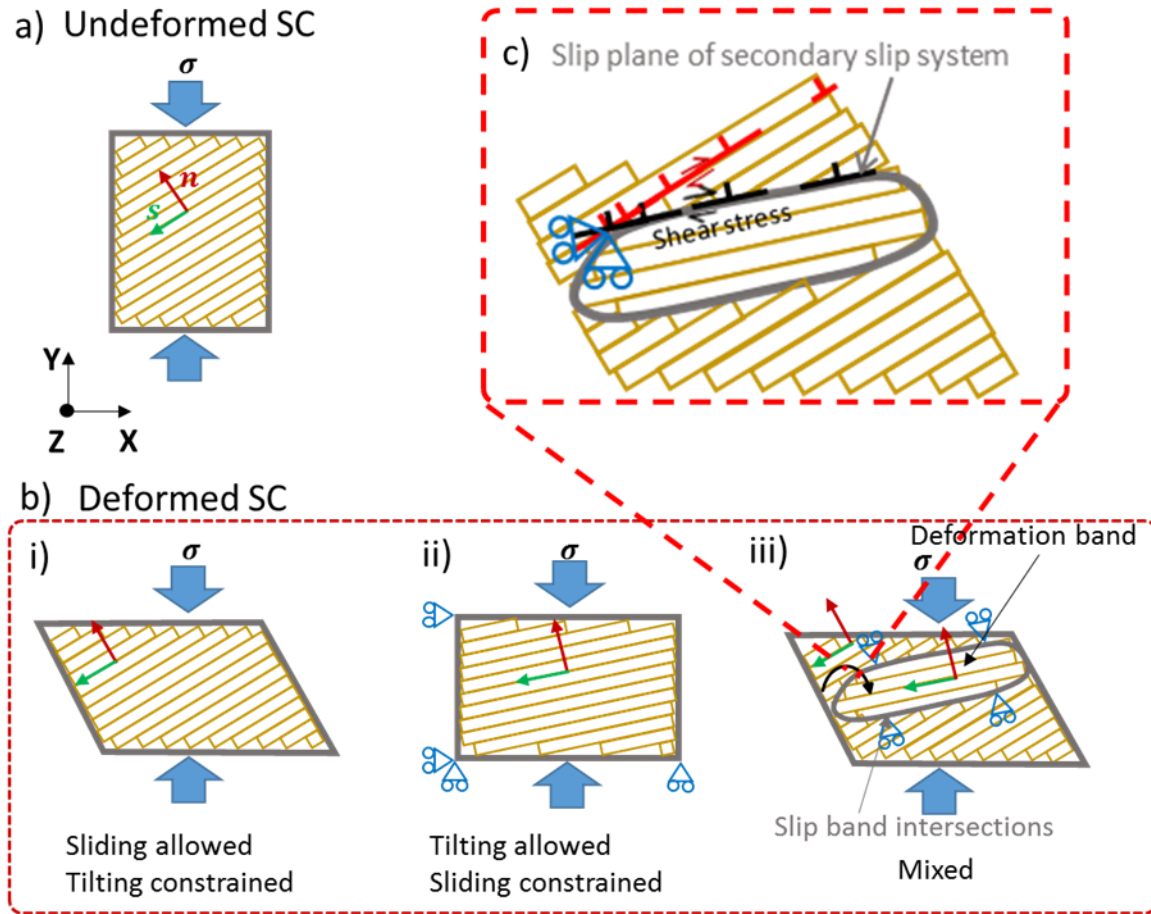
Figure 29 *A sketch to show the mechanism of DB formation. a) Slip direction* ***s*** *and slip normal* ***n*** *in a single crystal (SC) before deformation. b) Three types of deformation in deformed single crystal: i) lattice sliding only; ii) lattice rotation (i.e. tilting) with constraints; iii) a combination of lattice sliding and rotation due to local constraints causing the formation of DB. c) A detailed sketch shows the local constraint due to slip band intersection and dislocation pile up at an intersection point.*

3.5.2 Factors affecting deformation band formation

3.5.2.1 Crystal orientation

The deformed microstructures of four single crystals with different orientations are compared to study the effect of orientation on DB formation (see Figure 23). No distinct DBs are found in deformed single crystal (SC) IV. By comparing the predicted effective plastic strain and slip field of single crystals in Figure 24, it can be seen that the SC I, II, III and IV have similar values of effective plastic strain near DBs. Meanwhile, SC IV has the most homogeneous slip field distribution for the primary and secondary slip systems (i.e. no dominating slip system) in comparison with the other single crystals. Therefore, when the total strain is the same, the

crystal orientation would affect the formation of DBs by having a different level of primary slip fields. If one slip system is dominated during deformation, the peak value of its slip field, i.e. the value of primary slip field, could be high enough to facilitate the formation of distinct DBs with high misorientation on its boundaries (see SC I and II in Figure 23).

Furthermore, the crystal orientation also affects the aspect ratio, i.e. a/2c value, of formed DBs by having different levels of the primary slip field (shown in Figure 28 e). The primary slip field could be directly related to the stress level formed at the tip of DBs while the stress is proportional to the aspect ratio a/2c of the DBs as discussed by Brown [104]. Therefore, the primary slip field has a strong correlation with the aspect ratio of DBs.

3.5.2.2 Strain level

The multi-crystals MC 1 and MC 2 whose grain orientations are nearly the same were compressed to different strain levels, i.e. 0.3 engineering strain for MC 1 and 0.2 for MC 2, to compare the strain effect on DBs formation. Regarding the side faces of MC 1 and 2 whose grain orientation and grain structure are same, much fewer DBs and minor crystal rotation were found in MC 2 as seen in Figure 27 b1)-b2). Therefore, the induced strain level could also be the key factor in the formation of DBs. As shown by the CPFE results for ZY faces of MC 1 and MC 2 in Figure 28, the ZY face of MC 2 with no DBs have a lower value of the primary slip field while no obvious difference is found for the effective plastic strain level, especially in grain 2. Hence, the more primary slip would lead to more slip band intersection and the crystal rotation in DBs.

By comparing the aspect ratio a/2c of DBs in deformed MC 1 and MC 2, it has been found in Figure 28 f) that the high value of the primary slip field would prompt the occurrence of DBs with the high a/2c ratio. It may imply that highly concentrated stress could be formed at the tip of DBs due to the dislocation pile-up of primary slip.

3.5.2.3 Neighbouring grain

The grain structure could affect DBs formation due to the constraints imposed by the sharp sloped orientation change from neighbouring grains [85,107]. As discussed before, DBs formed in single crystals and multi-crystals are found to preferentially locate parallel to the slip trace of secondary slip system. However, for the ZY face of multi-crystals which have highly sloped orientation change, DBs are found to be parallel to the grain boundary instead of the

secondary slip system (see Figure 27 a2)-b2)). Hence, the constraint imposed by the orientation change would affect the local stress-strain state in grains and lead to crystal rotation. The stress concentration at grain boundaries caused by slip band-grain boundary intersections has already been demonstrated by Guo et al. [106] by using cross-correlation-based electron backscatter diffraction. The effect of neighbouring grains explains why DBs near the highly sloped grain boundary do not always in parallel to the secondary slip system.

However, it has been found that neighbouring grains would not affect the new orientation formed in DBs. The orientation in DBs near highly sloped grain boundary still tends to rotate around Z-axis and become 'harder' (see Figure C4 in Appendix C), which means that slip become harder to be activated in DBs (i.e. the highest value of SF in DBs is lower than the deformed matrix).

3.5.2.4 Slip direction

The activated slip direction is also found to affect the formation of DBs, as the area fraction of DBs varies for the XY and ZY face of the same single crystal (see Figure 25 b)-d)). The grain orientation and total strain level are the same in this case. Therefore, the accumulation of slip on different faces would be different due to the activated slip direction, resulting in the different distribution of the primary slip field as shown in Figure 25 a). According to the quantitative analysis in Figure 25 d1)-d2), the higher the primary slip field is, the higher the area fraction of DBs and the higher density of DBs would be formed.

3.5.3 Orientation in deformation band

The orientation formed in DBs is analysed by comparing the pole figures and inverse pole figures of single crystals and multi-crystals before and after compression. According to the pole figures shown in Figure 26 and Appendix 3 Figure C3, it has been found that the orientation in DBs is formed due to the lattice rotation around Z-axis following clockwise or anti-clockwise direction. The more distinct DBs are formed, the higher the misorientation angle is found between the deformed matrix and DBs (see Figure 23 a4)-d4)).

According to the inverse pole figures (see Figure 26 a1)-d1) and Figure C4 in Appendix C), it has been found that {111} slip planes in DBs tend to rotate perpendicular to the loading direction, i.e. Y-axis. This means that slip become harder to be activated in all DBs compared with the deformed matrix when the loading direction is still Y-axis. This has been demonstrated

by the drop in the highest Schmid factors (SF) in DBs (see Figure 26 e)). Therefore, it is rational to conclude that the direction of crystal rotation in DBs, i.e. either clockwise or anti-clockwise, depends on which way could reduce its Schmid factor values. Furthermore, the higher the primary slip field is, the higher the rotation angle is found for the slip planes in DBs (i.e. the slip become 'harder' to be activated in DBs).

3.5.4 Prediction on deformation bands

To predict the DBs formation, the CPFE modelling is a very effective technique, as the slip field of each slip system in single crystals, multi-crystals and polycrystals can be checked. The primary slip field rather than the effective strain field can be used to determine whether distinct DBs would be formed in grains. As the DBs tend to occur at the high slip field regions, the primary slip field calculated based on crystal plasticity theory is helpful for the prediction on the area fraction, density and aspect a/2c ratio of activated DBs. Since the CPFE modelling for the prediction of strain fields has been validated to a large extents by Dunne et al. [57,101,108,109], various factors, such as neighbouring grains, complex strain path, strain levels and etc., can be integrated into CPFE model for the accurate prediction on the eventuated plastic strain distribution and the peak value of slip field.

3.6 Summary

In this chapter, integrated experimental study and CPFE modelling in mesoscale are utilized to provide new insights in understanding the mechanism of DBs formation in pure aluminium and its affecting factors. It has been shown that:

1. The DBs are produced aligning parallel to the secondary slip system due to the constraints from the slip band intersection of primary and secondary slip. It is rational to speculate that the lattice sliding is prohibited at the intersection area while the lattice rotation is triggered to form high angle grain boundaries (i.e. HAGBs) for DBs.

2. The orientation formed in the DBs is found to become harder since {111} slip planes in the DBs are much more likely to become perpendicular to the loading direction. Hence, the orientation formed in DBs can be estimated according to its initial grain orientation and the primary slip field calculated from the CPFE modelling.

3. Various factors, including crystal orientation, strain level, neighbouring grains and slip direction, have an impact on the formation of DBs by affecting the primary slip field. DBs are formed preferentially in grains whose primary slip field rather than effective strain field reaches to the activation value.

4. The value of the primary slip field has a strong correlation with the area fraction, aspect ratio (i.e. a/2c) and the density of formed DBs in deformed single crystal and multi-crystal pure aluminium alloys.

4 How would the DBs affect recrystallization?[3]

4.1 Graphical Abstract
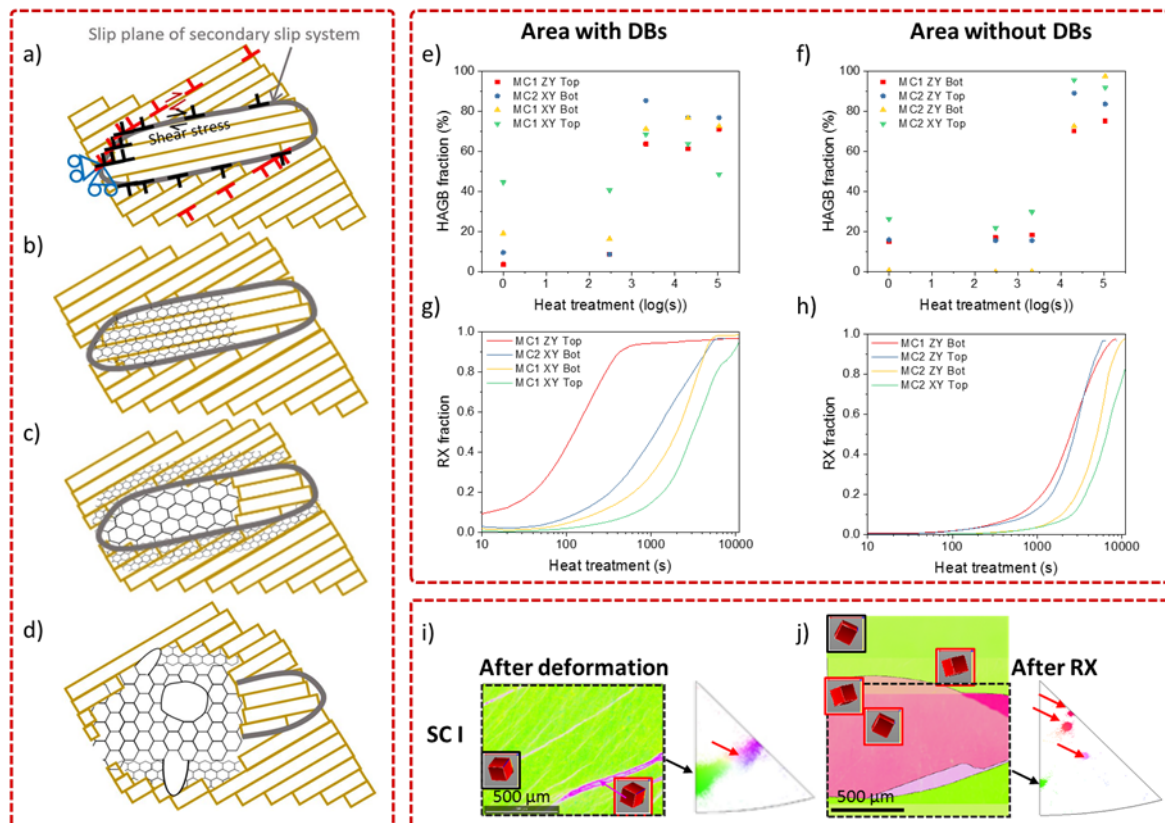
Figure 30 *Graphical abstract to show the effect of DBs for the occurrence of RX regarding the RXed grain orientation, positions for the grain nucleation and the rate of RX process.*

---

[3] The work in this chapter is under review at Acta Mater.

4.2 Introduction

As stated in the previous chapter, it is essential to fully understand how the grain nucleates on the basis of the heterogeneous deformed microstructure at the grain-level through experiments, since the key factors, such as nucleated positions, nucleated orientations and the number of nucleated grains, are all determined at this stage for the RX process [10,17,22,55,110]. In plastically deformed alloys [10], a larger number of deformation bands (DBs) discussed in Chapter 3 which can effectively accommodate the plastic strain and give rise to the heterogeneities in microstructure [40] were observed. Furthermore, a higher magnitude of dislocation density was found near the grain boundaries due to the prohibition of dislocation transmission from the neighbouring grain [111,112]. Therefore, both DBs and grain boundaries could be the potential nucleated sites for RX [3,22].

In this chapter, the electron back-scattered diffraction (EBSD) maps of the deformed samples are directly imported into the Kobayashi, Warren and Carter (KWC) phase-field model [61] as the deformed microstructure for the occurrence of RX. Moreover, this KWC phase-field model combines sound physical concepts for the prediction of RX process which is unlike the empirical approaches and probabilistic based models, such as Monte Carlo Potts model [20,21,113] and cellular automata model [72,114]. In this model, the concept of energy minimisation is written as a physically-based thermodynamic equation for the prediction of microstructural evolution during annealing. It includes the energy from dislocations, misorientations, grain boundaries and gradient field of phases. The arbitrary grain boundary geometries and their evolution with physical time step and length scale are simulated well by this model for the whole RX process.

Through combining the microstructural characterization and phase-field modelling, this chapter aims to quantitatively address this crucial problem by analysing: the effect of orientations in DBs on the RXed texture formation; the competition between DBs and grain boundaries on the nucleation sites; the effect of DBs on the rate of RX process. The comprehensive quasi-in-situ EBSD study on the evolution of grain orientation would provide insights into this problem. Initially, the experimental observations on the grain nucleation regarding nucleated positions and nucleated orientations can be written as nucleation laws in

the KWC phase-field model. Next, the experimental EBSD results for the RX process are capable of validating the simulated RX kinetics by KWC phase-field model.

In this chapter, deformed multi-crystals and single crystals of pure aluminium were heat-treated at 450 ℃ for different times to capture and predict the whole RX process with the aid of quasi-in-situ EBSD technique and KWC phase-field modelling. The experimentally observed and phase-field simulated grain nucleation and the subsequent grain growth are explained in as a unified manner.

4.3 Experimental methods and phase-field model

4.3.1 Materials preparation

This chapter used two types of uniaxial compressed pure aluminium to study the RX: one is $2\times2\times3.5$ mm^3 cuboid columnar multi-crystals (MC) with >99.9% purity; the other one is $10\times10\times10$ mm^3 cubic single crystals (SC) with >99.999% purity. MC samples were compressed to 20% and 30% engineering strain respectively; SC samples with four different orientations (i.e. SC I, II, III and IV) were compressed to 30% engineering strain (see Section 3.3.2 [40] for details of compression tests).

The interrupted heat treatments for the deformed samples were carried at 450 ℃ for different times, i.e. 0, 5, 35, 335 and 1775 min, in the furnace and followed by cold water quenching. The samples after each heat treatment were prepared for electron backscatter diffraction (EBSD) analysis by metallographically grinding with SiC papers (up to 1200 grit), then polishing with ~50 nm OP-S (Oxide Polishing Suspensions) and finally electropolishing for 40s in a solution of 9.5 vol% perchloric acid in ethanol at room temperature and 20 V.

4.3.2 Characterisation

Optical microscope (OM) and EBSD were applied for the microstructural characterisation. After each heat treatment, EBSD maps were captured at the same position using a Hitachi S3400N with Bruker eFlashHR EBSD Esprit v2.1 system. An accelerating voltage of 20 kV and a step size of 3 μm were applied for the EBSD mapping.

4.3.3 KWC phase-field modelling

4.3.3.1 Grain nucleation

The assumption of site-saturated nucleation [64] validated by Lauridsen et al. [115] was applied in this work to simulate the grain nucleation. It means that all nucleation events of RX effectively occur at the start of RX.

To find the possible nucleation sites, the stored energy distribution was calculated by Equation (16) based on the map of geometrically necessary dislocations (GNDs) obtained from the EBSD technique. The GND distribution was estimated using the method of the total line energy minimization described by Pantleon [116]. The lower bound of the GND density was estimated from the lattice rotation gradients calculated by the misorientation between the probe and its neighbouring points [116,117].

Since the high stored energy is the essential condition for the occurrence of RX [3], a critical stored energy E_c of 0.07 MPa µm^{-1} was chosen for the occurrence of grain nucleation. Also, a Gaussian distribution of misorientations of 40°−60° between the nuclei and original grains were assigned for the nuclei in this nucleation model based on the EBSD results (see Appendix C Figure C4) and literature [118]. In addition, the grain diameter of the initial nuclei was set as 30 µm which was ~2% to the parent grain diameter and the minimum distance between two neighbouring nuclei was set to be 60 µm. In this work, the nucleation sites were not limited to the grain boundaries which is significantly different from the previous simulation work [18,23]. Instead, the dislocation density is considered as the main cause of grain nucleation which causes the lattice rotation and the stored energy.

4.3.3.2 Grain growth

The KWC phase-field model [110] with two variables [22,119] was applied to simulate the grain growth of RX. The first variable, η, was set to be 0 for deformed grains and 1 for recrystallized grains. The second variable, θ, was the value of ϕ_2 extracted from the Euler angle $[\phi_1, \Phi, \phi_2]$ since the model was performed in two dimensions.

The free energy that contains the variables η and θ is expressed by,

$$F = \int \left[\frac{\alpha^2}{2} |\nabla\eta|^2 + f_d(\eta) + f_e(\eta, \rho) + g(\eta)s|\nabla\theta| \right] dV \qquad (11)$$

Hence, the time evolution of η and θ is given by,

$$\dot{\eta} = M_\eta \left\{ \alpha^2 \nabla^2 \eta - \frac{\partial f_d(\eta)}{\partial \eta} - \frac{\partial f_e(\eta, \rho)}{\partial \eta} - \frac{\partial g(\eta, \rho)}{\partial \eta} s |\nabla \theta| \right\} \tag{12}$$

$$\dot{\theta} = M_\theta \frac{1}{\eta^2} \nabla \left[g(\eta) s \frac{\nabla \theta}{|\nabla \theta|} \right] \tag{13}$$

$f_e(\eta, \rho)$ in Equation (13) is the homogeneous bulk free energy term [63] expressed as,

$$f_e(\eta, \rho) = f_e^r(\rho) p(\eta) + f_e^m(\rho)(1 - p(\eta)) \tag{14}$$

where $f_e(\eta, \rho)$ is an interpolation function that combines the free energy of the deformed phase $f_e^m(\rho)$ and recrystallized phase $f_e^r(\rho)$. $p(\eta)$ is a weight function used to smooth the density inside the interface region defined as,

$$p(\eta) = \eta^3 (10 - 15\eta + 6\eta^2) \tag{15}$$

The free energies in deformed phase and RXed phase, $f_e^m(\rho)$ and $f_e^r(\rho)$, were calculated according to its dislocation density. The free energy in the recrystallized phase is set to be zero, i.e. $f_e^r(\rho) = 0$, as the dislocation density in the RXed grain is around five orders smaller than that of the deformed grain [55]. The free energy in the deformed phase, $f_e^m(\rho) = 50E_{store}$, has been chosen where the stored energy, E_{store}, per unit length (i.e. per micrometre) of a deformed alloy is given by Reed-Hill et al. [120],

$$E_{store} = 0.5\rho G_{12}b \tag{16}$$

where ρ is the dislocation density, G_{12} is the shear modulus and b is the Burger's vector magnitude of aluminium alloys.

The interfacial energy term [63], $f_d(\eta)$, in equation (11) is expressed as,

$$f_d(\eta) = Wq(\eta) \tag{17}$$

$$q(\eta) = \eta^2 (1 - \eta) \tag{18}$$

$$W = \frac{6\sigma a}{\delta} \tag{19}$$

where $q(\eta)$ is a double-well potential that has minima at 0 and 1, and W is the depth of the energy wall. Both of $q(\eta)$ and $p(\eta)$ are used to construct the homogeneous free energy density $f_e(\eta, \rho)$ [63]. The double-well coefficient, W, is modified by adjusting the grain boundary thickness, δ, and grain boundary energy, σ.

The gradient energy term, $\frac{\alpha^2}{2}|\nabla\eta|^2$, gives rise to the diffuse interface in the phase-field model. The gradient coefficient, α, in Equation (11) is a constant associated with δ and σ expressed as,

$$\alpha = \sqrt{\frac{3\delta\sigma}{a}} \tag{20}$$

where $a = 2.20$ for an interface region with $\eta \in [0.1, 0.9]$. The grain boundary thickness is given based on the theory of diffuse interface approach [63] by,

$$\delta = 4\Delta x \tag{21}$$

where Δx is the grid size. The gradient coefficient, α, and the double-well coefficient, W, were correlated directly to physical properties, such as grain boundary thickness, δ, and grain boundary energy, σ [63].

The orientation energy term, $g(\eta)s|\nabla\theta|$, in Equation (11) is given by,

$$g(\eta) = \eta^2 \tag{22}$$
$$s = \frac{6\sigma}{\pi} \tag{23}$$

where the function $g(\eta)$ is used to eliminate the effect of misorientation inside the deformed grain. The constant s is related to the interface energy, σ.

The mobilities of η and θ are expressed as M_η and M_θ. M_η that considers steady grain growth in a one dimension problem [55] is given by,

$$M_\eta = M_0 \exp\left(-\frac{Q}{RT}\right) = M_0 \exp\left(-\frac{Q'}{k_B T}\right) \tag{24}$$

where M_0 is a pre-exponential factor, Q and Q' are the activation energies, R is the gas constant, T is the annealing temperature and k_B is the Boltzmann constant.

The mobilities used to define the rate of change in grain orientation are defined as,

$$M_\theta = (1 - p(\eta))M_\theta^0 \tag{25}$$
$$M_\theta^0 = M_\eta \tag{26}$$

The grain growth of nucleated grains driven by the stored energy follows the time-evolution of η and θ as described by Equation (12) and (13). The evolution of the 2D microstructure is solved using finite difference, with an eighth-order scheme for the spatial derivatives and the

Euler Forward method for time integration. The physical parameters used in the phase-field model to simulate the RX of deformed SC and MC pure aluminium at 723 K (i.e. 450 ℃) are listed in Table 6.

Table 6 *Material properties of SC and MC on the KWC phase-field model*

Grit size (Δx)	2 μm
Grain boundary energy (σ)	0.6 J/m^2
Boltzmann constant (k_B)	1.381×10^{-23} J/K
Constant for barrier height (a)	2.20
Activation energy (Q')	2.08×10^{-19} J
Time step (Δt)	0.01 ms
Pre-exponential factor (M_0)	3.1×10^7 m^3/(N ms)

4.4 Experimental results

4.4.1 Grain nucleation and grain growth

The deformed columnar multi-crystals and single crystals were applied to study the RX regarding the nucleation positions, nucleated grain orientations and grain growth since the effect of underlying grain orientations on the nucleated grain orientations can be avoided.

To reveal the microstructural evolution of deformed MC1 and MC2 at 450 ℃ after different annealing times, the EBSD inverse pole figure (IPF) maps regarding its loading direction, i.e. Y-axis, and their corresponding kernel average misorientation (KAM) maps are plotted in Figure 31. The deformed matrix mainly recovered within 5 min annealing, i.e. dislocation annihilation and arranging into dislocation walls to reduce the stored energy, thus, reducing the overall KAM values.

For the XY face of MC2 after 5 min annealing, a very beginning of grain nucleation is observed in DBs (see Figure 31 a2)), showing lots of compact unstable nuclei on its KAM map. After 35 min annealing, stable nuclei with high misorientation on its boundaries are found in the area with DBs. For the area without DBs, such as the top half of XY and ZY faces of MC2, no grain nucleation is observed in these regions.

With further annealing to 335 min and 1775 min (see Figure 31 c)-d)), the nucleated grains near DBs are found to grow into the deformed matrix while the initial grain boundaries are

quite stable without obviously changing their shapes during annealing. The newly formed grain boundaries are noticed to have much higher mobility compared with the initial grain boundaries.
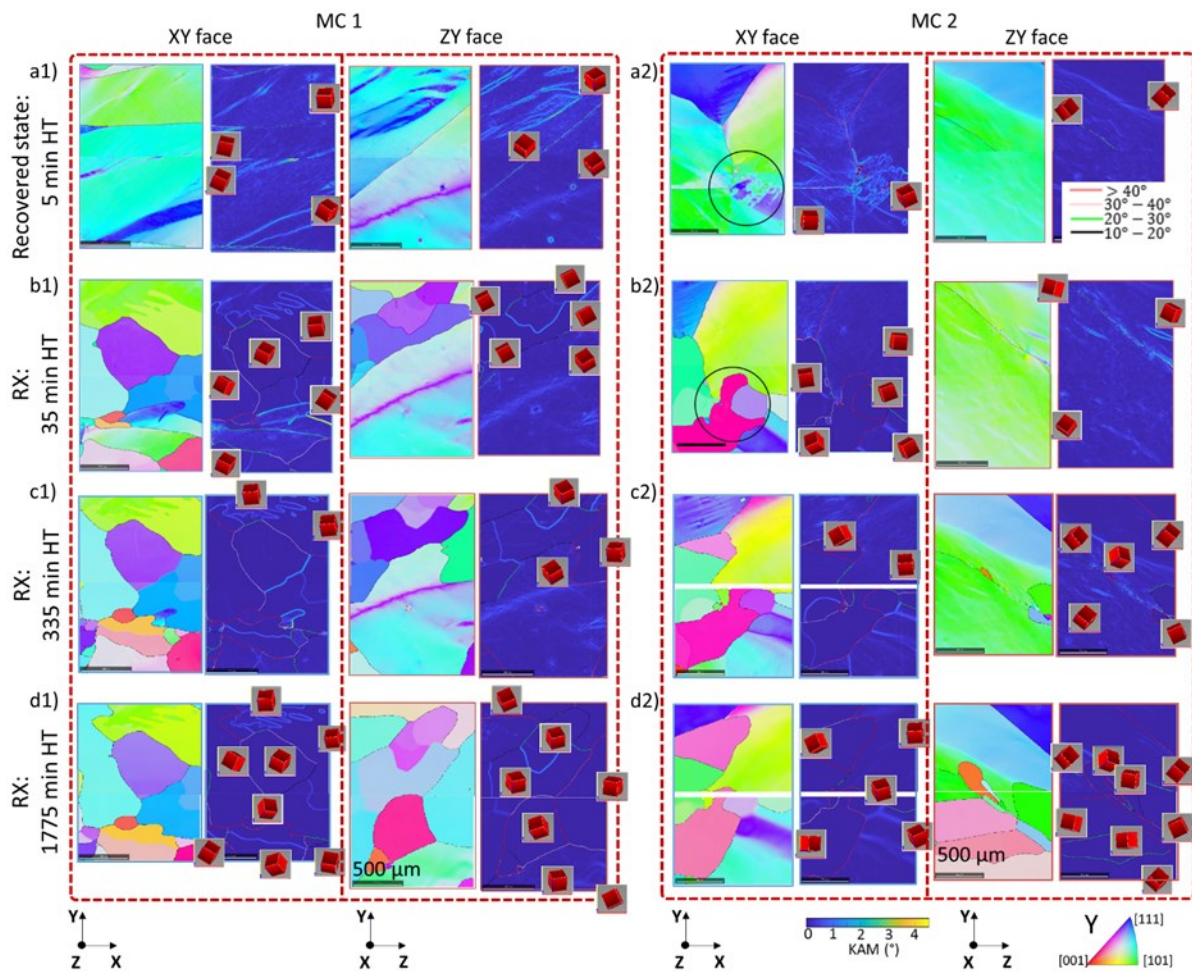
***Figure 31** a-d) are the EBSD IPF-Y maps and their corresponding KAM maps to show the microstructure evolution on the XY and ZY faces of deformed MC1 and MC2 during the heat treatment at 450 ℃ for 5, 35, 335 and 1775 min. The crystal orientation information (i.e. red cubes) at each position is superimposed in the KAM maps. Also, the misorientation on grain boundaries is marked out in KAM maps.*

The grains nucleated in the area with DBs can grow into 3D, for instance, the grains nucleated on the XY face of MC2 are found to grow into the ZY face (see Figure 31 c2) and d2)). Therefore, to study the nucleated grain positions and the relation between nucleated orientations with the matrix, it is important to do the observations at the early stage of grain nucleation rather than the stage of grain growth, such as 5-35 min annealing in this work, as the observed RX grains could nucleate at somewhere else.

The EBSD IPF-Y maps for SC I-IV before and after annealing are shown in Figure 32 where Y-axis is the uniaxial deformation direction. It has been seen that four SCs all completed the RX process within the 5 min heat treatment, while less pure MCs only finished recovery under same conditions (see Figure 31 a1) and a2)). The SCs completed the RX process rapidly due to the absence of solutes which would retard the rate of RX.
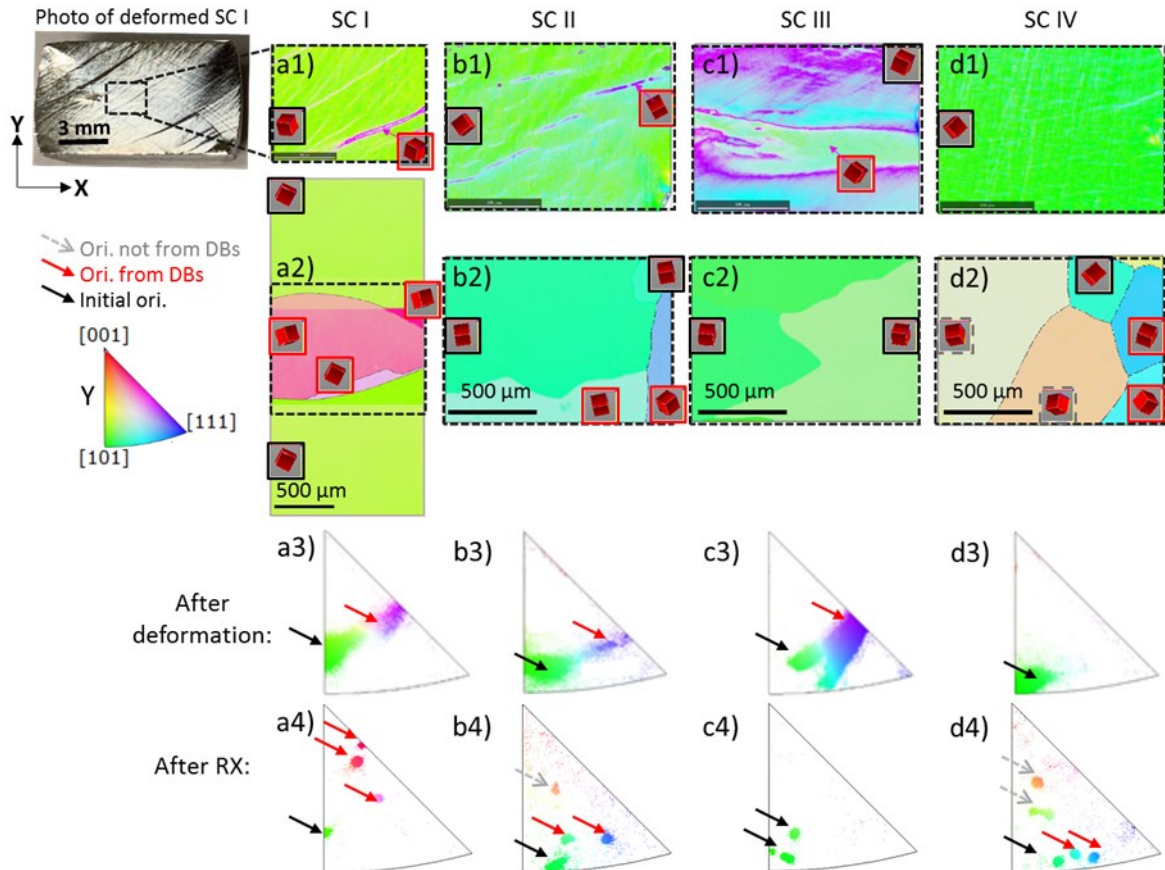
Figure 32 a1)-d1) and a3)-d3) are the IPF maps and IPFs-Y for the deformed SC I-IV. a2)-d2) and a4)-d4) are the IPF maps and IPFs-Y for the SC I-IV heat-treated for 5 min at 450 ℃. In the IPFs, the initial orientations are marked out by black arrow, RXed orientations from DBs are marked out by red arrow and RXed orientations not from DBs are marked out by grey dashed arrow. The crystal orientation information (i.e. red cubes) at each position is superimposed in the IPF maps. The border colour of the red cubes keeps consistent with the colour legend for arrows.

4.4.2 Recrystallized texture

To study the texture evolution due to RX, the IPFs on the XY and ZY face of the deformed MC1 and MC2 are analysed at each stage of heat treatments (see Figure 33), in which: the orientations from initial grains are labelled out as black arrows; the RXed orientations from

DBs are labelled as red arrows; the distinctive RXed orientations which have no relation with the deformed matrix or DBs are labelled as grey dashed arrows with grey circles. Since many RXed orientations are found to be quite close to the DBs (see Figure 31 and Figure 33), it has demonstrated that the orientation in DBs is a major source of orientations for RXed grains in MCs.

Through comparing the IPFs of deformed and RXed SCs in Figure 32, it is rational to conclude that the RXed orientations are partly originated from the orientations in DBs. The transitional distribution of orientation in DBs is likely to split into a few distinct orientations with misorientation ~10° during annealing, as shown in the evolution of IPFs on the XY face of MCs (see Figure 33 a1) and a2)). Apart from the orientations originated from DBs, some distinctive RXed orientations are also observed in MCs which are clearly neither from the initial grain orientation nor the DBs.
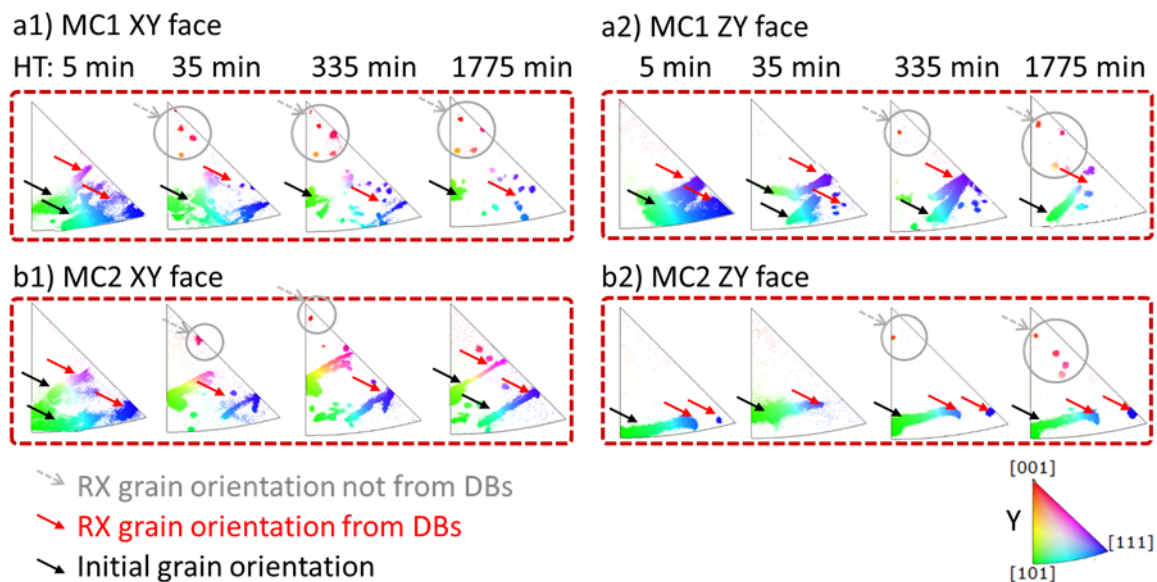
Figure 33 a1) and a2), b1) and b2) show the evolution of IPF-Y on the XY and ZY face of the MC1 and MC2 annealing for 5, 35, 335 and 1775 min at 450 ℃.

4.4.3 Distinctive recrystallized grain orientations

In an association of Figure 31 and Figure 33, it can be seen that the distinctive RXed orientations in Figure 33 are mainly located at the bottom edge of the specimen as shown in Figure 31 which is the contacting area during compression.

To make sure that those distinctive orientations were generated at the edge of the specimen, extra EBSD maps for MC1 and MC2 were taken at the bottom edge area of the ZY faces after 35 and 1775 min annealing (shown in Figure 34). The contacting area with the compression stage is marked out by an array of black slashes in Figure 34. It has been seen that nearly all the distinctive RXed orientations are found in this bottom edge area. For example, in MC2 (see IPF-Y in Figure 34 b), the distinctive orientations are labelled by red colour. In comparison, all the RXed grains with red colour in MC2 are located near the contacting area of compression.

Furthermore, as shown in the KAM maps in Figure 34, the grain boundaries of distinctive RXed grains are found to have high misorientation >40°. Through comparing a1)-a2) and b1)-b2) in Figure 34, these grains at the bottom edge area are found to grow quickly into the inside of the specimen during annealing.
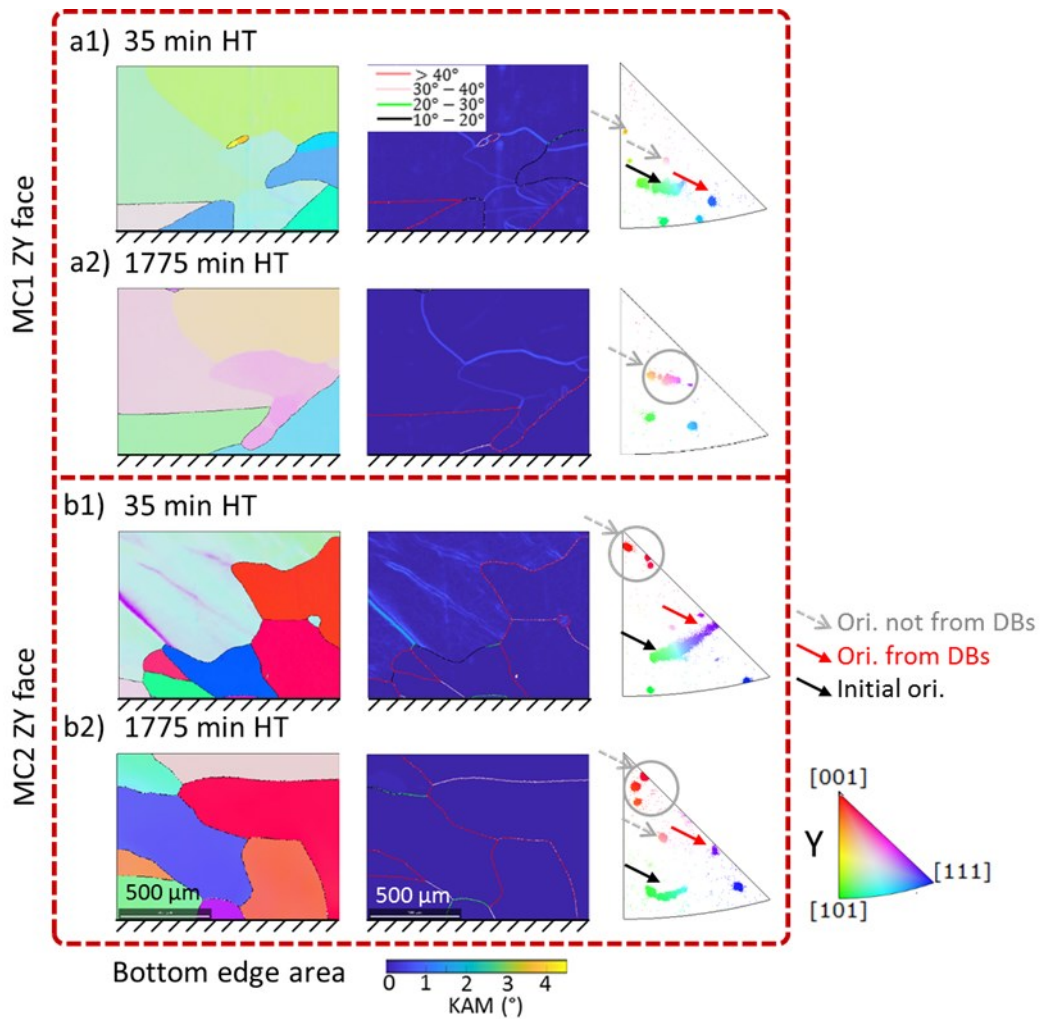
Figure 34 *a1)-a2) and b1)-b2) show the IPF-Y maps, KAM maps and IPFs-Y of the bottom edge area on the ZY face of MC1 and MC2 respectively. The misorientations on the grain boundaries are marked out by colours in KAM maps.*

4.5 Quantitative analysis

The whole XY and ZY face of the MC1 and MC2 are separated into two areas, i.e. top and bottom area, to quantitatively analyse the effect of DBs on the grain nucleation (see Figure 35) and grain growth (see Figure 37).

4.5.1 Observed grain nucleation

The microstructure of each area after 0, 5, 35, 335 and 1775 min annealing at 450 ℃ are analysed respectively for the evolution of grain size, high angle grain boundary (HAGB) fraction and the number of grains. The eight EBSD maps for the top and bottom area are divided

into two groups: one group is the area with DBs (see the left column plots in Figure 35, including the bottom area of the XY face in MC2, the top area of the ZY face in MC1, the bottom and the top area of the XY face in MC1); the other group is the area without the existence of DBs (see the right column plots in Figure 35, including the bottom area of the ZY face in MC1, the whole ZY face and the top area of the XY face in MC2).

The sudden change of the grain diameter, HAGB fraction and the number of grains indicates the occurrence of RX [121]. By comparing the left and right columns in Figure 35, it can be seen that notable RX was found at 35 min annealing in the areas with DBs while no obvious RX was found in the areas without DBs. By contrast, the change of grain size and HAGB fraction was found at 335 min in those areas (see Figure 35 a2)-b2)), showing that the RXed grains were found much later in the areas without DBs than the areas with DBs. These observations are also verified by the grain structure maps shown in Figure 31.

It also has been found in Figure 35 that the RX process would result in the decrease of average grain diameter (i.e. the increase of the number of grains and the increase of HAGB fraction) in pure aluminium. The slight increase of grain diameter and drop of HAGB fraction from 335 min to 1775 min annealing are attributed to the grain growth of nucleated grains in the early stage of annealing.
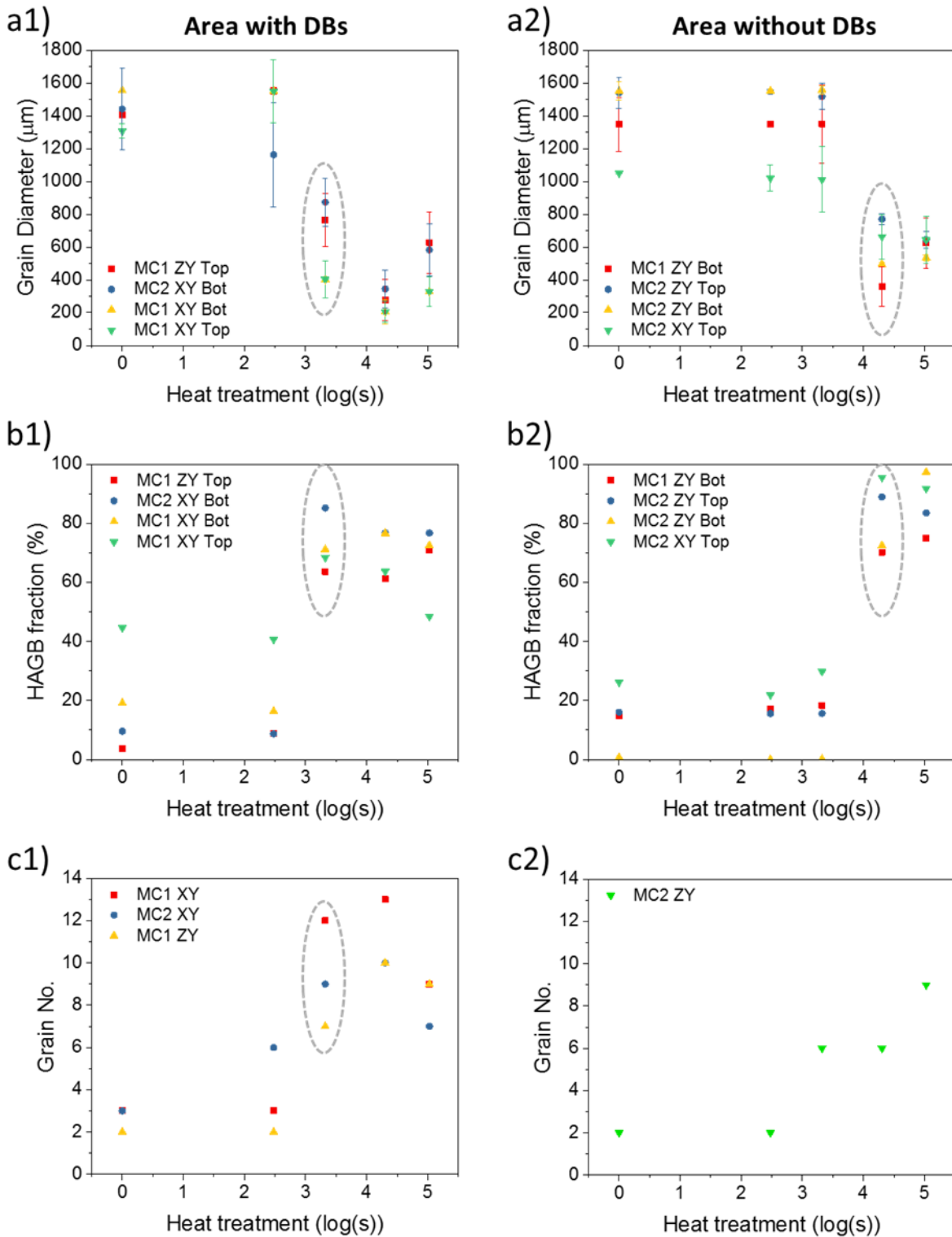
Figure 35 *a1)-b1) and a2)-b2) show the evolution of grain diameter and HAGB fraction in the areas with and without distinct DBs; c1) and c2) show the evolution of the total number of grains on the faces with DBs and the face without DBs. The values with obvious changes during annealing are circled out in plots. The colour order in the legend keeps consistent with the order of DBs area fraction from high to low.*

4.5.2 Simulated grain nucleation

The grain nucleation was simulated based on the nucleation laws discussed in Section 4.3.3.1 to generate the heterogeneous distribution of nucleated grains as shown in Appendix C Figure C4. In Figure 36, the number of simulated nucleated grains are compared with the misorientation angle and the area fraction of DBs measured from EBSD maps for each face of MC. The nucleated grain number is found to be more closely correlated with the area fraction of DBs in comparison to the misorientation angle.
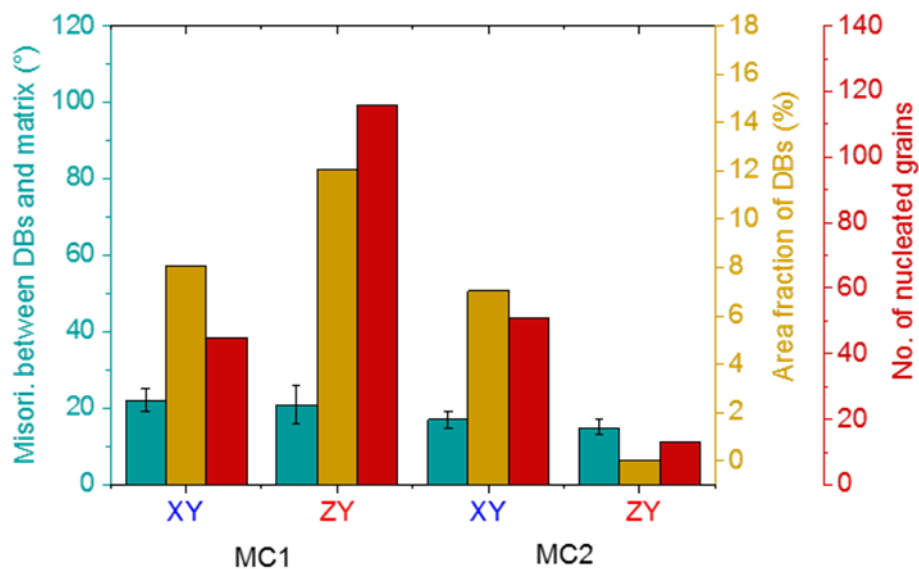
Figure 36 *Comparison of misorientation angle on the boundary of DBs and area fraction of DBs with the simulated nucleated grain no. on XY and ZY face of MC1 and MC2.*

4.5.3 Simulated grain evolution

The simulated microstructural evolutions are plotted in Figure 37 for the areas with and without the existence of DB. The coloured lines in the legend from top to bottom represent the descending order of the area fraction of DBs (i.e. from high to low). It can be seen from the simulations that the areas with a higher volume fraction of DBs show an earlier start and quicker finish of RX, i.e. lines from the left to right for the colour red, blue, yellow and green respectively in Figure 37.

The simulated RX process by this KWC phase-field model has a good agreement with the experimental observations by quasi-in-situ EBSD maps. For the areas with distinct DBs in MCs, it has been found that the RX mainly occurs around 1000 s (i.e. 16.7 min) and completes before 10000 s (i.e. 166.7 min) in both of experimental results (see Figure 35 a) and in simulation results (see Figure 37 a). However, for areas without distinct DBs, nearly none obvious RX is found around 1000 s (i.e. 16.7 min) in both of experimental results (see Figure 35 b) and simulation results (see Figure 37 b).
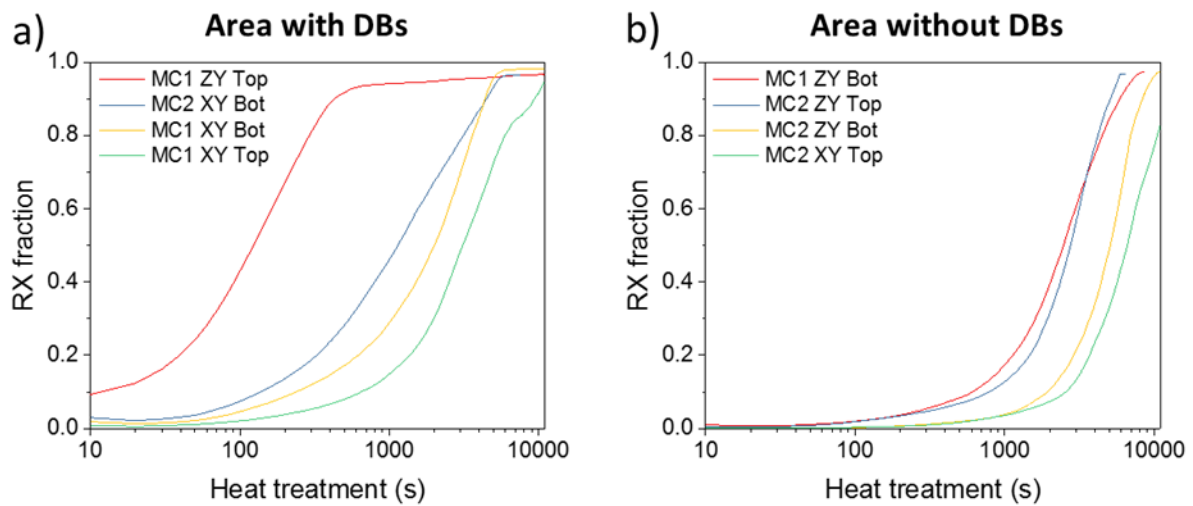
Figure 37 *a) and b) show the evolution of RX fraction in the areas with distinct DBs and without DBs. The colour order in the legend is consistent with the order of DBs area fraction from high to low.*

4.6 Discussion

4.6.1 Recrystallized orientations

According to the IPF evolution of the RX process in MCs (see Figure 33) and SCs (see Figure 32), it has been found that the majority of RXed orientations, which are a group of orientations with misorientation ~10° between each other, are originated from the orientation in DBs. Hence, orientation in DBs provides a source of orientations for RXed grains. In my previous work [40], it has been demonstrated that the orientations in DBs are rotated from the initial orientation whose {111} slip planes are likely to become perpendicular to the loading direction.

To study the source of RXed orientations, it is important to capture all deformed orientations for the analysis since the RXed grains nucleated at DBs would grow into the deformed matrix in 3D and can be found somewhere else. For example, the grains nucleated on the XY face of MC2 after 335 min annealing is found to grow into the ZY face along the initial grain boundary (see Figure 31 c2)).

Besides of the RXed orientations from DBs, some distinctive RXed orientations, which are apparently with no relation to the orientations of DBs and deformed matrix, are observed in the RXed microstructure (see Figure 31 and Figure 33). After checking the RXed microstructure near the compressive edge of samples, it has been found that nearly all these distinctive orientations are located near the contacting area with the compression stage in Figure 34.

The distinctive RXed orientations are formed likely due to the compressive friction at the contacting area of the specimen with the compression stage. The unavoidable localised friction could distort the lattice structure and create new orientations at the contacting layer during the compression [121]. These fresh orientations are found to have high misorientations >40° at the grain boundaries (i.e. HAGBs) and could grow fast into the matrix during annealing (see Figure 34) since the HAGBs have been demonstrated to have much higher mobility compared with LAGBs (i.e low angle grain boundaries) [122,123]. Additionally, the edge of the specimen apparently has a higher heating rate compared with the inside of the specimen when the heating is conducted in the furnace. The grains near the edge, therefore, would have a higher driving force for the grain growth compared with the inside grains at the beginning of heating.

In summary, the RXed grain orientations are generated from two sources: one is from the DBs; the other one is from the contacting edge of the specimen due to compressive frictions.

4.6.2 Grain nucleation

The quasi-in-situ EBSD maps of deformed MC1 and MC2 in Figure 31 clearly show the positions of grain nucleation in deformed pure aluminium. It has been seen that the nucleated grains are more likely to nucleate in the DBs after 35 min annealing at 450 ℃, rather than at the initial grain boundaries. Thus, it has been demonstrated in this chapter that initial grain boundaries, compared with DBs, are not favourable nucleation sites for pure aluminium. This finding is against many discussions in previous studies from which only grain boundaries are considered for the grain nucleation [9,10].

Instead, the initial grain boundaries act quite stable during heat treatment without incubating new grains and having obvious movements. This stable characteristic could also demonstrate that the initial grain boundaries are not potential sites for the grain nucleation at the early RX. Even though the misorientation angles on initial grain boundaries are high, the neatly arranged dislocations on the initial boundaries would make newly formed dislocations during deformation hard to move across them. Therefore, in comparison to DBs, the initial grain boundaries are not potential sites for nucleation. By contrast, they act as barriers for the nucleated grains to grow across. For those few RXed grains observed near the grain boundaries after longstanding annealings, such as the small grains found in the ZY face of MC2 after 335 min annealing shown in Figure 31 c2), they could be attributed to the growth of RXed grains which nucleated in DBs since their orientations are quite close the orientation of DBs.

The RXed grains once nucleated in DBs would grow into the deformed matrix and reduce the stored energy of the system during further annealing. That is why the RXed grains with the orientations close to DBs are also found in the area without DBs but with much longer annealing (as shown in the plots of Figure 35). Therefore, it is rational to conclude that the grain nucleation in the deformed pure aluminium prefers to occur at the DBs which contains both high orientation gradients and heterogeneous strain distribution.

According to this finding, assumptions for the simulation of grain nucleation made in many previous computational models [13,55] need to be revised, which only considered the grain boundaries as the potential nucleation sites for the RX simulation. The dislocation structure particularly the DBs should be taken into account for the simulation of grain nucleation.

The effect of DBs on grain nucleation has been studied in Figure 36. The number of nucleated grains is found to have a correlation with the area fraction of DBs while no obvious correlation is observed for the misorientation angle between DBs and deformed matrix.

4.6.3 Grain growth

As shown in Figure 31 and Figure 35, the grains nucleated in DBs are found to grow into the deformed matrix and sometimes grow along the initial grain boundary during further annealing. The kinetics of grain growth is checked for all the areas with and without distinct DBs by experimental EBSD analysis (see Figure 35) and KWC phase-field modelling (see Figure 37).

It has been validated by the series of EBSD maps that this model has successfully simulated the whole RX process for all areas on MC1 and MC2 regarding the annealing time.

The kinetics of grain growth has also been found to have a strong correlation with the area fraction of DBs. As shown in Figure 37, the areas with DBs are found to finish the RX process much earlier than the areas without distinct DBs, i.e. the higher the area fraction of DBs is, the quicker the RX process could finish. Since the grain nucleation prefers to occur in the DBs, more nucleated grains would be found in the area with DBs resulting in a faster evolution of the RX fraction. This positive correlation between the number of nucleated grains and the area fraction of DBs has been demonstrated in Section 4.6.2 about grain nucleation.

4.6.4 Interaction of deformation bands and recrystallization

Through capturing the microstructural changes of the whole deformed area by quasi-in-situ EBSD maps for SCs and MCs, it has been observed that the grain nucleation is likely to initially occur inside the DBs and grow into the deformed matrix. Such that, RX in the area with DBs is found to be much quicker than the area without DBs.

The mechanism of RX in grain level is summarised in Figure 38 to explain the above observations of RX process at the existence of DBs for pure aluminium. The sequence of a)-d) in Figure 38 shows the four steps in the course of RX: a) the formation of DBs in plastically deformed crystal as a result of the intersection of two types of activated slip systems (i.e. red and black symbol), as well as the dislocation pile-up at the intersection area [40]; b) the formation of unstable subgrains inside the DBs due to the substantial dislocations blocked in the DBs. This step is recognised as the initial recovery during annealing.

Figure 38 c) shows the formation of HAGBs due to the growth of subgrains, as well as the formation of subgrains at the outer layer of DB. The formation of subgrains at the outer layer of DB is slower than the inner layer of DBs since the outer layer contains less blocked dislocations, thus, requires more incubation time for the formation of subgrains [3,124]. In order to eliminate the excess dislocations at subgrain walls, the larger RXed grains formed in DBs are likely to consume the later formed subgrains at the outer layer of DBs following the mechanism of strain-induced boundary migration (SIBM) discussed in [9]. The orientations of RXed grains in Figure 33 which are found to be close to the orientations in DBs can be treated as a proof for this phenomena.

Figure 38 d) shows the combination of RX, grain growth by the SIBM [27] and subgrain boundary migration [28,29]. It contributes to the primary and secondary grain growth for the development of final microstructure [3].
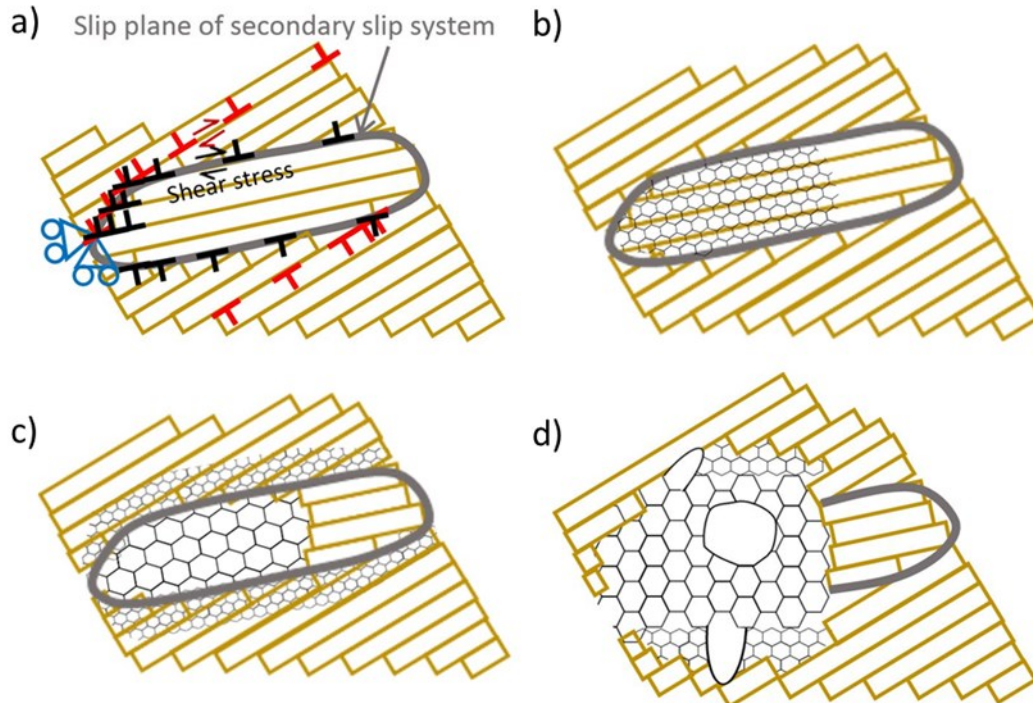
Figure 38 Schematics to show each step of RX process: a) the formation of DB due to slip band intersection and dislocation pile-up at the intersection area; b) initial recovery for the formation of unstable subgrains in the DB; c) RX for the formation of HAGBs and later recovery at the outer layer of DB; d) RX and grain growth during annealing.

4.7 Summary

In this chapter, the quasi-in-situ EBSD maps of the whole deformed sample surface are applied to study how the DBs affect the RX in deformed pure aluminium. Geometrically necessary dislocation density (GND) maps together with the orientation information are directly imported to the KWC phase-field modelling to predict the grain nucleation and grain growth. It has been found that:

1. The orientation of DBs is demonstrated as a major source of orientations for RXed grains which would contribute to the final RXed texture.

2. The grain nucleation prefers to occur in DBs compared with the initial grain boundaries since the developed DBs contains more unstable dislocations than the initial grain boundary.

3. Demonstrated by both of experiments and modelling, the areas with higher area fraction of DBs are found to complete the RX process much quicker than the area without DBs since DBs would provide more potential nucleated sites and less incubation time for RX.

4. In KWC phase-field modelling, the number of nucleated grains has a strong positive correlation with the area fraction of DBs while no obvious correlation is found for the misorientation angle.

5 Combining EBSD with modelling for RX in 1050A[4]

5.1 Graphical abstract
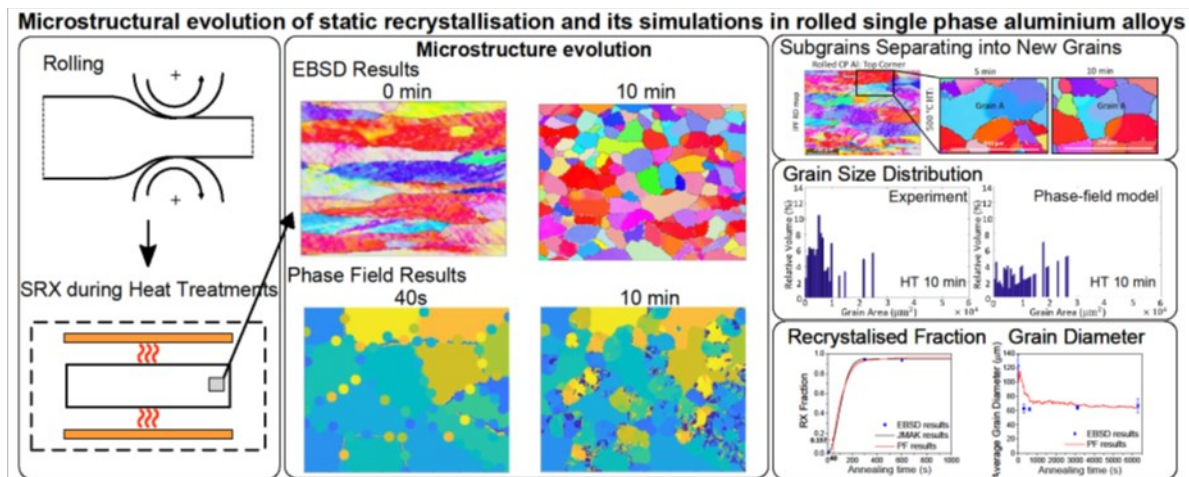
Figure 39 *Graphical abstract to show the accurate prediction of RX process through combining CPFE and phase-field modelling in rolled polycrystalline pure aluminium 1050A.*

---

[4] The work in this chapter has been published in Computational Materials Science [110].

5.2 Introduction

The prediction on the deformed microstructure and occurrence of RX has been achieved in Chapter 3 and Chapter 4 respectively. However, there are still some problems remaining. Firstly, it is challenging to accurately predict the nucleated positions and orientations based on simulated deformed structure, primarily due to the problematic prediction on the dislocation distribution during plastic deformation. Furthermore, it is technically difficult to determine the incubation time and verify the relationship between incubation time, GND density and annealing time from experiments.

In this chapter, I applied a validated lengthscale-dependent CPFE model [57–59], adopted from Dunne et al. [60], to precisely simulate the heterogeneous distribution of local, grain-level, accumulated slip. My phase-field modelling presented here works together with theoretical JMAK equation offers a solution to this problem. Additionally, with regard to the prediction of texture evolution, the KWC phase-field model has the capability of generating orientations for nucleated grains from experimental observations, theoretical hypothesis and physical principles.

Regarding the methodology implemented herein, deformed polycrystalline pure aluminium 1050A was heat-treated at 500 ℃ for different times to capture the whole RX process by the quasi-in-situ EBSD technique. The heterogeneous deformed microstructure simulated by CPFE was imported into the KWC phase-field model for the simulation of grain nucleation and grain growth. The simulated evolution is quantitatively validated by the EBSD results regarding grain morphology and texture development.

The work in this chapter provides a versatile tool for many unsolved problems in manufacturing. For example, through changing the boundary conditions, e.g. the strain paths in the CPFE model and the temperature gradients in the phase-field model, the prediction of RX under complex strain paths and temperature gradients become feasible for the industry. Apart from this, the recrystallized microstructure can be input into a crystal plasticity model as the initial conditions in future work to achieve the prediction of the mechanical properties, such as the strength [125], ductility [126], creep [127], fatigue [128] and stress crack corrosion behaviour [129] of load-bearing components.

5.3 Methodology

5.3.1 Material preparation and quasi-in-situ EBSD characterisation

A rolled sheet of 1050A aluminium was supplied by Aalco Metals Ltd. The chemical composition is listed in Table 7. To study the SRX behaviour of cold rolled single phase aluminium, a rectangular plate 10 (RD)×10 (TD)×6 (ND) mm³ was cut from the rolled sheet, where RD is the rolling direction, TD is the transverse direction and ND is the normal direction for heat treatment.

Table 7 Chemical composition of 1050A

Element	Fe	Si	Zn	Mg	Ti	Mn	Cu	Other	Al
wt. % up to	0.40	0.25	0.07	0.05	0.05	0.05	0.05	0.03	Balance

The interrupted heat treatment of as received 1050A was carried out in a furnace at 500 ℃ and followed by cold water quenching. The RD-ND surface of cold rolled samples were ground using SiC paper to 1200 grit, then mechanically polished using 40 nm OP-S (Oxide Polishing Suspensions) diluted with H_2O to a ratio 1:5 of OP-S: H_2O for 3 min. Finally, the samples were electropolished for 60 seconds in a solution of 9.5 vol. % perchloric acid in ethanol at room temperature and 19.5 V, drawing a steady current density of around 0.9 A/cm².

Electron Backscattered Diffraction (EBSD) was performed in a Carl Zeiss Sigma 300 CrossBeam SEM with Bruker eSprit v2.1 software, using an aperture size of 120 µm and an accelerating voltage of 20 kV with a step size of 3 µm. The EBSD data was analysed using MTEX toolbox [130]. The EBSD scanned area was precisely relocated after further annealing to allow the scanning of the same area. The top, middle and bottom corners of RD-ND plane were quasi-in-situ imaged by EBSD after 0, 5, 10, 52, 105, 527, 1051 and 1667 min annealing at 500 ℃ followed by water quenching. After each heat treatment, the annealed sample was mildly re-polished by 40 nm OPS diluted with H_2O for 2 min and electropolished for 30 seconds. The thickness reduction due to re-polishing was less than 1 µm.

5.3.2 Crystal plasticity finite element (CPFE) model

In the CPFE model explained in Chapter 3, Taylor's dislocation hardening rule for polycrystalline pure aluminium 1050A shown in Equation (8) has been modified to consider both SSD and GND as follows

$$\tau_c^\alpha = \tau_{c0} + \mu \cdot G_{12} \cdot b \cdot \sqrt{\rho_{GND} + \rho_{SSD}^S} \tag{27}$$

where μ is the material constant for polycrystalline aluminium [131], ρ_{GND} is the geometrically necessary dislocation density and ρ_{SSD}^S is the density of sessile statistically stored dislocations.

The GNDs are the extra storage of dislocations to accommodate the lattice curvature due to the appearance of non-uniform plastic deformation [132]. The Nye's dislocation tensor to compute the GNDs is given by,

$$\Lambda = \text{curl}(\mathbf{F}^p) = \sum_{\alpha=1}^{12} \rho_{Gs}^\alpha \, \mathbf{b}^\alpha \otimes \mathbf{s}^\alpha + \rho_{Get}^\alpha \mathbf{b}^\alpha \otimes \mathbf{t}^\alpha + \rho_{Gen}^\alpha \mathbf{b}^\alpha \otimes \mathbf{n}^\alpha \tag{28}$$

where ρ_{Gs}^α are the screw dislocation components on slip system α with line vector along the slip direction $\mathbf{s}^\alpha$, ρ_{Get}^α and ρ_{Gen}^α are the edge dislocation components with line tangent vector along with the slip normal $\mathbf{n}^\alpha$ and $\mathbf{t}^\alpha$, $\mathbf{t}^\alpha = \mathbf{s}^\alpha \times \mathbf{n}^\alpha$ and $\mathbf{b}^\alpha$ is the Burgers vector on slip system α.

There are 12 ρ_{Gs}^α screw, 12 ρ_{Get}^α edge and 12 ρ_{Gen}^α edge dislocation components, resulting in a total of 36 independent GND components shown in Equation (28). Equation (28) may be written in a matrix form as,

$$\overline{\Lambda} = \mathbf{A}\rho_{GND} \tag{29}$$

where $\overline{\Lambda}$ is a 9×1 vector form of the Nye's dislocation tensor Λ, $\mathbf{A}$ is a 9×36 linear matrix containing the basis tensors $\mathbf{b}^\alpha \otimes \mathbf{s}^\alpha$, $\mathbf{b}^\alpha \otimes \mathbf{t}^\alpha$ and $\mathbf{b}^\alpha \otimes \mathbf{n}^\alpha$. This is an undetermined system of linear equations having infinite solutions. According to the discussion by Arsenlis and Parks [132], the L_2 norm is expressed as the sum of the squares of GND densities on each slip system to solve the minimisation problem [133]. The sum of GND densities is given by

$$\rho_{GND} = \sqrt{\sum_{\alpha=1}^{12} (\rho_{Gs}^\alpha)^2 + (\rho_{Get}^\alpha)^2 + (\rho_{Gen}^\alpha)^2} \tag{30}$$

The CPFE parameters to simulate the plastic deformation of polycrystalline pure aluminium 1050A are listed in Table 8. The initial critical resolved shear stress, τ_{c0}, and the isotropic hardening coefficient for ρ_{SSD}^S accumulation were calibrated using the experimental macroscopic stress-strain response of 1050A (see Figure 40 (b)). The other properties shown in Table 5, such as the magnitude of the Burger's vector, b, Boltzmann constant k, Helmholtz free energy, ΔH, and activation volume, ΔV, were obtained from the literature for pure aluminium [57,101].

Table 8 *Material properties of 1050A on CPFE model*

Young's modulus (E)	70 GPa
Initial slip stress (τ_{c0})	21 MPa
Material constant (μ)	0.22

A 3D CPFE model (shown in Figure 40 (a)) with the grain morphology and average grain diameter (~120 µm) of the rolled pure aluminium was applied to study the plastic deformation of the alloy 1050A. Twenty-noded brick finite elements with reduced integration (C3D20R) were used in the finite element model. The grain shape was generated by VGRAIN [134]. The grain orientations of 14 grains were determined based on the pole figure of 1050A (see Figure 48 a)) by choosing the first 14 dominating orientations with the maximum grain area in the deformed microstructure. Pole figures in Figure 48 a) and b) demonstrate that orientations in CPFE model have a good agreement with the experimental observations. The sample in the simulation was deformed up to 15 % compressive strain under plane strain compression conditions at room temperature to achieve the same amount of GND density of 1050A used in this study. The bottom, left, front and back surfaces are fixed in the model. The dimensions of the polycrystalline sample in the study are $760{\times}760{\times}50$ µm^3.
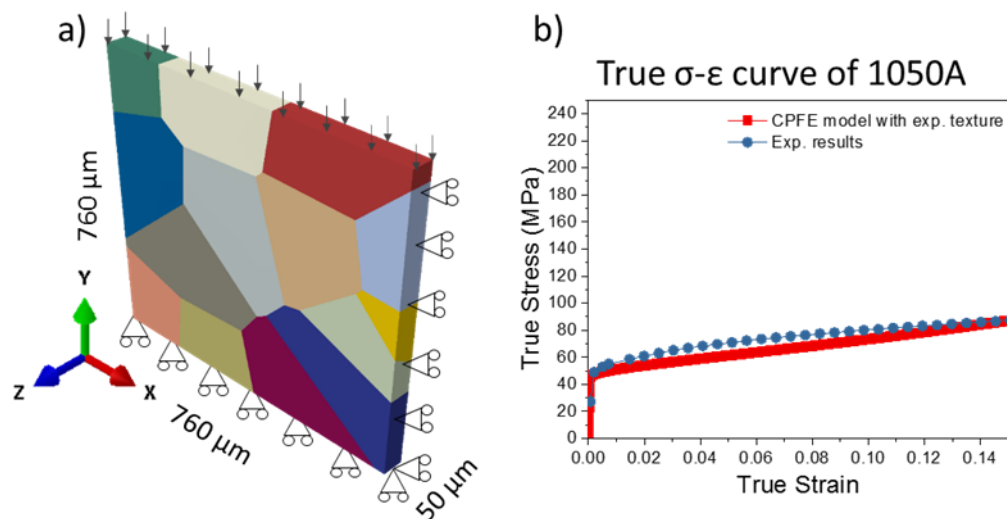
Figure 40 *a) CPFE model of 14 grains with the grain morphology of rolled pure aluminium before the plane strain compression along YY direction. b) The true stress-strain response of the CPFE model and tensile test* [135] *shows a perfect fit up to 0.15 true strain.*

5.3.3 KWC phase-field model

The KWC phase-field model introduced in Chapter 4 was applied to study the polycrystalline pure aluminium in this chapter. The crystal orientation and dislocation density (see Figure 41) from CPFE simulation was input for the phase-field model to calculate the grain nucleation and grain growth during RX. Due to the different grid size and irregular element shape, the dislocation density on the mid xy layer was extracted from CPFE model and then remapped using linear interpolation [17,136] before performing the phase-field modelling in 2D. The linear interpolation aims to ensure that the driving force is smoothly distributed within the interface region.
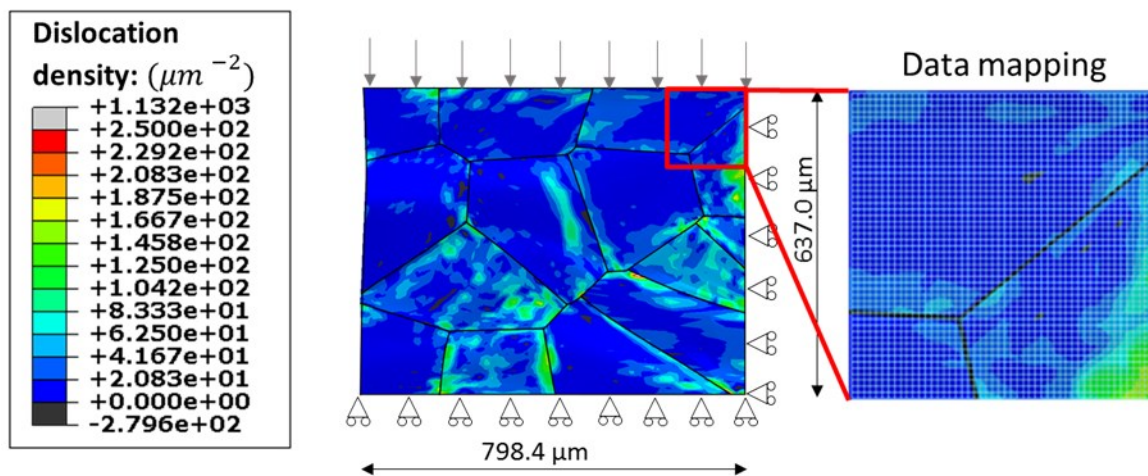
Figure 41 Dislocation distribution on the xy surface of the deformed CPFE model to 0.15 true strain, where the y-axes are the deformation axes. The simulation results on the elements with irregular shape were remapped to regular shape for the phase-field modelling.

5.3.3.1 Grain nucleation

In this chapter for polycrystalline pure aluminium, the misorientation angle was set to be more than 15° and E_c was defined to be 0.01 MPa μm^{-1} based on the stored energy distribution shown in Figure 42 a). The orientations of new grains were assigned based on the observations made for the deformed microstructure (shown in Figure 48).

In addition, the minimum distance between two neighbouring nuclei was set to be 50 μm and the grain diameter of seeds was set as 40 μm. The dislocation density ρ and phase distribution η after seeding are shown in Figure 42 b) and c). The initial area fraction of nucleated grains was simply calculated as the sum of area for nucleated grains, since the critical size of stable

nuclei and the number of possible nuclei were already obtained from EBSD maps and phase-field modelling respectively.
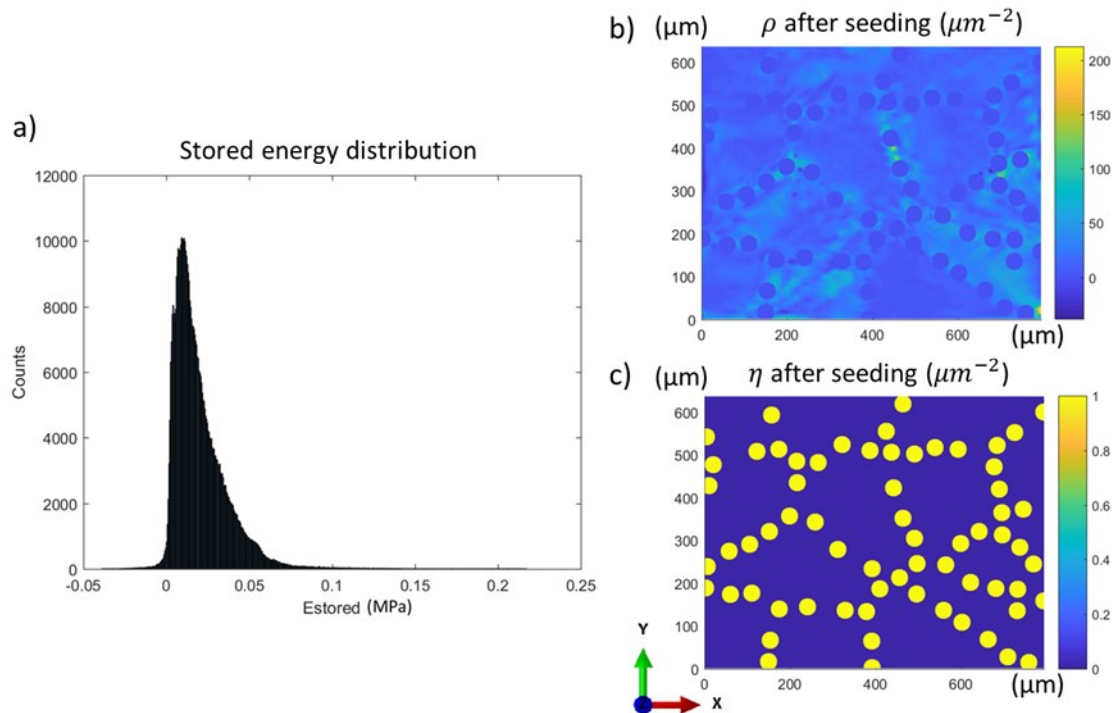
Figure 42 a) The histogram of stored energy calculated according to Equation (16); b) and c) are the dislocation density (ρ) distribution and phase (η) distribution after seeding. The dislocation density of recrystallized grains was assumed to be 0 μm^{-2}, and the dislocation density of the deformed grains was extracted from the CPFE model.

Regarding the incubation time required for the grain nucleation, there is no valid experimental method or computational model at present to accurately capture or calculate the time for the formation of stable nuclei. In this chapter, the phase-field modelling results were creatively plotted together with the validated theoretical JMAK curve for the comparison. The incubation time, therefore, can be directly estimated from the curve according to the initial area fraction of nucleated grains. This crucial parameter has been quantified for the first time by combining the theoretical JMAK curve with the computational method which both validated by experimental EBSD results.

5.3.3.2 Grain growth

The KWC phase-field model [22,119] explained in Section 4.3.3.2 was also selected to model grain growth in polycrystalline pure aluminium 1050A. The parameters used for the RX in

polycrystalline pure aluminium keep the same with SC and MC pure aluminium (see Table 6) while the annealing temperature used in this section is 773 *K* (i.e. 500 ℃).

5.4 Results

5.4.1 EBSD results

The quasi-in-situ EBSD maps at the top, middle and bottom corners of the cold-rolled pure Al RD-ND plane were applied to characterise the grain size, RX fraction, texture, GND distribution and fraction of high angle grain boundaries (HAGBs) during annealing [2].

5.4.1.1 Texture evolution

The quasi-in-situ inverse pole figure (IPF) EBSD maps taken for the rolling direction (RD) are shown in Figure 43 a). The maps of each row were captured from the same area. The corresponding pole figures (PF) at each corner but from a bigger area are plotted in Figure 43 c).

The evolution of the PF shows the change of texture at each corner during annealing. As shown in Figure 43 c), the texture varied slightly between the area near the edge of the rolled sample and the area in the middle, due to the different deformation states of the rolled sheet during rolling. However, the texture at each corner remained the same during the annealing no matter how long the RX occurred. This notable observation is an important support for the texture simulation in the phase-field model. The nucleated grains tend to keep the orientation of deformed grains in the pure aluminium, thus maintaining the texture.
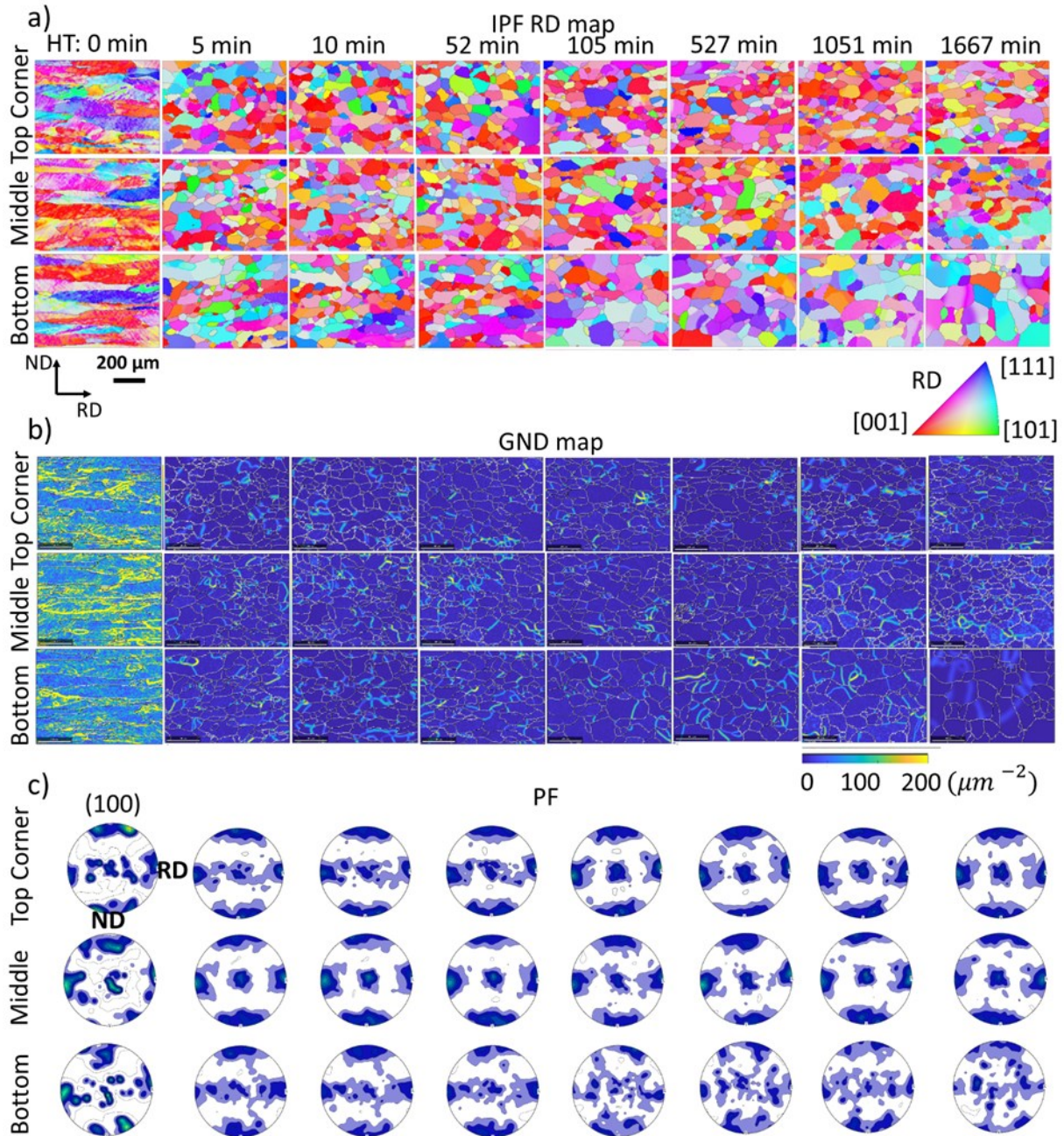
Figure 43 *EBSD a) IPF maps b) GND density maps and c) PF of cold rolled pure aluminium 1050A at the top, middle and bottom corners after 0, 5, 10, 52, 105, 527, 1051 and 1667 min annealing at 500℃. The rolling direction (RD) is horizontal, and observation along RD was applied to IPF triangle. The (001) pole figures are shown in the same orientation as the IPF maps.*

5.4.1.2 Grain size and HAGBs evolution

To calculate the average grain size of the recrystallized grains, the grains that have grain orientation spread (GOS) values lower than 2° are recognised as recrystallized grains [137,138].

In Figure 44 a), the plots show the average grain size and recrystallized grain size evolution at each corner. The average grain diameter reduced rapidly from over 100 μm to around 60 μm after 5 min of annealing and remained at ~60 μm with further annealing. The recrystallized grain diameter grew quickly from 0 μm to around 60 μm after 5 min of annealing and remained at ~60 μm.
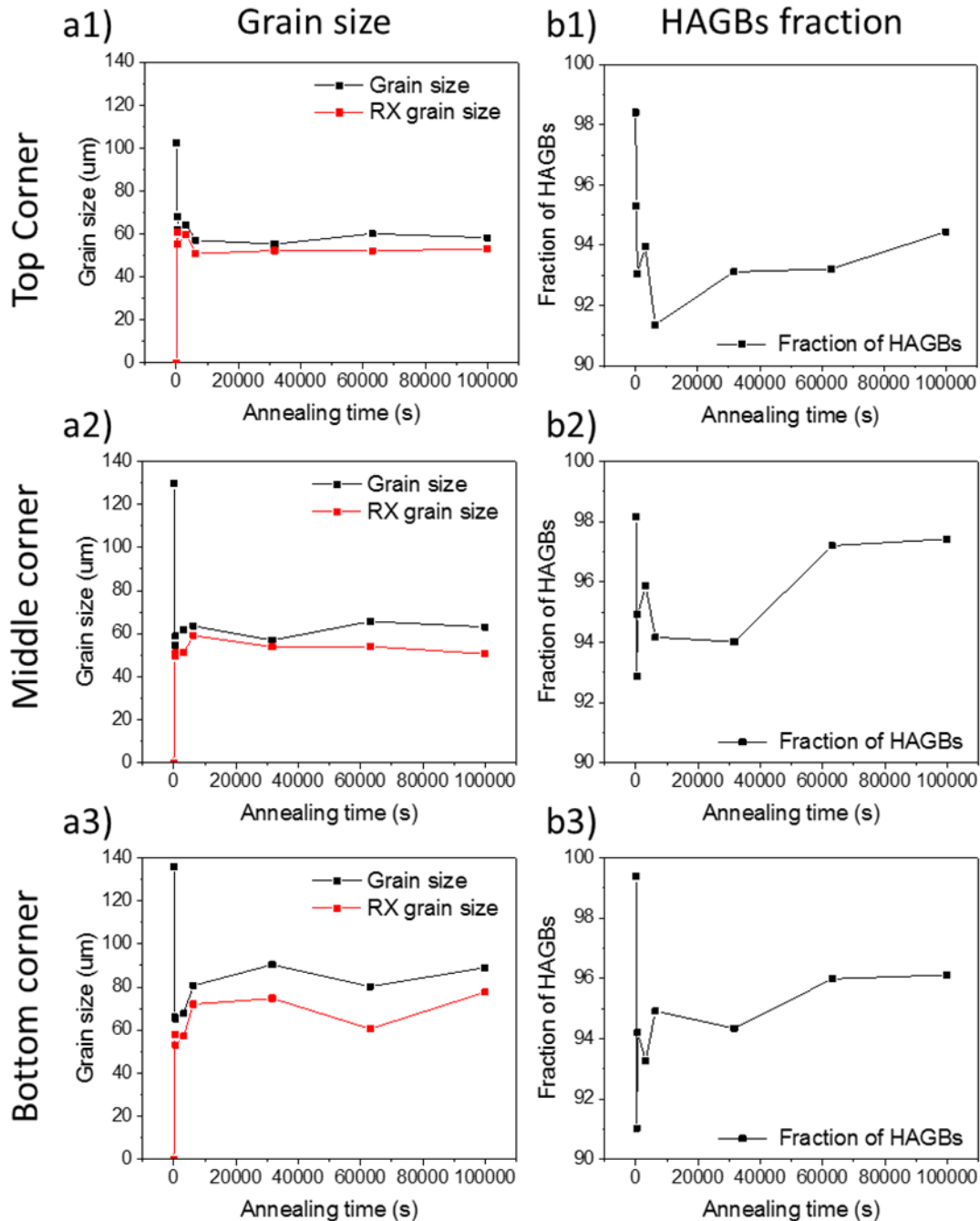
Figure 44 *a) Average grain diameter and recrystallized grain diameter evolution on top, middle and bottom corners after 0, 5, 10, 52, 105, 527, 1051 and 1667 min annealing at 500℃. b) The evolution of high angle grain boundaries (HAGBs) fraction during annealing.*

The quasi-in-situ EBSD maps were zoomed in to investigate how the microstructure changed during annealing to determine the nucleation mechanism in pure aluminium. An example is shown in Figure 45. Subgrains were found within the recrystallized grain, such as the Grain A in Figure 45 b), with an orientation variation inside it. The subgrain boundaries transformed into the HAGBs and formed separate grains during further annealing (see Figure 45 c)). Thus, the evolution of the average grain size fluctuated with the annealing time due to the separation of growing grains. The plots of HAGBs fraction in Figure 44 b) show that the fraction of HAGBs increases with annealing. These results validate the nucleation theory as seen in Figure 2 a) and b), and explain why the average grain size does not grow during annealing.
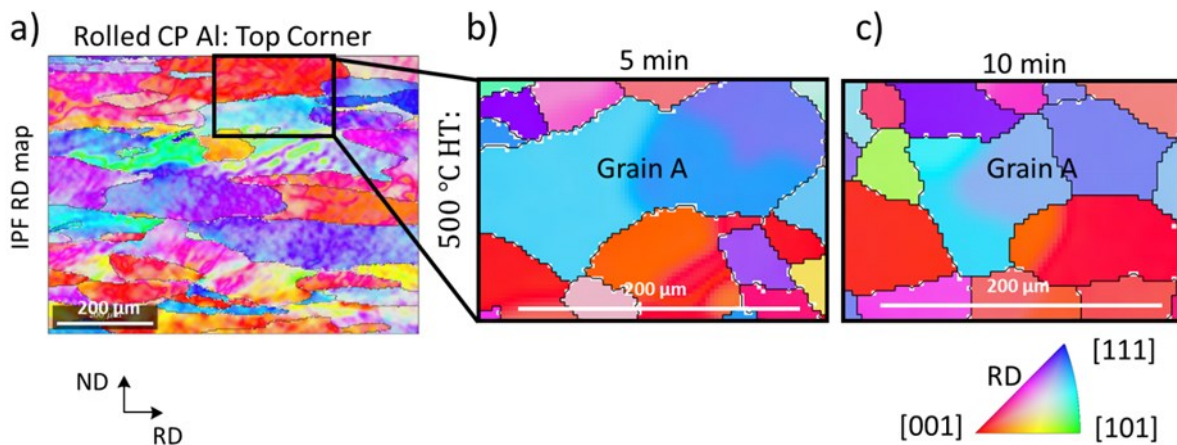
Figure 45 EBSD IPF maps of a small area on the top corner of cold-rolled pure aluminium 1050A after a)-c) 0, 5 and 10 min annealing at 500℃. b) and c) show how the subgrain boundaries in recrystallized grain A were accumulated during annealing to form separated grains.

5.4.1.3 Hardness evolution

The hardness evolution shown in Figure 46 was obtained by performing the Vickers hardness tests using a load of 5 kg on the sample annealed for different times at 500 ℃. The hardness of the pure aluminium depends on dislocations and grain size only, due to the absence of any alloying precipitates. The hardness of cold-rolled pure aluminium dropped rapidly from HV5 38 to 20 after 5 min of annealing due to the elimination of dislocations by RX. The hardness of the annealed samples remained constant at around HV5 20 during annealing, while the hardening is mainly caused by grain boundaries after full RX as described by the Hall-Petch relation [139]. This macroscopic mechanical behaviour of annealed pure aluminium also

demonstrates that grain size does not vary greatly in the annealed sample since the effects of grain boundary hardening are similar for the sample at the different annealing times.
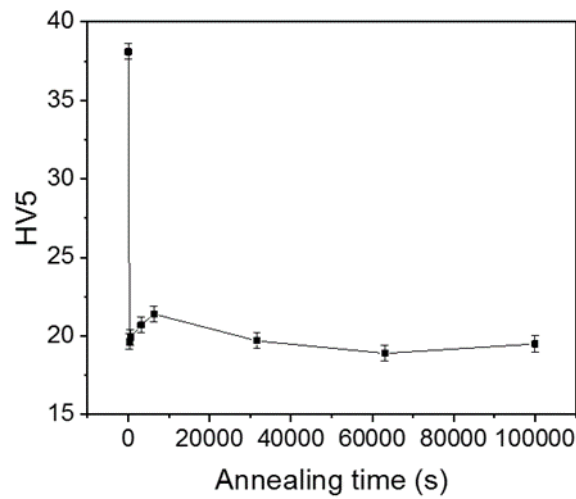
Figure 46 *Macroscopic hardness results on the cold rolled pure Al that annealed for 0, 5, 10, 52, 105, 527, 1051 and 1667 min at 500°C.*

5.4.1.4 GND density and RX fraction evolution

The geometrically necessary dislocation (GND) distribution was calculated using the method in [116] and plotted in Figure 47 b). The displacement gradient tensor was obtained first from the orientation map. The lattice rotation corresponding to the antisymmetric part of the displacement tensor was thus resolved. The lower bound of the GND density was then estimated from the lattice rotation gradients [116,117]. Subgrain boundaries observed in the GND maps are the positions with high values of GND inside of the grain.

The evolution of the RX fraction during annealing, shown in Figure 47 a), was quantitatively analysed based on the kernel average misorientation (KAM) as calculated from the EBSD maps. The KAM is an average misorientation of a point with respect to all its neighbours, i.e. a measure of local deviation in orientation. The areas with KAM values less than the threshold value (0.5° in this work), were recognised as new deformation-free, recrystallized areas [140].

As shown in Figure 47 a) and b), the RX completed in 5 min, resulting in a quick reduction of GND from $\sim 100 \ \mu m^{-2}$ to $\sim 10 \ \mu m^{-2}$ in 5 min. The slight fluctuation of RX fraction and GND density during further annealing was due to the area change of grain boundaries. The evolution of RX fraction at the top corner was plotted in Figure 51 a) together with the JMAK theoretical curve and the curve from the phase-field model.
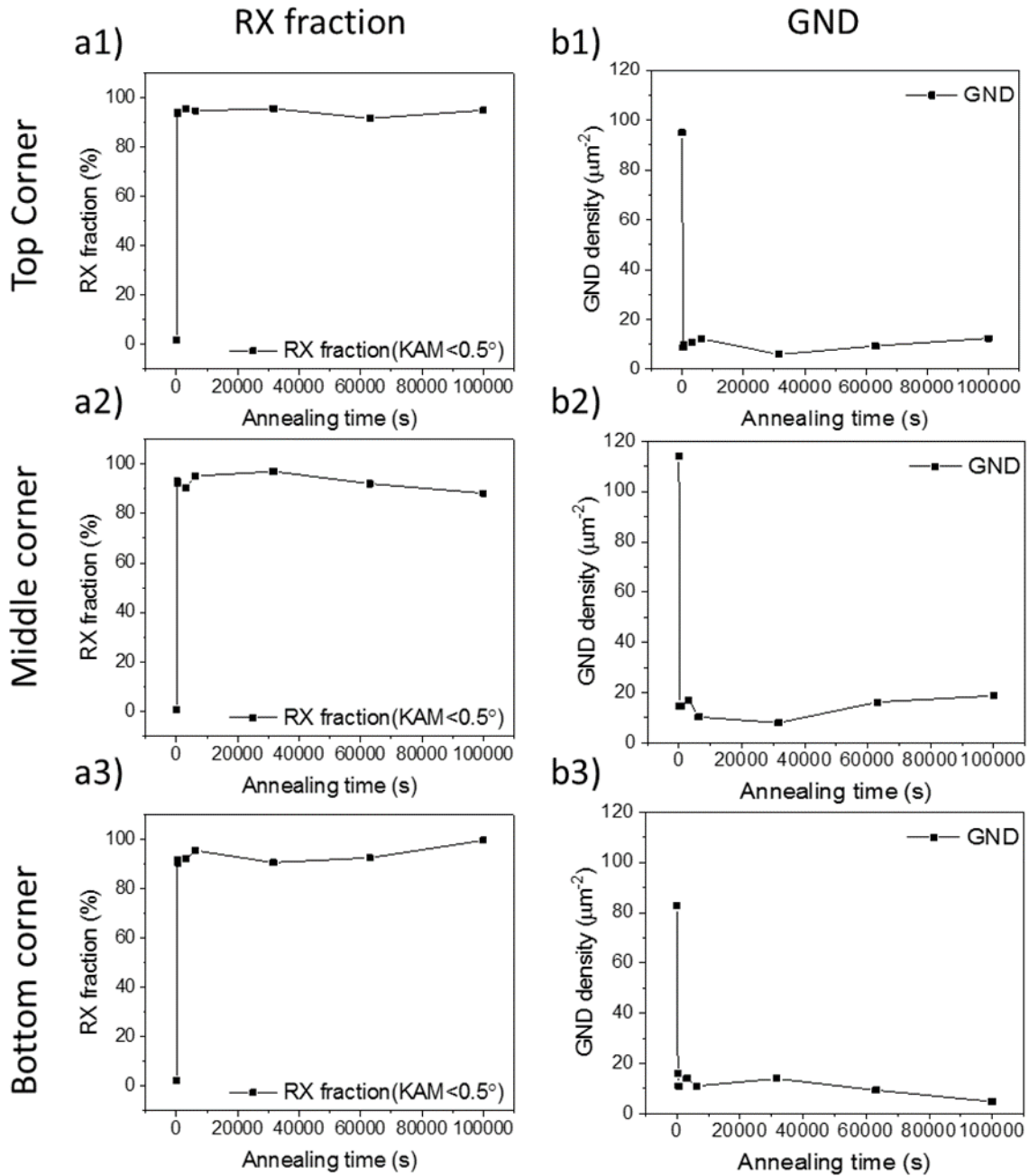
Figure 47 a) *Recrystallization fraction values calculated based on the KAM maps on top, middle and bottom corners after 0, 5, 10, 52, 105, 527, 1051 and 1667 min annealing at 500 ℃.* b) *The evolution of geometrically necessary dislocation density (GND) during annealing.*

5.4.2 CPFE results

The xy face of the CPFE model, with the boundary conditions of plane strain compression, was plotted in Figure 41. The colour represents the dislocation density distribution, which is the

sum of GND and SSD densities. The nucleation positions of the new grains during annealing were determined based on this dislocation distribution (shown in Figure 42).

5.4.2.1 Simulated texture evolution

The orientations of the nucleated grains were assigned based on the rolled sample since the DBs (see Figure 48 a) for the rolled sample) have been demonstrated in Chapter 4 as a source of orientations for nuclei. According to the experimental observation on the texture evolution shown in Section 5.4.1.1, the recrystallized texture remained close to that of the deformed texture at the mesoscale. Hence, the simulated deformation and recrystallized texture in this work were assigned to have the same texture as in the experiments. The consistency of the texture in modelling and experiment was verified by comparing their IPF maps and PF (see Figure 48).
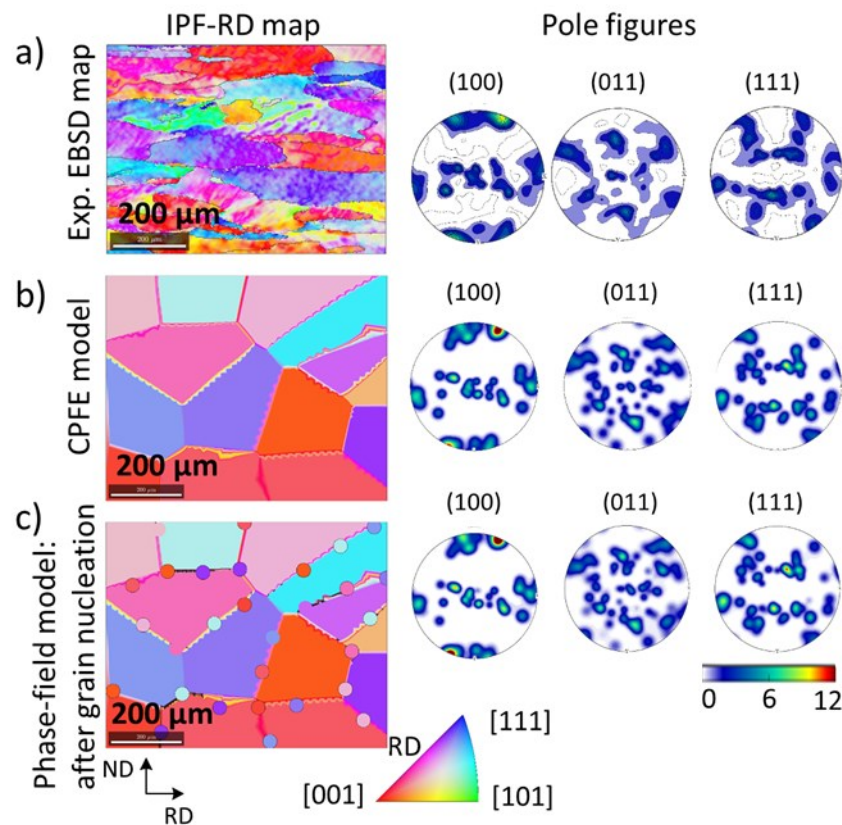
Figure 48 *a)-c) are the IPF-RD maps and PF of the grain orientations in EBSD map, in deformed CPFE model and in the phase-field model after the simulation of grain nucleation.*

5.4.2.2 Simulated RX fraction evolution

Figure 49 shows the simulated evolution during annealing at 500 °C of a) the recrystallized phase and b) grain orientations. The recrystallized phase with low energy during annealing is

shown to bulge into the neighbouring deformed phase with high stored energy and thus reduce total stored energy. The grain growth described by Equation (12) and (13) was quantitatively analysed by measuring the grain size and RX fraction at each time step and plotted in Figure 51 together with the JMAK and experimental results. As the grain nucleation in this chapter occurred at the beginning of the RX, the time for nucleated grains to reach the critical diameter of 40 μm at 500 ℃ was estimated to be 40 s according to the initial area fraction of the recrystallized phase, which is 0.157, in the phase-field model. The critical grain diameter was set to be 40 μm according to the size of small grains shown in the recrystallized EBSD maps (see column a) and c) in Figure 50).
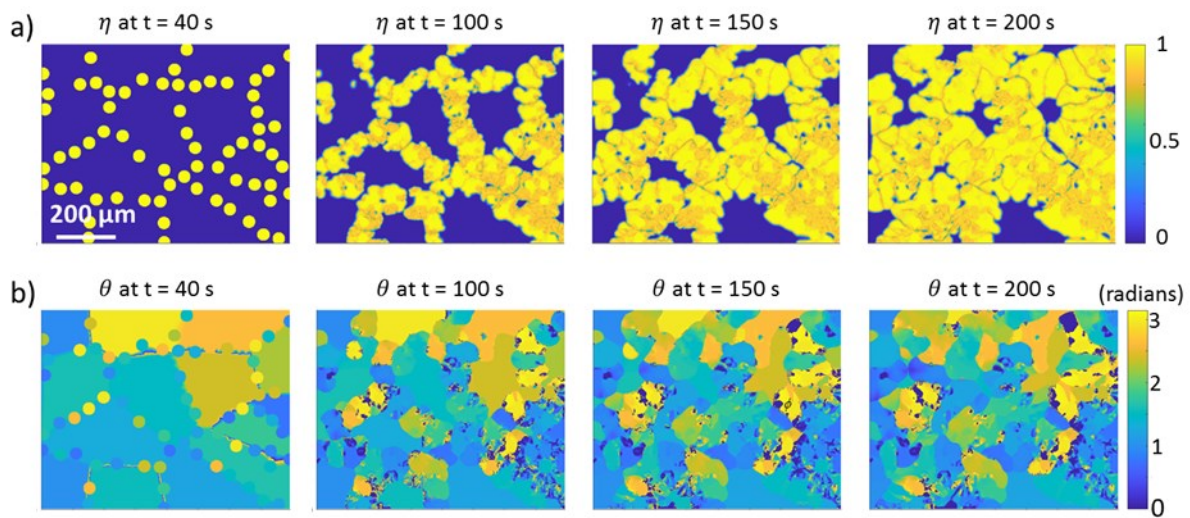
Figure 49 *a) and b) show the change of two order parameters η and θafter 40s, 100s, 150s and 200s annealing at 500 ℃ obtained by the KWC phase-field model.*

5.4.2.3   Simulated grain size evolution

The orientation evolution simulated by the KWC phase-field model was processed using the grain construction in MTEX toolbox [130] to obtain the grain structure (see Figure 50). Column a) and b) in Figure 50 show the grain structure from the top corner EBSD maps and phase-field simulations after 0, 5, 10, 52 and 105 min of annealing at 500 ℃. The grain area distributions for experimental results and simulated results are shown in column c) and d) correspondingly.

A comparison between column c) and d) in Figure 50 reveals that the phase-field model predicts the grain area distribution accurately after the completion of RX, i.e. after 5 min. The simulated grains after full RX generally had an area size of less than 1.5×10^{4} μm^{2}, with only a few of them having an area larger than this. Furthermore, in terms of the average grain size,

the simulated evolution agreed well with the experimental results as shown in Figure 51 b), especially when the annealing time is longer than 10 min.
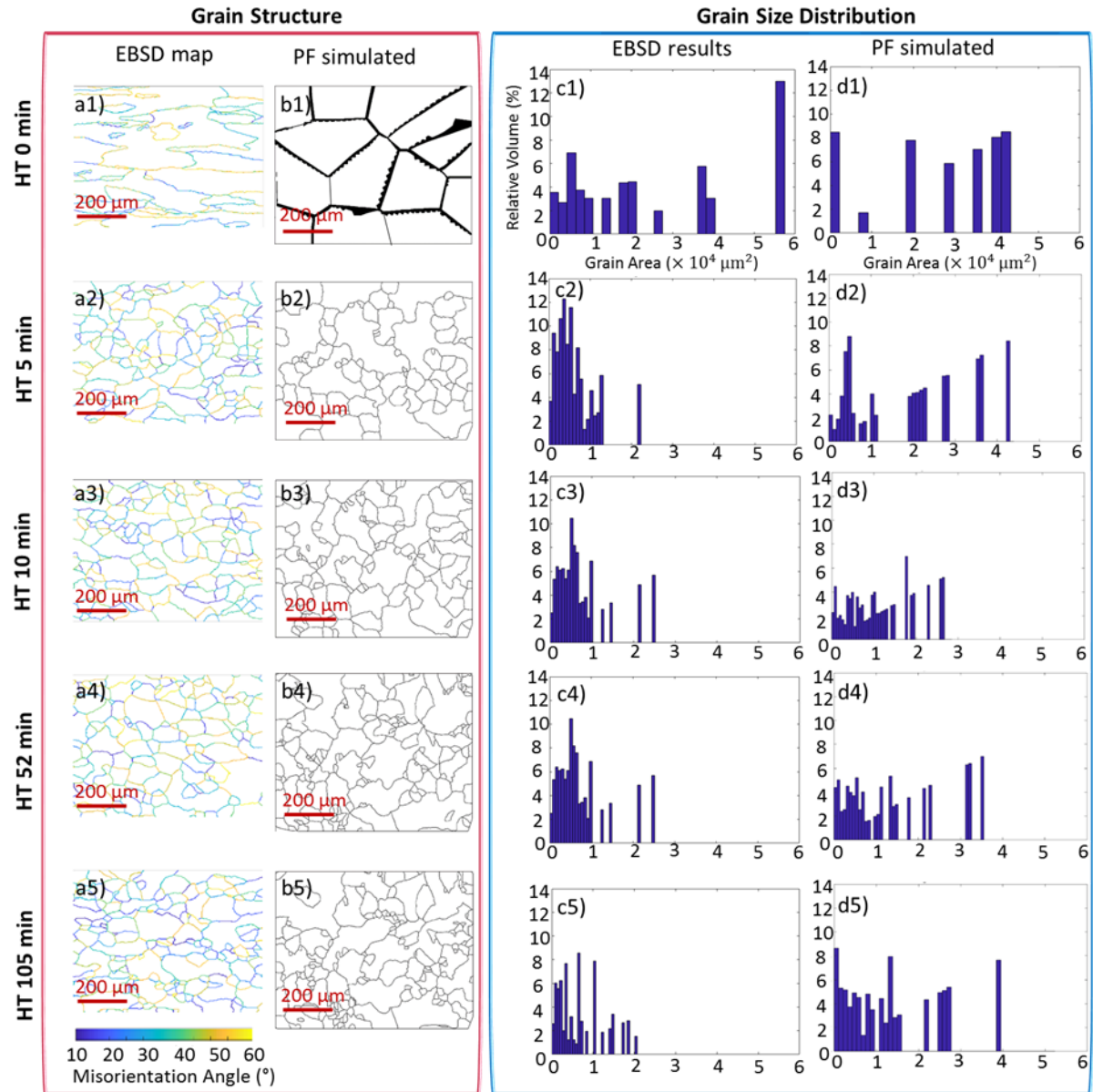
***Figure 50** Column a)-b) and c)-d) are the grain structures and histograms of grain area from EBSD mapping and phase-field modelling respectively, after 0, 5, 10, 52 and 10 min annealing at 500℃. The grain boundaries shown in a1)-a5) are coloured to show their misorientation angle.*

5.4.3 JMAK curve

Based on the previous discussion, the Avrami exponent $n = 2$ was selected for the JMAK curve of rolled pure aluminium alloy, which was heated at 500 ℃. The Avrami coefficient k=5.625$\times 10^{-5}$ was chosen by calibrating the JMAK equation with the experimental EBSD

results. As the maximum RX fraction is 0.95 due to the existence of high angle grain boundaries (see Figure 50), the JMAK curve has been modified to the equation below and plotted in Figure 51 a):

$$X = 0.95 \times [1 - \exp(-5.625 \times 10^{-5} \times t^2)] \tag{31}$$

5.5 Discussion

5.5.1 Experimental observations

Through tracking the microstructural evolution during SRX using quasi-in-situ EBSD maps, the mechanisms of grain nucleation and grain growth in the rolled pure aluminium were revealed. Furthermore, the validation of the phase-field model was achieved by the evolution of microstructural features characterised by EBSD.

In terms of the grain nucleation, subgrain boundaries absorbed dislocations during annealing, resulting in an increase of misorientation, stored energy and mobility, thus, leading to the transformation into HAGBs and the formation of grains [2]. This explains why the fraction of HAGBs increased with annealing and why the recrystallized grains grew to $\sim 60 \ \mu m$ diameter in the first 5min and then kept constant during annealing (see Figure 44). The simultaneous processes of grain splitting and grain growth accounted for the dynamic stability of grain size during annealing. In terms of grain coarsening, pre-existing HAGBs migrated toward the interior of a more highly strained grain to minimise the total energy of the system, as described by the SIBM theory [9,94].

In addition, the grain nucleated by subgrain boundary migration maintained the orientation of the subgrain while its orientation was originally generated from the deformed structure. Thus, it is straightforward to account for the consistency between the recrystallized texture and the deformed texture in Figure 43 c). Therefore, the nucleation mechanism of pure aluminium can be described by the migration of pre-existing subgrains or grain boundaries [9].

5.5.2 Modelling results

5.5.2.1 Prediction of texture and nucleation positions

The heterogeneous distribution of dislocation density and the accumulation of dislocations at grain boundaries in the textured model under plane strain compression were captured by the CPFE model in this chapter. This dislocation distribution and grain orientation information

were then used as initial conditions for the phase-field model, making the prediction of nucleated grain orientations and nucleation positions in the deformed structure possible. The model described in this work can be adapted to study other materials by incorporating the effects of precipitates, material properties etc.

5.5.2.2 Prediction of incubation time

The phase-field model coupled with theoretical JMAK kinetics provides insights into the nucleation mechanism regarding the estimation of incubation time and its relation to dislocation density and annealing temperature, which are hard to be captured by experiments. In this chapter, the incubation time was determined as ~ 40 s to reach the RX fraction of 15.7 % with the critical recrystallized grain diameter of 40 μm (see Figure 51 a)).

5.5.2.3 Prediction of RX fraction evolution

The simulated evolution curve agrees well with the EBSD results and JMAK curve in Figure 51 a), indicating that the phenomena of the grain nucleation and the impingement of growing grains for moderate grain growth were successfully simulated. The KWC phase-field modelling in this chapter considers the energy from dislocations, the interface energy and the misorientation energy.

5.5.2.4 Prediction of grain size evolution and distribution

The phase-field model together with the CPFE model was able to provide a reliable prediction of the grain size distribution and evolution for pure aluminium after full RX (see Figure 50 b) and Figure 51 b)). The slight variation of grain size distribution between experiments and simulation in initial observation (see Figure 50 c2) and d2)) is likely due to the choice of nucleation condition for critical stored energy. The in-situ EBSD mapping for the SRX of rolled pure aluminium could help to determine this value by observing the minimum grain size and calculating the GND density at the nucleation position before and after the nucleation. As a result, the grain size at partial RX could then be accurately predicted.
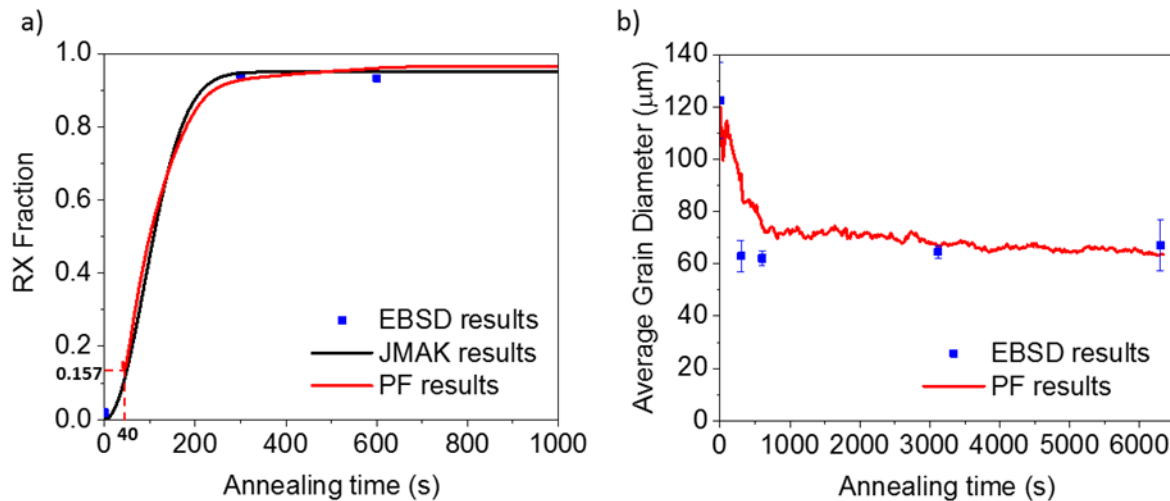
Figure 51 *The evolutions of a) recrystallization fraction and b) average grain diameter at 500°C heat treatment from experimental EBSD results, phase-field (PF) modelling and theoretical JMAK curve.*

5.6 Summary

In the meanwhile of demonstrating the effect of dislocation structure on the RX in polycrystalline aluminium alloy, this chapter also developed a modelling methodology to link dislocation structure with RX process.

Based on quasi-in-situ EBSD results, the nucleation mechanism of AA1050 is attributed to the migration of subgrain boundaries and SIBM. This leads to a) splitting of the grain during grain coarsening due to the transformation of subgrain boundaries into HAGBs; and b) maintenance of the deformed texture during annealing.

The validated CPFE and KWC phase-field model provides a versatile tool for simulating the microstructural evolution during RX. The simulated evolution is quantitatively in a good agreement with the quasi-in-situ EBSD results regarding grain morphology and texture development. Also, the validated model predict the incubation time with reasonable accuracy.

6 Interaction of DBs and RX in AA7050

6.1 Introduction

The 7xxx series aluminium alloys are widely used in aeronautical and automobile industry for its excellent strength-density ratio, among which the aluminium alloy 7050 (AA7050), a typical Al-Zn-Mg-Cu aluminium alloys, is particularly preferred for aeronautic components such as upper wing skins, stringers and stabilizers [141] on account of its desirable physical and mechanical properties [142].

The performance of large piece AA7050 components formed by hot forging, such as the lifetime and the mechanical properties, are strongly affected by the complex microstructural evolution under severe plastic deformation. Hence, the control of microstructure typically by RX process during the industrial manufacturing process is crucial for the final structural component to acquire desired properties [143] after forging. Furthermore, the RX as a softening mechanism is able to help the material reducing the flow stress during forging through wiping out the dislocations at elevated temperatures. The forgeability of AA7050, thus, is improved which would eventually help the industry to cut down the manufacturing cost [144,145].

Nevertheless, the prediction of basic microstructural characteristics, such as the grain size evolution, during thermomechanical processing (TMP) is still a problem for the manufacturing of high strength AA7050. It is caused by the failure of linking the deformation process with the RX process. In previous Chapter 3, 4 and 5, the prediction on the deformed microstructure, the occurrence of RX and the kinetics of RX has been achieved for pure aluminium of single and mutlicrystal. It has been found that DBs are crucial for the prediction of RX process in pure Al implying that the effect of DBs needs to be considered in RX models.

During the manufacture of forged components, commercial Al alloys are normally preheated before forging to temperatures in the range of 400°−500°C [146] to reduce the flow stress during deformation [147]. The preheating process would cause a partial or complete dissolution of precipitates in the forging metal [146]. Therefore, the effect of solutes on the deformation

state and the subsequent dynamic or static RX is also crucial for the control of eventual microstructure in the metal component and its performance in service.

Previous chapters have demonstrated that, without the existence of solutes, DBs generated during plastic deformation is a dominant factor for the RX process in solute free Al. As a result, this chapter is going to check whether the formation of DBs is affected by the existence of solutes and whether DBs is still a major cause for the RX in commercial Al alloys.

To avoid the effect of precipitate on the formation of deformed microstructure, this chapter uses solution heat-treated AA7050 to validate the formation of DBs in the precipitate free commercial Al alloys and its effect on RX at the existence of a large amount of solutes. The solution heat-treated AA7050 were compressed to 0.3 engineering strain and then annealed at 450 ℃ for different times to capture the RX process by EBSD technique. Knowledge obtained from pure aluminium is validated for the commercial AA 7050.

6.2 Methodology

6.2.1 Materials preparation

The work in this chapter used commercial AA7050 rolled thick plate with the initial temper of T7451 [142] from the Aviation Industry Corporation of China (AVIC) the First Aircraft Institute (FAI) to study the formation of DBs and RX in commercial Al alloy. To achieve the temper of T7451, the metal is solution heat-treated, stress relieved by stretching, then stabilized by artificial overaging. The main chemical composition of AA7050 is Al-6.2Zn-2.3Mg-2.3Cu-0.12Zr [142]. Cylindrical specimens with 8 mm in diameter and 12 mm in height were machined from the plate. The specimens were solution heat-treated at 500 ℃ for 24 hours in the furnace and followed by cold water quenching for uniaxial compression test.

The specimens were sectioned along the loading direction, mounted in bakelite resin, ground by SiC papers (up to 1200 grit) and polished with ~50 nm OP-S (Oxide Polishing Suspensions) diluted with H_2O by a ratio 1:5 of OP-S:H_2O. For optical microscope (OM) mapping, the metallographically polished samples were then etched for 25 s using Keller's agent with the composition of 1.5% HCl + 1% HF + 2.5% HNO_3 + 95% distilled water [142]. For EBSD mapping, the metallographically polished faces were electropolished for 60 s in a solution of 9.5 vol% perchloric acid in ethanol at room temperature and 20 V. The parameters used for characterisation keeps the same with the experiments in Chapter 3 and 4.

6.2.2 Compression tests and heat treatments

The uniaxial compression tests for the solution heat-treated AA7050 were carried by Instron mechanical testing frame to achieve up to 0.3 engineering strain at a 0.002 s^{-1} strain rate and room temperature. The experimental stress-strain behaviour can be found in Figure 52. Samples were lubricated on both sides to reduce the friction during the compression.

The interrupted heat treatments for the deformed samples were carried at 450 ℃ for different times, i.e. 0, 3.5, 10 and 35 min, in the furnace and followed by cold water quenching. The samples after each heat treatment were prepared for EBSD analysis.
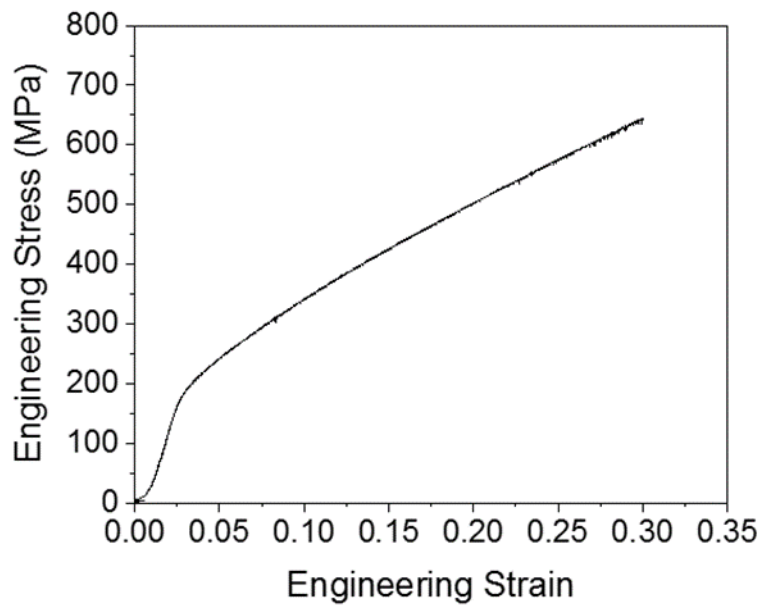
Figure 52 *The exp. stress-strain curve of solution heat-treated AA7050.*

6.3 Results and discussion

6.3.1 DBs in AA7050

The OM maps and EBSD IPF maps of deformed AA7050 viewed down the compression axis (i.e. Y-axis) are plotted in Figure 53 (a)-(f). The misorientation angle along the line which crosses the bands are plotted in Figure 53 (g)-(h) showing the existence of DBs in deformed AA7050 since sharp orientation changes (i.e. misorientation >15˚) were observed at each edge of bands (i.e. boundary of DBs). It is clearly shown in Figure 53 that DBs which can accommodate the imposed plastic deformation are widely developed in polycrystalline AA7050.

The kernel average misorientation (KAM) maps in Figure 54 to show the position of DBs and the change of stored dislocations are calculated based on the orientation deviation to its neighbouring points. The algorithm for KAM calculation is shown in Appendix A Section A.1.4.
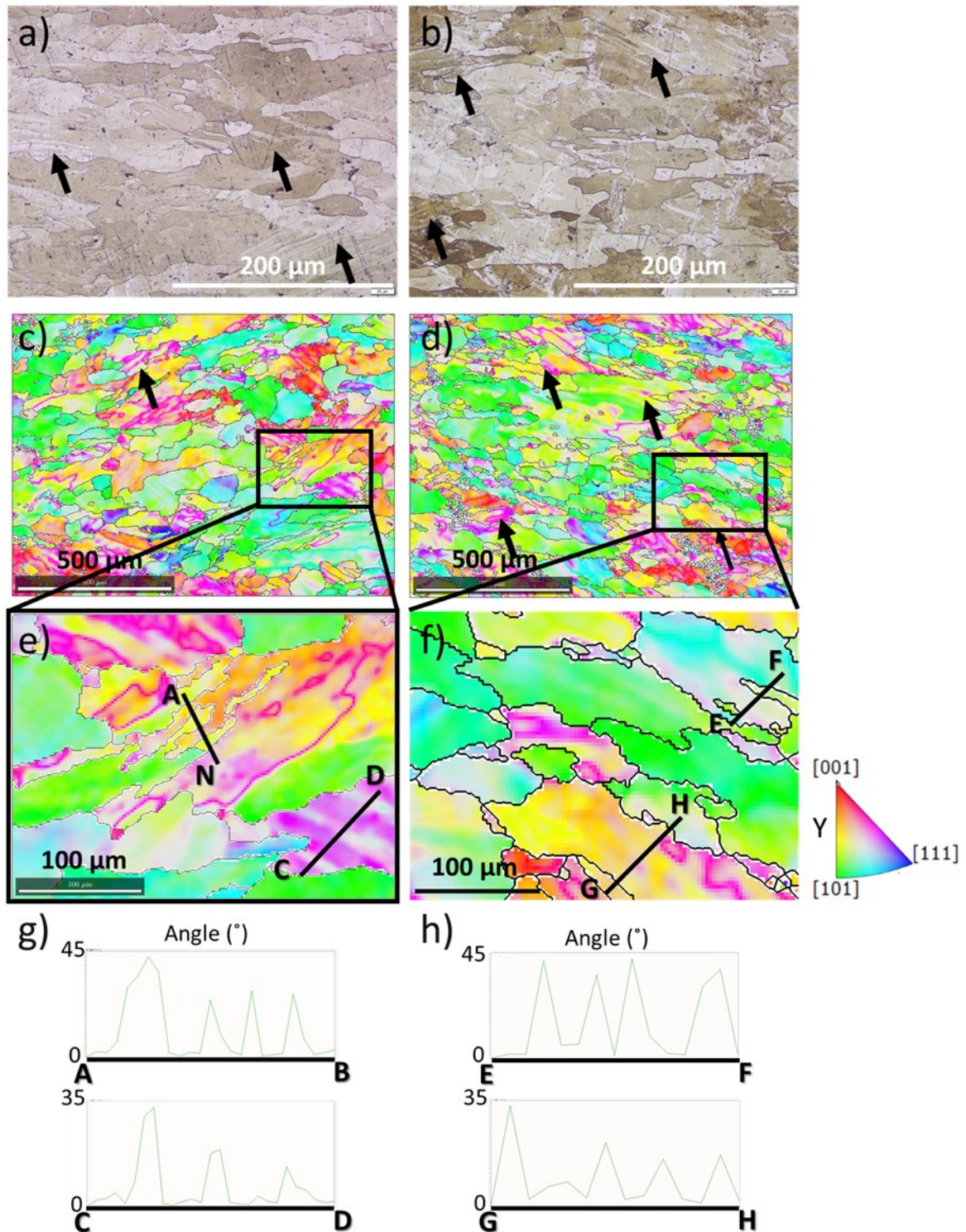
Figure 53 *Microstructural characterisation of deformed 7050 Al: left and right column maps are captured from two specimens respectively by OM mapping (a)-(b) and EBSD mapping (c)-(f) (IPF-Y colouring, i.e. the loading direction). DBs are labelled out by arrows in the map (a)-(b). The distributions of misorientation angle to the previous point along the line AB, CD, EF and GH which crosses the DBs are plotted in (g)-(f) for two specimens.*

According to the KAM maps and the Schmid factor (SF) maps of the deformed microstructure shown in Figure 54 (a), more DBs are found in the grains with higher SF. It is reasonable to conclude that developing DBs in polycrystalline AA7050 is easier in 'soft' grains compared with the 'hard' grains. Furthermore, the SF of the orientation in DBs is found to be lower (i.e. the darker colour in SF map, see Figure 54 (a3)) than its parent grain which means the orientation in DBs becomes 'harder' during the plastic deformation. These findings for AA7050 regarding the formation of DBs and its orientations keep consistent with the formation of DBs in pure Al in Chapter 3.
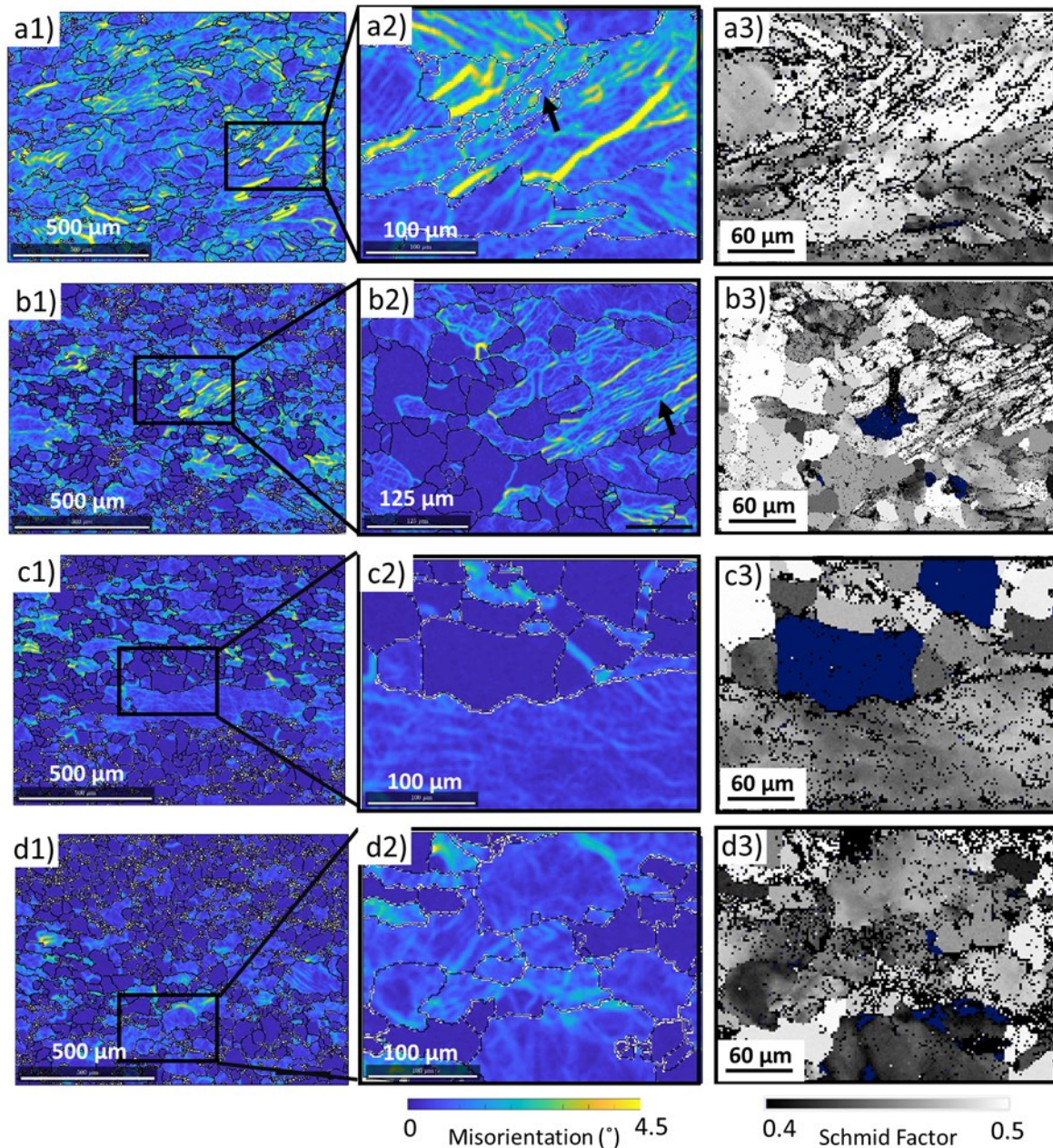
Figure 54 *(a1)-(d1) are the kernel average misorientation (KAM) maps of deformed AA7050 after 0, 3.5, 10 and 35 min annealing at 450 ℃, showing the change of stored energy in AA7050 during RX. (a2)-(d2) and (a3)-(d3) are the KAM maps and Schmid factor maps of the zoomed-in area in (a1)-(d1). DBs are labelled out by arrows in the map (a2) and (b2).*

6.3.2 Effect of DBs on RX in AA7050

To reveal the microstructural evolution of deformed AA7050 at 450 ℃ during RX, the EBSD IPF-Y maps, their corresponding KAM maps and Schmid factor maps are plotted in Figure 54 and Figure 55.

The deformed matrix mainly recovered within 3.5 min annealing without the development of dislocation free new grains. Initial grain nucleation is observed after 10 min annealing nearby DBs (see Figure 55 (b)), showing some small grains with low KAM. Obvious grain growth is found after 35 min annealing in Figure 55 (c).
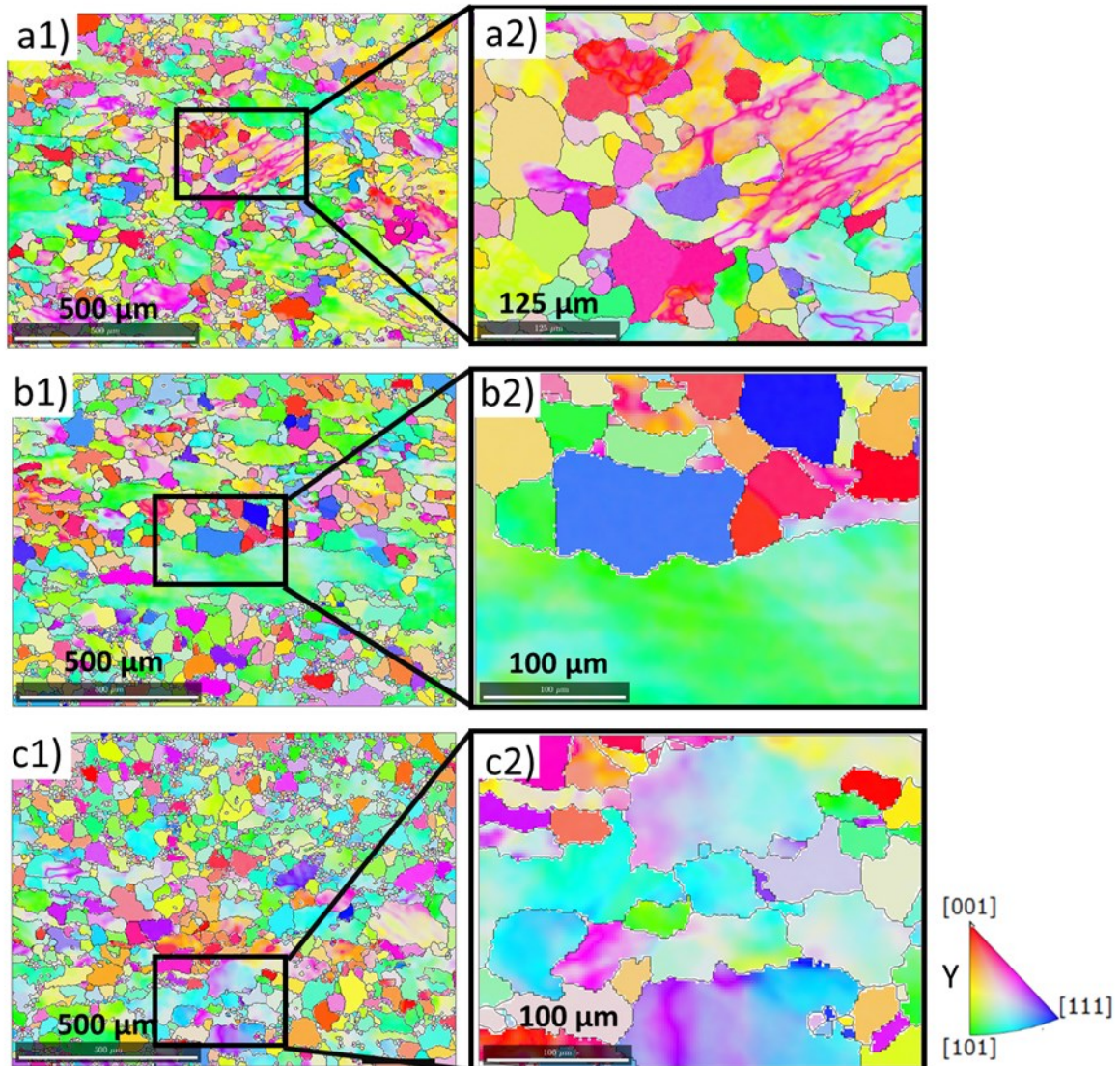
Figure 55 *(a1)-(c1) are the EBSD IPF maps along the Y-axis and (a2)-(c2) are its zoomed-in areas of AA7050 which were annealed for 3.5 min, 10 min and 35 min respectively, showing the RX process of deformed AA7050.*

6.3.2.1 Nucleation sites

The microstructural evolution of deformed AA7050 during the recovery and RX process is shown in Figure 54 (b)-(d) and Figure 55 (a)-(c). Regarding the grain nucleation sites in the deformed microstructure of AA7050, the regions with more DBs are found to recrystallize preferentially compared with the regions without distinct DBs. For example, numerous

recrystallized grains are found nearby DBs in AA7050 after 10 min annealing while only the recovery is found in the area without DBs (see Figure 54 (c) and Figure 55 (b)).

6.3.2.2 Recrystallized orientations

The quantitative analyses of the KAM and SF maps are plotted in Figure 56 to show the change of misorientation angle distribution and Schmid factor distribution during annealing. The change of misorientation angle distribution in Figure 56 (a) shows the reduction of stored energy during recovery from 0 to 3.5 min annealing, grain nucleation from 3.5 to 10 min annealing and grain growth from 10 to 35 min annealing.
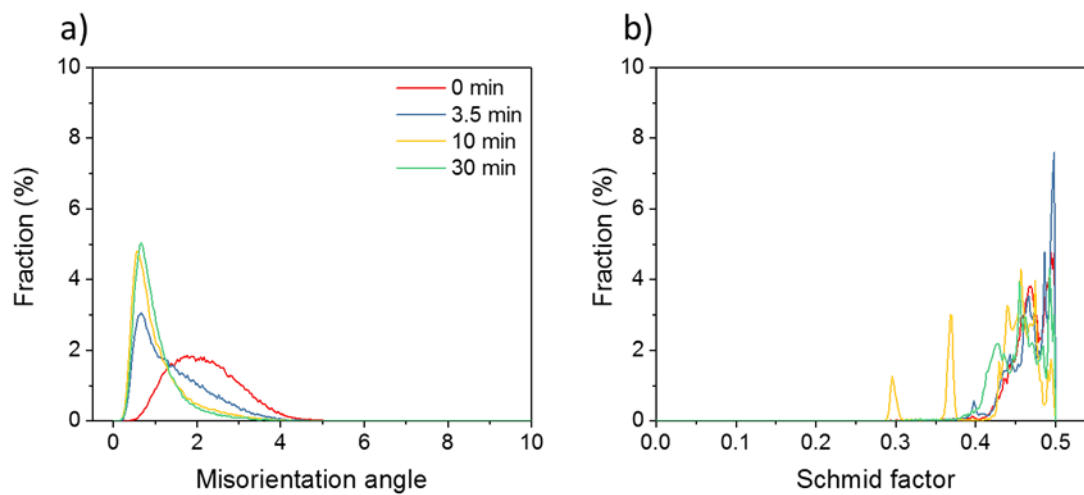
Figure 56 *The histogram of (a) the kernel average misorientation (KAM) maps to show the change of misorientation angle distribution; (b) the Schmid factor in deformed 7050A after 0, 3.5, 10 and 35 min annealing at 450 ℃.*

The change of Schmid factor distribution in Figure 56 (b) show that the texture tends to become 'harder' during RX, i.e. the overall value of SF decreases during annealing (also seen in Figure 54 (a3)-(d3)). The orientations of the RXed grains are likely to be the main reason for this texture evolution. It can be found in the SF map for AA7050 after 3.5 min heat treatment (see Figure 54 (c3)) that the RXed grains have fairly small values of SF causing the subpeaks in Figure 56 (b).

In Chapter 4, the orientation of DBs in pure aluminium is found to be a major source of orientations for recrystallized grains, while the orientation of DBs is noticed to become 'harder' after plastic deformation. Hence, it is reasonable to conclude that RXed grains induced by DBs

would result in a 'harder' texture after RX. In this section, it can be seen that all the above findings for pure aluminium are found in the commercial AA7050.

6.3.3 Impact of studying DBs on the forging process

As discussed in Section 6.1, the forging process, which induces severe plastic deformation and complex microstructural evolution, is necessary for the final aluminium components to acquire desired properties [143]. To provide industrial solutions for the design and optimization of forging processes, finite element (FE) simulation is an important tool on the prediction of the microstructure evolution and the selection of forming parameters for the large-scale structural aluminium component [148,149].

However, the internal state variables, such as grain size, dislocation density, grain boundaries, etc., in current FE models are mainly based on the empirical methods or experimental observations which cannot precisely describe the heterogeneities in the deformed alloy. It makes the generalization of the FE models to the other processing routes challenging since the deformed microstructure is highly affected by strain paths [148]. By contrast, although the microstructural based models can calculate the evolution of microstructure in mesoscale, it is hard to apply them to the simulations of a full process of hot deformation on a large scale due to the huge computational cost [4]. The generalization of the microstructural models to different heat treatments and processing routes is also problematic [6,75].

For instance, Li et al. [150] recently developed physically-based constitutive equations for a FE model to predict the RX process in hot forging of AA7050 components based on the rotation of subgrain boundary (i.e. LAGBs) to high angle GBs (i.e. HAGBs) and the migration of LAGBs and HAGBs. It is an EBSD experimentally validated model for the internal states variables and a big step forward from the existing stress-strain curve fitting process. However, the effects of dislocation density, such as strain path effect and DBs formation on RX which bring the heterogeneities into the deformed microstructure have yet taken into account due to the lack of understanding and time-consuming experiments. As a result, the developed CPFE and PF model would provide as a valuable tool linking the microstructure evolution and macro processing for future physically-based model development, which would save considerable time with improved accuracy on the design of processing routes.

Therefore, an accurate prediction of the dislocation structure and its relation to RX is crucial to the FE models. The work in this chapter has demonstrated that the existence of DBs has an impact on the nucleation sites and the nucleated orientations in commercial Al alloys. It has been found that numerous DBs in the deformed AA7040 samples incubates RXed grains during the subsequent heat treatment. The findings on the formation of DBs (i.e. dislocation structure), as well as its effect on the RX process, can be adopted into FE models to solve its generalization problem when dealing with the complex forging routes.

6.4 Summary

In this chapter, EBSD analysis of AA7050 is applied to verify that the findings for pure aluminium discussed in Chapter 3 and 4 are valid for commercial polycrystalline alloys. Firstly, numerous DBs were also observed in commercial aluminium alloys at the existence of substantial solutes. The formation of DBs in AA7050 is demonstrated to follow the mechanism shown in Chapter 3 for pure Al, i.e. DBs prefer to form in 'soft' grains with a 'harder' orientation. Secondly, DBs developed in deformed AA7050 are also found to be a source of nucleation sites and orientations for recrystallized grains.

It has been demonstrated in this chapter that the forging process for the manufacture of structural components, such as the AA7050 for the high-stressed aeronautic components, would create numerous DBs in the deformed structure which govern the possible dynamic RX during forging and the inevitable static RX process during the subsequent solution heat treatment for the forged metal. Therefore, the mechanism of DBs formation developed in this work would help with the prediction of dislocation structure in deformed metal which makes the design of forging routes, i.e. strain path, for a fine microstructure possible.

7 Conclusions

7.1 Thesis review

In this thesis, a systematic study of the RX process in aluminium alloys was performed, to understand the fundamental mechanism of DBs formation, and develop theories for the effect of DBs on RX with the ultimate motivation of improving the prediction of the RX process.

Chapter 1 introduced the basic background and the motivations for both scientific understanding and manufacturing industry. Chapter 2 provided knowledge of deformed microstructure, RX process and RX models, also summarised unsolved problems of RX process for the use of later chapters.

The main novel contributions of this study were conducted in four subsequent parts in a logical sequence: (a) developing the mechanism of DBs formation in Chapter 3, (b) quantitatively analysing the effect of DBs on RX in Chapter 4, (c) combining microstructural characterization with crystal plasticity and phase-field modelling in Chapter 5, and (d) validating the formation of DBs and its effect on RX in commercial Al alloys in Chapter 6.

In Chapter 3, the slip band intersection from primary and secondary slip was found to be the main cause for the formation of DBs in single crystal and multi-crystal pure Al. The value of the primary slip field was demonstrated to have a strong positive correlation with the amount of DBs. Also, the orientation formed in the DBs was found to become 'harder' compared with the initial orientation.

In Chapter 4, the mechanism of RX process at the existence of DBs was summarised for pure aluminium. DBs were found to be a major source of nucleation positions and nucleated orientations. Areas with higher area fraction of DBs were found to have a higher rate of the RX process since DBs would provide more potential nucleated sites and less incubation time for RX.

In Chapter 5, excellent agreements between predicted microstructures and experimental observations were achieved in polycrystalline pure Al, especially for the grain morphology evolution and texture evolution. The incubation time of grain nucleation was also quantified through calculating the critical energy, critical grain size and favourable orientations of the nucleated new grains.

In Chapter 6, knowledge obtained for pure aluminium from previous chapters was validated for the commercial aluminium alloys AA 7050. The impact of DBs at the existence of substantial solutes during forging was verified since the numerous DBs were observed in deformed AA7050 which incubated RXed grains during the subsequent annealing.

7.2 Summary of findings

7.2.1 Formation of DBs

A theory of DBs formation has been developed and validated by a CPFE model with experimental observations in single crystal, multi-crystal and polycrystalline aluminium. The formation of DBs is caused by the prohibition of the lattice sliding and the initiation of the lattice rotation due to the constraints from slip band intersection.

DBs are formed preferentially in grains whose primary slip field reaches to criteria. The value of the primary slip field has a strong positive correlation with the area fraction, aspect ratio (i.e. a/2c) and the density of formed DBs. The orientation in the DBs is found to become 'harder' since {111} slip planes in the DBs are found to become perpendicular to the loading direction during the plastic deformation.

7.2.2 Effect of DBs on recrystallization

The effect of DBs on the RX process in aluminium ranging from pure Al to commercial Al alloys has been summarised in this work. The DB is demonstrated to be a major source of orientations and potential positions for the nucleated grains, resulting in the eventual RXed texture.

It has been found that the initial grain nucleation prefers to occur inside of the DBs rather than grain boundaries in deformed Al alloys. The area fraction of DBs is found to have a positive correlation with the number of nucleated grains which contributes to the RX rate.

7.2.3 RX kinetics

Grain coarsening, impingement, recrystallized texture and grain structure can be accurately simulated by KWC phase-field model through revising the nucleation law according to experimental findings. KWC phase-field model coupled with CPFE model is able to quantify the incubation time of nucleated grains through identifying the favourable positions, critical stored energy and critical size.

7.3 Future works

7.3.1 Strain path effect on recrystallization

As mentioned for unsolved problems in Chapter 2, the strain path effect is an unsolved problem for the prediction and manipulation of the RXed microstructure of alloys during manufacturing. When one crystalline material is deformed by different processes, the resulting deformed microstructure and texture differ, thus, affecting the kinetics of the RX process.

Since the relation between deformed state and RX has been successfully established in this thesis, the problem of strain path effect on RX becomes investigating the impact of strain path on the deformed state. To avoid the uncertainties from the effect of the grain boundary, texture, grain morphology and precipitates, cubic single crystal pure Al samples with the same orientations can be deformed by different strain paths for this study, e.g. plane-strain compression, simple shear, multi-axis compression, etc., to the same true strain. The deformed microstructure and its RXed microstructure can be analysed in terms of dislocation structure and orientation distribution to understand the effect of strain path on RX.

7.3.2 Interaction of precipitates and DBs

The effect of precipitates on the formation of DBs, as well as the competition between precipitates and DBs on grain nucleation, are not discussed in this thesis, whereas most of the alloys in commercial use, such as aluminium alloys used for aeronautic and automobile

industry, contain precipitates to achieve high strength. These precipitates, demonstrated in previous literature [3], can affect the RX behaviour regarding the kinetics, the resulting grain size and texture.

Since it has been validated in this thesis that the existence of DBs is crucial for the RX in commercial aluminium alloys which not containing precipitates, the importance of DBs in the Al alloys containing precipitates needs to be examined in the future work for the practical use, as well as the scientific understanding.

References

[1]   K.G.F. Janssens, D. Raabe, E. Kozeschnik, M.A. Miodownik, B. Nestler, Computational materials engineering : an introduction to microstructure evolution, Elsevier / Academic Press, 2007.

[2]   K. Huang, K. Marthinsen, Q. Zhao, R.E. Logé, The double-edge effect of second-phase particles on the recrystallization behaviour and associated mechanical properties of metallic materials, Prog. Mater. Sci. 92 (2018) 284–359. doi:10.1016/j.pmatsci.2017.10.004.

[3]   F.J. Humphreys, M. Hatherly, Recrystallization and related annealing phenomena, Elsevier, 2004. doi:10.1016/B978-008044164-1/50014-1.

[4]   H. Hallberg, Approaches to modeling of recrystallization, Metals (Basel). 1 (2011) 16–48. doi:10.3390/met1010016.

[5]   D. Raabe, 23 - Recovery and Recrystallization: Phenomena, Physics, Models, Simulation, in: Elsevier, Oxford, 2014: pp. 2291–2397. doi:10.1016/B978-0-444-53770-6.00023-X.

[6]   A.D. Rollett, Overview of modeling and simulation of recrystallization, Prog. Mater. Sci. 42 (1997) 79–99. doi:10.1016/S0079-6425(97)00008-X.

[7]   P. Bate, Modelling deformation microstructure with the crystal plasticity finite-element method, Philos. Trans. R. Soc. A Math. Phys. Eng. Sci. 357 (1999) 1589–1601. doi:10.1098/rsta.1999.0391.

[8]   D. Raabe, R.C. Becker, Coupling of a crystal plasticity finite-element model with a probabilistic cellular automaton for simulating primary recrystallization in aluminium, Model. Simul. Mater. Sci. Eng. 8 (2000) 445–462. doi:10.1002/3527606157.ch1.

[9]   P.R. Rios, F. Siciliano, H. Ricardo, Z. Sandim, R.L. Plaut, A. Fernando Padilha, Nucleation and growth during recrystallization, Mater. Res. 8 (2005) 225–238. doi:10.1590/S1516-14392005000300002.

[10] B. Bay, N. Hansen, Recrystallization in Commercially Pure Aluminum, Metall. Trans. A. 15 (1984) 287–297. doi:10.1007/BF02645114.

[11] M. Miszczyk, H. Paul, J.H. Driver, C. Maurice, New orientation formation and growth during primary recrystallization in stable single crystals of three face-centred cubic metals, Acta Mater. 83 (2015) 120–136. doi:10.1016/j.actamat.2014.09.054.

[12] M.M.M. Miszczyk, H. Paul, J.H.H. Driver, P. Drzyma, P. Drzymała, Recrystallization nucleation in stable aluminium-base single crystals : Crystallography and mechanisms, Acta Mater. 125 (2017) 109–124. doi:10.1016/j.actamat.2016.11.054.

[13] K. Kashihara, M. Tagami, T. Okada, F. Inoko, Nucleation of recrystallized grains in multiple slipped structure without deformation band in aluminum single crystal, Mater. Sci. Eng. A. 291 (2000) 207–217. doi:10.1016/S0921-5093(00)00961-8.

[14] C.D. Barrett, A. Imandoust, A.L. Oppedal, K. Inal, M.A. Tschopp, H. El Kadiri, Effect of grain boundaries on texture formation during dynamic recrystallization of magnesium alloys, Acta Mater. 128 (2017) 270–283. doi:10.1016/J.ACTAMAT.2017.01.063.

[15] D. Guan, W.M. Rainforth, J. Gao, L. Ma, B. Wynne, Individual effect of recrystallisation nucleation sites on texture weakening in a magnesium alloy: Part 2-shear bands, Acta Mater. 145 (2018) 399–412. doi:10.1016/j.actamat.2017.12.019.

[16] P. Zhao, Y. Wang, S.R. Niezgoda, Microstructural and micromechanical evolution during dynamic recrystallization, Int. J. Plast. 100 (2018) 52–68. doi:10.1016/J.IJPLAS.2017.09.009.

[17] P. Zhao, T. Song En Low, Y. Wang, S.R. Niezgoda, An integrated full-field model of concurrent plastic deformation and microstructure evolution: Application to 3D simulation of dynamic recrystallization in polycrystalline copper, Int. J. Plast. 80 (2016) 38–55. doi:10.1016/J.IJPLAS.2015.12.010.

[18] X. Zhou, H. Zhang, G. Wang, X. Bai, Y. Fu, J. Zhao, Simulation of microstructure evolution during hybrid deposition and micro-rolling process, J. Mater. Sci. 51 (2016) 6735–6749. doi:10.1007/s10853-016-9961-0.

[19] T. Takaki, T. Hirouchi, Y. Hisakuni, A. Yamanaka, Y. Tomita, Multi-Phase-Field Model to Simulate Microstructure Evolutions during Dynamic Recrystallization, Mater. Trans. 49 (2008) 2559–2565. doi:10.2320/matertrans.MB200805.

[20] K. Adam, D. Zöllner, D.P. Field, 3D microstructural evolution of primary recrystallization and grain growth in cold rolled single-phase aluminum alloys, Model. Simul. Mater. Sci. Eng. 26 (2018). doi:10.1088/1361-651X/aaa146.

[21] D. Raabe, Multiscale recrystallization models for the prediction of crystallographic textures with respect to process simulation, J. Strain Anal. Eng. Des. 42 (2007) 253–268. doi:10.1243/03093247JSA219.

[22] Q. Luan, J. Lee, Z. Zheng, J. Lin, J. Jiang, Static recrystallization study on pure aluminium using crystal plasticity finite element and phase-field modelling, Procedia Manuf. 15 (2018) 1800–1807. doi:10.1016/j.promfg.2018.07.211.

[23] E. Popova, Y. Staraselski, A. Brahme, R.K. Mishra, K. Inal, Coupled crystal plasticity – Probabilistic cellular automata approach to model dynamic recrystallization in magnesium alloys, Int. J. Plast. 66 (2015) 85–102. doi:10.1016/J.IJPLAS.2014.04.008.

[24] W.R. Hibbard, W.R. Tully, The effect of orientation on the recrystallization kinetics of cold-rolled single crystals, AIME TRANS. 221 (1961) 336–343.

[25] R.D. Doherty, D.A. Hughes, F.J. Humphreys, J.J. Jonas, D.J. Jensen, M.E. Kassner, W.E. King, T.R. McNelley, H.J. McQueen, A.D. Rollett, Current issues in recrystallization: a review, Mater. Sci. Eng. A. 238 (1997) 219–274. doi:10.1016/S0921-5093(97)00424-3.

[26] F.J. Humphreys, Modelling mechanisms and microstructures of recrystallisation, Mater. Sci. Technol. 8 (1992) 135–144. doi:10.1179/mst.1992.8.2.135.

[27] P.A. Beck, P.R. Sperry, C.S. Smith, J.E. Burke, P.R. Sperry, C.S. Smith, J.E. Burke, Strain induced grain boundary migration in high purity aluminum, J. Appl. Phys. 21 (1950) 150–152. doi:10.1063/1.1699614.

[28] P.A. Beck, The Formation of Recrystallization Nuclei, J. Appl. Phys. 20 (1949) 633–634. doi:10.1063/1.1698446.

[29] R.W. Cahn, A New Theory of Recrystallization Nuclei, Proc. Phys. Soc. Sect. A. 63 (1950) 323–336. doi:10.1088/0370-1298/63/4/302.

[30] W. Boas, J.S. Bowles, The effect of crystal arrangement on " secondary recrystallization" in metals, J. Inst. Met. 74 (1947) 501–519.

[31] M. Hillert, On the theory of normal and abnormal grain growth, Acta Metall. 13 (1965) 227–238. doi:10.1016/0001-6160(65)90200-2.

[32] J. Friedel, Dislocations, Elsevier Science, 1964.

[33] C.S. Barrett, L.H. Levenson, Structure of iron after drawing, swaging and elongation in tension, Trans. Aime. 135 (1939) 327–352.

[34] I.L. Dillamore, P.L. Morris, C.J.E. Smith, W.B. Hutchinson, Transition Bands and Recrystallization in Metals, Proc. R. Soc. A Math. Phys. Eng. Sci. 329 (1972) 405–420. doi:10.1098/rspa.1972.0120.

[35] K. Higashida, J. Takamura, N. Narita, J. Takamurat, N. Narita, The Formation of Deformation Bands in f. c. c. Crystals, Elsevier, 1986. doi:10.1016/0025-5416(86)90266-1.

[36] D.M. Moon, W.H. Robinson, Dislocation distribution in deformed silver single crystals, Can. J. Phys. 45 (1967) 1017–1030. doi:10.1139/p67-074.

[37] J.W. Steeds, Dislocation arrangement in copper single crystals as a function of strain, Proc. R. Soc. London. Ser. A. Math. Phys. Sci. 292 (1966) 343–373. doi:10.1098/RSPA.1966.0139.

[38] P. Franciosi, M. Berveiller, A. Zaoui, Latent hardening in copper and aluminium single crystals, Acta Metall. 28 (1980) 273–283. doi:10.1016/0001-6160(80)90162-5.

[39] T.-Y. Wu, J.L. Bassani, C. Laird, Latent Hardening in Single Crystals I. Theory and Experiments, Proc. R. Soc. A Math. Phys. Eng. Sci. 435 (1991) 1–19. doi:10.1098/rspa.1991.0127.

[40] Q. Luan, H. Xing, J. Zhang, J. Jiang, Experimental and crystal plasticity study on deformation bands in single crystal and multi-crystal pure aluminium, Acta Mater. 183

(2020) 78–92. doi:10.1016/J.ACTAMAT.2019.11.006.

[41] J.R. Hirsch, Correlation of deformation texture and microstructure, Mater. Sci. Technol. 6 (1990) 1048–1057. doi:10.1179/mst.1990.6.11.1048.

[42] N. Jia, P. Eisenlohr, F. Roters, D. Raabe, X. Zhao, Orientation dependence of shear banding in face-centered-cubic single crystals, Acta Mater. 60 (2012) 3415–3434. doi:10.1016/j.actamat.2012.03.005.

[43] H. Paul, J.H. Driver, C. Maurice, A. Piątkowski, The role of shear banding on deformation texture in low stacking fault energy metals as characterized on model Ag crystals, Acta Mater. 55 (2007) 575–588. doi:10.1016/J.ACTAMAT.2006.08.051.

[44] W. Pfeiler, Investigation of short-range order by electrical resistivity measurement, Acta Metall. 36 (1988) 2417–2434. doi:10.1016/0001-6160(88)90192-7.

[45] O. Engler, Deformation and texture of copper–manganese alloys, Acta Mater. 48 (2000) 4827–4840. doi:10.1016/S1359-6454(00)00272-X.

[46] A. Duckham, R.. Knutsen, O. Engler, Influence of deformation variables on the formation of copper-type shear bands in Al–1Mg, Acta Mater. 49 (2001) 2739–2749. doi:10.1016/S1359-6454(01)00166-5.

[47] K. Lücke, O. Engler, Effects of particles on development of microstructure and texture during rolling and recrystallisation in fcc alloys, Mater. Sci. Technol. 6 (1990) 1113–1130. doi:10.1179/mst.1990.6.11.1113.

[48] J. Lin, Fundamentals of materials modelling for metals processing technologies : theories and applications, n.d.

[49] E. Lindh, B. Hutchinson, S. Ueyama, Effect of redundant deformation on recrystallisation behaviour of copper, Scr. Metall. Mater. 29 (1993) 347–352. doi:10.1016/0956-716X(93)90511-P.

[50] J.D. Embury, W.J. Poole, E. Koken, Some views on the influence of strain path on recrystallization, Scr. Metall. Mater. 27 (1992) 1465–1470. doi:10.1016/0956-716X(92)90129-3.

[51] A.N. Shiryayev, On The Statistical Theory of Metal Crystallization, in: Sel. Work. A. N. Kolmogorov, Springer Netherlands, Dordrecht, 1992: pp. 188–192. doi:10.1007/978-94-011-2260-3_22.

[52] W.A. Johnson, R.F. Mehl, Reaction kinetics in processes of nucleation and growth, Trans. Am. Inst. Min. Met. Eng. 135 (1939) 416–442.

[53] M. Avrami, Kinetics of Phase Change. I General Theory, J. Chem. Phys. 7 (1939) 1103. doi:10.1063/1.1750380.

[54] M. Avrami, Kinetics of Phase Change. II Transformation-Time Relations for Random Distribution of Nuclei, J. Chem. Phys. 8 (1940) 212. doi:10.1063/1.1750631.

[55] T. Takaki, A. Yamanaka, Y. Higa, Y. Tomita, Phase-field model during static recrystallization based on crystal-plasticity theory, J. Comput. Mater. Des. 14 (2007) 75–84. doi:10.1007/s10820-007-9083-8.

[56] L. Gránásy, T. Pusztai, J.A. Warren, S. Biswas, I. Samajdar, A. Haldar, A. Sain, Coarsening in polycrystalline material using quaternions, J. Phys. Condens. Matter. 23 (2011) 72202–5. doi:10.1088/0953-8984/23/7/072202.

[57] Y. Guan, B. Chen, J. Zou, T. Ben Britton, J. Jiang, F.P.E.E. Dunne, Crystal plasticity modelling and HR-DIC measurement of slip activation and strain localization in single and oligo-crystal Ni alloys under fatigue, Int. J. Plast. 88 (2017) 70–88. doi:10.1016/j.ijplas.2016.10.001.

[58] B. Chen, J. Jiang, F.P.E. Dunne, Is stored energy density the primary meso-scale mechanistic driver for fatigue crack nucleation?, Int. J. Plast. 101 (2018) 213–229. doi:10.1016/J.IJPLAS.2017.11.005.

[59] B. Chen, J. Jiang, F.P.E. Dunne, Microstructurally-sensitive fatigue crack nucleation in Ni-based single and oligo crystals, J. Mech. Phys. Solids. 106 (2017) 15–33. https://www.sciencedirect.com/science/article/pii/S0022509617301059 (accessed June 7, 2017).

[60] F.P.E. Dunne, R. Kiwanuka, A.J. Wilkinson, Crystal plasticity analysis of micro-deformation, lattice rotation and geometrically necessary dislocation density, Proc. R.

Soc. A Math. Phys. Eng. Sci. 468 (2012) 2509–2531. doi:10.1098/rspa.2012.0050.

[61]   R. Kobayashi, J.A. Warren, W.C. Carter, A continuum model of grain boundaries, Phys. D Nonlinear Phenom. 140 (2000) 141–150. doi:https://doi.org/10.1016/S0167-2789(00)00023-3.

[62]   M. Muramatsu, Y. Aoyagi, Y. Tadano, K. Shizawa, Phase-field simulation of static recrystallization considering nucleation from subgrains and nucleus growth with incubation period, Comput. Mater. Sci. 87 (2014) 112–122. doi:10.1016/j.commatsci.2014.02.003.

[63]   N. Moelans, B. Blanpain, P. Wollants, An introduction to phase-field modeling of microstructure evolution, Calphad Comput. Coupling Phase Diagrams Thermochem. 32 (2008) 268–294. doi:10.1016/j.calphad.2007.11.003.

[64]   K. Marthinsen, E. Nes, O. Daaland, T. Furu, The spatial distribution of nucleation sites and its effect on recrystallization kinetics in commercial aluminum alloys, Metall. Mater. Trans. A. 34 (2003) 2705–2715. doi:10.1007/s11661-003-0172-3.

[65]   M.. P. Anderson, D.. J. Srolovitz, G.. S. Grest, P.. S. Sahni, Computer simulation of grain growth—I. Kinetics, Acta Metall. 32 (1984) 783–791. doi:10.1016/0001-6160(84)90151-2.

[66]   M.P. Anderson, G.S. Grest, D.J. Srolovitz, Computer simulation of normal grain growth in three dimensions, Philos. Mag. Part B. 59 (1989) 293–329. doi:10.1080/13642818908220181.

[67]   E. Ising, Report on the theory of ferromagnetism, Zeitschrift Fur Phys. 31 (1925) 253–258.

[68]   R.B. Potts, C. Domb, G.H. Wannier, Some generalized order-disorder transformations, Math. Proc. Cambridge Philos. Soc. 48 (1952) 106. doi:10.1017/S0305004100027419.

[69]   H. Hallberg, M. Wallin, M. Ristinmaa, Modeling of continuous dynamic recrystallization in commercial-purity aluminum, Mater. Sci. Eng. A. 527 (2010) 1126–1134. doi:10.1016/j.msea.2009.09.043.

[70]   H. Hallberg, M. Wallin, M. Ristinmaa, Simulation of discontinuous dynamic

recrystallization in pure Cu using a probabilistic cellular automaton, Comput. Mater. Sci. 49 (2010) 25–34. doi:10.1016/j.commatsci.2010.04.012.

[71]   K.G.F. Janssens, Random grid, three-dimensional, space-time coupled cellular automata for the simulation of recrystallization and grain growth, Model. Simul. Mater. Sci. Eng. 11 (2003) 157. doi:10.1088/0965-0393/11/2/304.

[72]   A.D.D. Rollett, D. Raabe, A hybrid model for mesoscopic simulation of recrystallization, Comput. Mater. Sci. 21 (2001) 69–78. doi:10.1016/S0927-0256(00)00216-0.

[73]   O.M. Ivasishin, S.V. Shevchenko, N.L. Vasiliev, S.L. Semiatin, A 3-D Monte-Carlo (Potts) model for recrystallization and grain growth in polycrystalline materials, Mater. Sci. Eng. A. 433 (2006) 216–232. doi:10.1016/j.msea.2006.06.115.

[74]   P. Peczak, A Monte Carlo study of influence of deformation temperature on dynamic recrystallization, Acta Metall. Mater. 43 (1995) 1279–1291. doi:10.1016/0956-7151(94)00280-U.

[75]   A.D.D. Rollett, M.J.J. Luton, D.J.J. Srolovitz, Microstructural simulation of dynamic recrystallization, Acta Metall. Mater. 40 (1992) 43–55. doi:10.1016/0956-7151(92)90198-N.

[76]   D. Raabe, Cellular Automata in Materials Science with Particular Reference to Recrystallization Simulation, Annu. Rev. Mater. Res. 32 (2002) 53–76. doi:10.1146/annurev.matsci.32.090601.152855.

[77]   K. Nakashima, T. Nagai, K. Kawasaki, Scaling behavior of two-dimensional domain growth: Computer simulation of vertex models, J. Stat. Phys. 57 (1989) 759–787. doi:10.1007/BF01022831.

[78]   D. Weygand, Y. Brechet, J. Lepinoux, A Vertex Simulation of Grain Growth in 2D and 3D, Adv. Eng. Mater. 3 (2001) 67–71. doi:10.1002/1527-2648(200101)3:1/2<67::AID-ADEM67>3.0.CO;2-P.

[79]   S. Osher, J.A. Sethian, Fronts propagating with curvature-dependent speed: Algorithms based on Hamilton-Jacobi formulations, J. Comput. Phys. 79 (1988) 12–

49. doi:10.1016/0021-9991(88)90002-2.

[80] H.S. Ubhi, J. Parsons, N. Othen, S. Campbell, R. Poole, a Gholinia, In-situ EBSD Phase Transformation and Recrystallisation, J. Phys. Conf. Ser. 522 (2014) 12011. doi:10.1088/1742-6596/522/1/012011.

[81] I.L. Dillamore, C.J.E. Smith, T.W. Watson, Oriented nucleation in the formation of annealing textures in iron, Met. Sci. J. 1 (1967) 49–54. doi:10.1179/msc.1967.1.1.49.

[82] J. Lin, Fundamentals of Materials Modelling for Metals Processing Technologies, Imperial College Press, 2015. doi:10.1142/p951.

[83] L. Ying, T. Gao, M. Dai, P. Hu, Investigation of interfacial heat transfer mechanism for 7075-T6 aluminum alloy in HFQ hot forming process, Appl. Therm. Eng. 118 (2017) 266–282. doi:10.1016/j.applthermaleng.2017.02.107.

[84] M. Zouari, R. Logé, N. Bozzolo, In Situ Characterization of Inconel 718 Post-Dynamic Recrystallization within a Scanning Electron Microscope, Metals (Basel). 7 (2017) 476. doi:10.3390/met7110476.

[85] F. Di Gioacchino, J. Quinta da Fonseca, Plastic Strain Mapping with Sub-micron Resolution Using Digital Image Correlation, Exp. Mech. 53 (2013) 743–754. doi:10.1007/s11340-012-9685-2.

[86] J.B. Hess, C.S. Barrett, Structure and nature of kink bands in zinc, JOM. 1 (1949) 599–606. doi:10.1007/BF03398902.

[87] K. Mecke, C. Blochwitz, Saturation Dislocation Structures in Cyclically Deformed Nickel Single Crystals of Different Orientations, Cryst. Res. Technol. 17 (1982) 743–758. doi:10.1002/crat.2170170610.

[88] K. Hagihara, M. Yamasaki, M. Honnami, H. Izuno, M. Tane, T. Nakano, Y. Kawamura, Philosophical Magazine Crystallographic nature of deformation bands shown in Zn and Mg-based long-period stacking ordered (LPSO) phase Crystallographic nature of deformation bands shown in Zn and Mg-based long-period stacking ordered (LPSO) phase, (2014). doi:10.1080/14786435.2014.987843.

[89] Y. Yang, L. Wang, T.R. Bieler, P. Eisenlohr, M.A. Crimp, Quantitative Atomic Force

Microscopy Characterization and Crystal Plasticity Finite Element Modeling of Heterogeneous Deformation in Commercial Purity Titanium, Metall. Mater. Trans. A. 42 (2011) 636–644. doi:10.1007/s11661-010-0475-0.

[90] F.P.E. Dunne, Introduction to computational plasticity, Oxford University Press, Oxford ; New York, 2005.

[91] Y. Guo, D.M.M. Collins, E. Tarleton, F. Hofmann, J. Tischler, W. Liu, R. Xu, A.J.J. Wilkinson, T.B.B. Britton, Measurements of stress fields near a grain boundary: Exploring blocked arrays of dislocations in 3D, Acta Mater. 96 (2015) 229–236. doi:10.1016/J.ACTAMAT.2015.05.041.

[92] J. Jiang, T. Zhang, F.P.E. Dunne, T. Ben Britton, Deformation compatibility in a single crystalline Ni superalloy, Proc. R. Soc. A Math. Phys. Eng. Sci. 472 (2016) 20150690. doi:10.1098/rspa.2015.0690.

[93] F. Basson, J.H. Driver, Deformation banding mechanisms during plane strain compression of cube-oriented f.c.c. crystals, Acta Mater. 48 (2000) 2101–2115. doi:10.1016/S1359-6454(00)00042-2.

[94] K. Huang, R.E. Logé, A review of dynamic recrystallization phenomena in metallic materials, Mater. Des. 111 (2016) 548–574. doi:10.1016/j.matdes.2016.09.012.

[95] M.A. Sutton, W.J. Wolters, W.H. Peters, W.F. Ranson, S.R. McNeill, Determination of displacements using an improved digital correlation method, Image Vis. Comput. 1 (1983) 133–139. doi:10.1016/0262-8856(83)90064-1.

[96] F. Hild, S. Roux, Digital Image Correlation: from Displacement Measurement to Identification of Elastic Properties, Strain. 42 (2006) 69–80. doi:10.1111/j.1475-1305.2006.00258.x.

[97] Q. Luan, T.B.B. Britton, T.-S. Jun, Strain rate sensitivity in commercial pure titanium: The competition between slip and deformation twinning, Mater. Sci. Eng. A. 734 (2018) 385–397. doi:10.1016/j.msea.2018.08.010.

[98] H.J. Scheel, The Development of Crystal Growth Technology, in: Cryst. Growth Technol., John Wiley & Sons, Ltd, Chichester, UK, 2003: pp. 1–14.

doi:10.1002/0470871687.ch1.

[99]   GOM Correlate Professional V8 SR1 Manual Basic Inspection-3D Testing, 2015.
       www.gom.com (accessed July 31, 2019).

[100] L.. Kubin, A. Mortensen, Geometrically necessary dislocations and strain-gradient
       plasticity: a few critical issues, Scr. Mater. 48 (2003) 119–125. doi:10.1016/S1359-
       6462(02)00335-4.

[101] T. Zhang, D.M. Collins, F.P.E.E. Dunne, B.A. Shollock, Crystal plasticity and high-
       resolution electron backscatter diffraction analysis of full-field polycrystal Ni
       superalloy strains and rotations under thermal loading, Acta Mater. 80 (2014) 25–38.
       doi:10.1016/j.actamat.2014.07.036.

[102] K.P. Boyle, Latent Hardening in Copper and Aluminium Single Crystals, Mater. Sci.
       Forum. 495–497 (2005) 1043–1048. doi:10.4028/www.scientific.net/msf.495-
       497.1043.

[103] G. De Matteis, G. Brando, F.M. Mazzolani, Pure aluminium: An innovative material
       for structural applications in seismic engineering, Constr. Build. Mater. 26 (2012)
       677–686. doi:10.1016/j.conbuildmat.2011.06.071.

[104] L.M. Brown, Dislocation pile-ups, slip-bands, ellipsoids, and cracks, Mater. Sci. Eng.
       A. 400–401 (2005) 2–6. doi:10.1016/j.msea.2005.03.043.

[105] R.J. Asaro, Micromechanics of Crystals and Polycrystals, Adv. Appl. Mech. 23 (1983)
       1–115. doi:10.1016/S0065-2156(08)70242-4.

[106] Y. Guo, T.B. Britton, A.J. Wilkinson, Slip band-grain boundary interactions in
       commercial-purity titanium, Acta Mater. 76 (2014) 1–12.
       doi:10.1016/j.actamat.2014.05.015.

[107] S. Birosca, F. Di Gioacchino, S. Stekovic, M. Hardy, A quantitative approach to study
       the effect of local texture and heterogeneous plastic strain on the deformation
       micromechanism in RR1000 nickel-based superalloy, Acta Mater. 74 (2014) 110–124.
       doi:10.1016/j.actamat.2014.04.039.

[108] J. Jiang, J. Yang, T. Zhang, J. Zou, Y. Wang, F.P.E. Dunne, T.B. Britton,

Microstructurally sensitive crack nucleation around inclusions in powder metallurgy nickel-based superalloys, Acta Mater. 117 (2016) 333–344. doi:10.1016/j.actamat.2016.07.023.

[109] J. Jiang, F.P.E.E. Dunne, T. Ben Britton, Toward Predictive Understanding of Fatigue Crack Nucleation in Ni-Based Superalloys, Jom. 69 (2017) 863–871. doi:10.1007/s11837-017-2307-9.

[110] Q. Luan, J. Lee, J.-H. Zheng, C. Hopper, J. Jiang, Combining microstructural characterization with crystal plasticity and phase-field modelling for the study of static recrystallization in pure aluminium, Comput. Mater. Sci. (2019) 109419. doi:10.1016/J.COMMATSCI.2019.109419.

[111] Y. Guo, J. Schwiedrzik, J. Michler, X. Maeder, On the nucleation and growth of {11-22} twin in commercial purity titanium: In situ investigation of the local stress field and dislocation density distribution, Acta Mater. 120 (2016) 292–301. doi:10.1016/j.actamat.2016.08.073.

[112] Y. Guo, D.M. Collins, E. Tarleton, F. Hofmann, A.J. Wilkinson, T. Ben Britton, Dislocation density distribution at slip band-grain boundary intersections, Acta Mater. 182 (2020) 172–183. doi:10.1016/J.ACTAMAT.2019.10.031.

[113] D. Raabe, Scaling Monte Carlo kinetics of the Potts model using rate theory, Acta Mater. 48 (2000) 1617–1628. doi:10.1016/S1359-6454(99)00451-6.

[114] L. Madej, M. Sitko, K. Radwański, R. Kuziak, K. Radwanski, R. Kuziak, Validation and predictions of coupled finite element and cellular automata model: Influence of the degree of deformation on static recrystallization kinetics case study, Mater. Chem. Phys. 179 (2016) 282–294. doi:10.1016/j.matchemphys.2016.05.040.

[115] E.M. Lauridsen, H.F. Poulsen, S.F. Nielsen, D. Juul Jensen, Recrystallization kinetics of individual bulk grains in 90% cold-rolled aluminium, Acta Mater. 51 (2003) 4423–4435. doi:10.1016/S1359-6454(03)00278-7.

[116] W. Pantleon, Resolving the geometrically necessary dislocation content by conventional electron backscattering diffraction, Scr. Mater. 58 (2008) 994–997. doi:10.1016/J.SCRIPTAMAT.2008.01.050.

[117] J.W. Kysar, Y. Saito, M.S. Oztop, D. Lee, W.T. Huh, Experimental lower bounds on geometrically necessary dislocation density, Int. J. Plast. 26 (2010) 1097–1123. doi:10.1016/J.IJPLAS.2010.03.009.

[118] D. Juul Jensen, Growth rates and misorientation relationships between growing nuclei/grains and the surrounding deformed matrix during recrystallization, Acta Metall. Mater. 43 (1995) 4117–4129. doi:10.1016/0956-7151(95)00111-8.

[119] J.A. Warren, R. Kobayashi, A.E. Lobkovsky, W.C. Carter, Extending phase field models of solidification to polycrystalline materials, Acta Mater. 51 (2003) 6035–6058.

[120] R.E. Reed-Hill, R. Abbaschian, R. Abbaschian, Physical metallurgy principles, Van Nostrand New York, 1973.

[121] H. Jazaeri, F.J. Humphreys, Quantifying recrystallization by electron backscatter diffraction, J. Microsc. 213 (2004) 241–246. doi:10.1111/j.0022-2720.2004.01296.x.

[122] G. Gottstein, D.A. Molodov, L.S. Shvindlerman, D.J. Srolovitz, M. Winning, Grain boundary migration: misorientation dependence, Curr. Opin. Solid State Mater. Sci. 5 (2001) 9–14. doi:10.1016/S1359-0286(00)00030-9.

[123] Y. Huang, F.J. Humphreys, Measurements of grain boundary mobility during recrystallization of a single-phase aluminium alloy, Acta Mater. 47 (1999) 2259–2268. doi:10.1016/S1359-6454(99)00062-2.

[124] K.. Russell, Grain boundary nucleation kinetics, Acta Metall. 17 (1969) 1123–1131. doi:10.1016/0001-6160(69)90057-1.

[125] Y.S. Sato, H. Kokawa, Distribution of tensile property and microstructure in friction stir weld of 6063 aluminum, Metall. Mater. Trans. A. 32 (2001) 3023–3031. doi:10.1007/s11661-001-0177-8.

[126] D. Witkin, Z. Lee, R. Rodriguez, S. Nutt, E. Lavernia, Al–Mg alloy engineered with bimodal grain size for high strength and increased ductility, Scr. Mater. 49 (2003) 297–302. doi:10.1016/S1359-6462(03)00283-5.

[127] A.K. Ghosh, R. Raj, Grain size distribution effects in superplasticity, Acta Metall. 29

(1981) 607–616. doi:10.1016/0001-6160(81)90142-5.

[128] A.M. Korsunsky, D. Dini, F.P.E. Dunne, M.J. Walsh, Comparative assessment of dissipated energy and other fatigue criteria, Int. J. Fatigue. 29 (2007) 1990–1995. doi:10.1016/J.IJFATIGUE.2007.01.007.

[129] V.Y. Gertsman, S.M. Bruemmer, Study of grain boundary character along intergranular stress corrosion crack paths in austenitic alloys, Acta Mater. 49 (2001) 1589–1598. doi:10.1016/S1359-6454(01)00064-7.

[130] F. Bachmann, R. Hielscher, H. Schaeben, Texture Analysis with MTEX – Free and Open Source Software Toolbox, Solid State Phenom. 160 (2010) 63–68. doi:10.4028/www.scientific.net/SSP.160.63.

[131] M. Kassner, A case for Taylor hardening during primary and steady-state creep in alurniniurn and type 304 stainless steel, J. Mater. Sci. 25 (1990) 1997–2003.

[132] A. Arsenlis, D.. Parks, Crystallographic aspects of geometrically-necessary and statistically-stored dislocation density, Acta Mater. 47 (1999) 1597–1611. doi:10.1016/S1359-6454(99)00020-8.

[133] J. Cheng, S. Ghosh, A crystal plasticity FE model for deformation with twin nucleation in magnesium alloys, Int. J. Plast. 67 (2015) 148–170. doi:10.1016/j.ijplas.2014.10.005.

[134] P. Zhang, D. Balint, J. Lin, An integrated scheme for crystal plasticity analysis: Virtual grain structure generation, Comput. Mater. Sci. 50 (2011) 2854–2864. doi:10.1016/j.commatsci.2011.04.041.

[135] F. Djavanroodi, M. Daneshtalab, M. Ebrahimi, A novel technique to increase strain distribution homogeneity for ECAPed materials, Mater. Sci. Eng. A. 535 (2012) 115–121. doi:10.1016/j.msea.2011.12.050.

[136] M.J. Powell, T. Physics, S. Street, A direct search optimization method that models the objective and constraint functions by linear interpolation, in: Adv. Optim. Numer. Anal., Springer, 1994: pp. 51–67.

[137] K. Radwański, Application of FEG-SEM and EBSD Methods for the Analysis of the

Restoration Processes Occurring during Continuous Annealing of Dual-Phase Steel Strips, Steel Res. Int. 86 (2015) 1379–1390. doi:10.1002/srin.201400361.

[138] N. Peranio, Y.J. Li, F. Roters, D. Raabe, Microstructure and texture evolution in dual-phase steels: Competition between recovery, recrystallization, and phase transformation, Mater. Sci. Eng. A. 527 (2010) 4161–4168. doi:10.1016/j.msea.2010.03.028.

[139] N. Hansen, Hall–Petch relation and boundary strengthening, Scr. Mater. 51 (2004) 801–806. doi:10.1016/J.SCRIPTAMAT.2004.06.002.

[140] Z. Liu, R.O. Olivares, Y. Lei, C.I. Garcia, G. Wang, Microstructural characterization and recrystallization kinetics modeling of annealing cold-rolled vanadium microalloyed HSLA steels, J. Alloys Compd. 679 (2016) 293–301. doi:10.1016/j.jallcom.2016.04.057.

[141] A. Gloria, R. Montanari, M. Richetta, A. Varone, Alloys for Aeronautic Applications: State of the Art and Perspectives, Metals (Basel). 9 (2019) 662. doi:10.3390/met9060662.

[142] W. Li, Y. Liu, S. Jiang, Q. Luan, Y. Li, B. Gu, Z. Shi, A study of thermomechanical behaviour and grain size evolution of AA7050 under hot forging conditions, Int. J. Light. Mater. Manuf. (2018). doi:10.1016/J.IJLMM.2018.10.002.

[143] X. Wang, Q. Pan, L. Liu, S. Xiong, W. Wang, J. Lai, Y. Sun, Z. Huang, Characterization of hot extrusion and heat treatment on mechanical properties in a spray formed ultra-high strength Al-Zn-Mg-Cu alloy, Mater. Charact. 144 (2018) 131–140. doi:10.1016/J.MATCHAR.2018.07.012.

[144] H.E. Hu, L. Zhen, L. Yang, W.Z. Shao, B.Y. Zhang, Deformation behavior and microstructure evolution of 7050 aluminum alloy during high temperature deformation, Mater. Sci. Eng. A. 488 (2008) 64–71. doi:10.1016/J.MSEA.2007.10.051.

[145] S. Wang, J.R. Luo, L.G. Hou, J.S. Zhang, L.Z. Zhuang, Physically based constitutive analysis and microstructural evolution of AA7050 aluminum alloy during hot compression, Mater. Des. 107 (2016) 277–289. doi:10.1016/J.MATDES.2016.06.023.

[146] ASM International Committee, Heat Treating of Aluminum, ASM Handbook, Vol. 4 Heat Treat. 4 (1990) 841–879. doi:10.1361/asmhba000.

[147] G.W. Kuhlman, Forging of Aluminum Alloys, ASM Handbook, Vol. 14A Metalwork. Bulk Form. (2013) 299–312. doi:10.1361/asmhba0003996.

[148] J. Cao, Z. Sun, H. Wu, Z. Yin, L. Huang, Evolution law of continuous dynamic recrystallization in forming of AA7075 tee valve by multi-direction loading, Int. J. Light. Mater. Manuf. 2 (2019) 40–49. doi:10.1016/J.IJLMM.2018.10.004.

[149] S. Lei, W. Jiu-Ba, R. Chang, The Prediction of Microstructure Evolution of 6005A Aluminum Alloy in a P-ECAP Extrusion Study, J. Mater. Eng. Perform. 27 (2018) 2566–2575. doi:10.1007/s11665-018-3326-6.

[150] Y. Li, B. Gu, S. Jiang, Y. Liu, Z. Shi, J. Lin, A CDRX-based Material Model for Hot Deformation of Aluminium Alloys (under review), Int. J. Plast. (2020).

[151] J. Tarasiuk, P. Gerber, B. Bacroix, Estimation of recrystallized volume fraction from EBSD data, Acta Mater. 50 (2002) 1467–1477. doi:10.1016/S1359-6454(02)00005-8.

[152] T. Nagira, H. Yokota, S. Morita, H. Yasuda, M. Yoshiya, C.M. Gourlay, A. Sugiyama, K. Uesugi, K. Umetani, Characterization of Shear Deformation Based on In-situ Observation of Deformation in Semi-solid Al–Cu Alloys and Water-particle Mixture, ISIJ Int. 53 (2013) 1195–1201. doi:10.2355/isijinternational.53.1195.

[153] E.P. Busso, A continuum theory for dynamic recrystallization with microstructure-related length scales, Int. J. Plast. 14 (1998) 319–353. doi:10.1016/S0749-6419(98)00008-4.

[154] S.F.F. Medina, C.A.A. Hernandez, Modelling of the dynamic recrystallization of austenite in low alloy and microalloyed steels, Acta Mater. 44 (1996) 165–171. doi:10.1016/1359-6454(95)00154-6.

[155] T. Sakai, J.J. Jonas, Dynamic recrystallization - Mechanical and microstructural considerations, Acta Met. Mater. 32 (1984) 189–209.

[156] M.L. Chiesa, A.A. Brown, B.R. Antoun, J.T. Ostien, R.A. Regueiro, D.J. Bammann, N.Y. Yang, Prediction of Final Material State in Multi-Stage Forging Processes, in:

AIP Conf. Proc., AIP, 2004: pp. 510–515. doi:10.1063/1.1766576.

[157] C.. M. Sellars, Q. Zhu, Microstructural modelling of aluminium alloys during thermomechanical processing, Mater. Sci. Eng. A. 280 (2000) 1–7. doi:10.1016/S0921-5093(99)00648-6.

[158] E. Ising, Beitrag zur Theorie des Ferromagnetismus, Zeitschrift Für Phys. 31 (1925) 253–258. doi:10.1007/BF02980577.

[159] M. Miodownik, E.A. Holm, G.N. Hassold, Highly parallel computer simulations of particle pinning: Zener vindicated, Scr. Mater. ol.42 (2000) 1173–1177.

[160] A. Harun, E. Holm, M. Clode, M. Miodownik, On computer simulation methods to model Zener pinning, Acta Mater. 54 (2006) 3261–3273. doi:10.1016/j.actamat.2006.03.012.

[161] J.A. Glazier, M.P. Anderson, G.S. Grest, Coarsening in the two-dimensional soap froth and the large- Q Potts model: A detailed comparison, Philos. Mag. Part B. 62 (1990) 615–645. doi:10.1080/13642819008215259.

[162] D. Raabe, F. Roters, Z. Zhao, A Texture Component Crystal Plasticity Finite Element Method for Physically-Based Metal Forming Simulations Including Texture Update, Mater. Sci. Forum. 396–402 (2002) 31–38. doi:10.4028/www.scientific.net/MSF.396-402.31.

[163] I. Kimber, C. Humphris, C. Westmoreland, N. Alepee, G.D. Negro, I. Manou, Computational materials engineering : an introduction to microstructure evolution, J. Appl. Toxicol. 31 (2011) 206–209. doi:10.1002/jat.1666.

Appendix A. Experimental characterisation methods

A.1 EBSD analysis for RX

The EBSD image parameters that can be used to characterise RX phenomenon are image/pattern quality (IQ), confidence index (EDAX), kernel average orientation (KAM), grain average misorientation (GAM), grain orientation spread (GOS) and grain reference orientation deviation (GROD).

A.1.1 Image quality

The image/pattern quality [151] is a measure of the quality (clarity) of diffraction patterns and is strongly affected by the degree of lattice imperfection caused by deformation [137]. One conventional parameter (IQ) used to describe the pattern quality is based on the Hough transform for indexing Kikuchi lines. The defects in crystal lattice such as dislocations, grains, and subgrain boundaries show a distorted pattern of Kikuchi lines resulting in lower values of IQ parameter [137]. Hence, the low value of IQ is located in the area with a high concentration of strain and grain boundaries. The high value of IQ is located at the dislocation-free recrystallized grains. The deconvolution of the IQ parameter is used to determine the fraction of recrystallized grains. An example is shown in Reference [137].

A.1.2 Confidence index

The confidence index (CI) is based on the automated indexing of the diffraction pattern. It was calculated using a voting scheme of software if multiple solutions exist. The equation is given by

$$CI = \frac{V_1 - V_2}{V_{ideal}}$$

(32)

where V_1 is the vote for solution 1, V_2 is the vote for solution 2 and V_{ideal} is the total available votes for detected bands.

A.1.3 Kernel average misorientation

The Kernel average misorientation (KAM) is an average misorientation of point with all its neighbours, i.e. a measure of local deviations in orientation. This value makes a clear difference visible between rolled and recrystallized area. In Reference [140], the yellow or red regions on the KAM map represent the grains having high KAM values and hence high dislocation density whereas the green or blue regions represent the grains having low KAM values and hence low dislocation density. The areas with KAM values less than the threshold value are recognised as new deformation-free, recrystallized grains. The KAM threshold ranges from $0.5°$ to $1.0°$ in the studies of recrystallization of steels [140]. Through measuring the fraction of blue regions in the KAM distribution map, the volume fraction of RX in the deformed sample can be quantitatively determined.

For the given pixel, KAM is defined by as follows [137]

$$KAM(j) = \left[\frac{1}{K}\right]\sum_k \omega_{jk} \tag{33}$$

where K is the number of pixels around the pixel j, ω_{jk} is the misorientation angle between the pixel j and k.

A.1.4 Grain reference orientation deviation

The grain reference orientation deviation is the deviation of each point's orientation from some reference value for the grain. The reference orientation can be average orientation (GROD-AO) for grain or orientation of point with minimum Kernel average misorientation (GROD-LK).

A.1.5 Grain average misorientation

The GAM parameter expresses the average misorientation between points inside one grain [137]. It is calculated as follows for the grain i:

$$GAM(j) = \left[\frac{1}{J(i)}\right]\sum_j KAM_j \tag{34}$$

where $J(i)$ is the number of pixels in the grain i.

A.1.6 Grain orientation spread

The GOS parameter represents the average misorientation of all points in particular grains [137,138]. It is calculated as

$$GOS(i) = \left[\frac{1}{J(i)}\right]\sum_j \omega_{ij} \tag{35}$$

where $J(i)$ is the number of pixels in grain i, ω_{jk} is the misorientation angle between the orientation of pixel j and the average orientation of the grain i. The GOS parameter for recrystallized grains is assumed to be less than 1.5˚ [114,137,138]. The high value of KAM and GOS represents a high variability of orientation indicating a high density of geometrically necessary dislocations (GNDs) [137,138].

A.2 Digital image correlation (DIC)

Digital image correlation (DIC) technique enables the measurement of full-field, in-plane strain distribution and the identification of shear bands during plastic deformation. This would provide a direct validation of the simulation tools, particularly the crystal plasticity modelling, for the prediction of the deformed microstructure [57,59].

DIC is a technique to measure the components of in-plane strains by tracing the movement of photocopier particles during deformation. Displacement vectors can be output by using the "differential" method from every correlation. This method is useful to solve the solid particle movement, the increment of displacement and strain field [152].

Appendix B. Existing models for RX

B.1 Continuum mechanical model

The continuum mechanical models describe the deformation history by use of internal variables which are related to the accumulated plastic deformation and the macroscopic deformation hardening of the material. The internal variables also can represent other homogenized quantities, such as the dislocation density and the grain size [4].

For this approach, the macroscopic properties, such as flow stress behaviour and strain-rate dependence, are linked to average properties of the evolving microstructure. The macroscopic flow stress σ_y will be related to the average grain size d following the Hall-Petch effect:

$$\sigma_y \propto \frac{1}{\sqrt{d}} \tag{36}$$

During the plastic deformation, the dislocation density ρ_d can be considered as a deformation hardening. This is described by

$$\sigma_y \propto \sqrt{\rho_d} \tag{37}$$

The dislocation density is also influenced by the recrystallization process besides plastic deformation, as the newly nucleated grains contain lower stored energy. Furthermore, with the decrease of grain size, the amount of grain boundary area increases resulting in restricted mobility of dislocations and dislocation accumulation [4].

a) Criteria for the recrystallization initiation

In some phenomenological continuum mechanical models of DRX, the condition for initiation of recrystallization is shown as follows

$$\varepsilon_{\text{eff}}^{\text{P}} \geq \varepsilon_c^P \tag{38}$$

The macroscopic critical plastic strain ε_c^P corresponds to the microscopic critical dislocation density. Hallberg et al. used these criteria in a finite strain, a visco-plastic, constitutive model of recrystallization in commercial-purity aluminium [69]. Reference [153–155] also used these

criterion in relation to analytical models and experimental results of RX.

For SRX, the dislocation density was considered by Chiesa et al. in 2004 as an internal variable related to the isotropic hardening of the material [156]. The variable is defined as a temperature-dependent critical threshold value.

b) Recrystallized grain size

An evolution equation for the subgrain size δ can be calculated from

$$\dot{\delta} = g(\delta)\dot{\varepsilon}_{\text{eff}}^{\text{P}} \tag{39}$$

where $g(\delta)$ is a function of the current value of the subgrain size, i.e., the spacing between dislocation walls.

The present amount of grain boundary area per unit volume $s_{\text{V}}(d_0, \varepsilon_{\text{eff}}^{\text{P}})$ is defined as a function of initial grain size and plastic deformation strain. Hence, the recrystallization nuclei density per unit volume can be calculated as follows, if nucleation is assumed to only occur at grain boundaries:

$$n_{\text{V}} = \left(\frac{c_{\text{n}}}{\delta^2}\right) s_{\text{V}}(d_0, \varepsilon_{\text{eff}}^{\text{P}}) \tag{40}$$

where parameter c_{n} is related to the probability of the presence of subgrains that are large enough for the constitution of nucleation sites for recrystallization.

The recrystallized grain size is then approximated under the assumption of site-saturated nucleation from a relation below

$$d = c_{\text{d}}(n_{\text{V}})^{-1/3} \tag{41}$$

where c_{d} is a parameter [4,157]. This approach involves an evolution law of the subgrain misorientation, taking the misorientation as an average quantity [4].

B.2 Monte Carlo Potts model

The Monte Carlo method was firstly used in solid-state physics to model ferromagnetic materials. The magnetization is represented by two states of spins: up and down. This type of model is known as the Ising model (1925) [158]. In 1952, Potts et al. generalised the Ising model allowing Q-states for each spin [68]. The Monte Carlo Potts model was also used to

investigate Zener pinning or particle pinning in Reference [159] and [160]. In 1984, Anderson et al. firstly introduced the Potts model to simulate the grain growth kinetics and to investigate grain size distribution and topology in two dimensions [65]. Anderson et al. then extended the algorithm to study three-dimensional grain growth in1989 [66].

The initial microstructure has to be mapped on to the grid of N discrete lattice sites. Each site i is given an index s_i and the sites in the same grain have a common index. Figure B1 is a schematic of a grain structure [4]. Additional parameters, such as crystallographic orientation and dislocation density, can be assigned to the index value of each lattice site representing the physical state of the site.

Figure B1 *A schematic of a 2D grain structure mapped onto a square lattice, showing orientation numbers at each site and grain boundaries between sites with unlike orientation* [4].

The total energy term of the analysis domain, *E,* is calculated from

$$E = \sum_{i=1}^{N} \left(\sum_{j=1}^{n} \frac{1}{2} \gamma(s_i, s_j) + E_s(s_i) \right) \tag{42}$$

where n is the number of neighbouring lattice sites for each individual site i. $E_s(s_i)$ is the stored energy related to the dislocation density at site i and the boundary energy $\gamma(s_i, s_j)$ is a function of the lattice index of present site i and neighbour site j. Because the boundary energy is a function of the relative crystallographic misorientation across the boundary. The energy terms are in the units of the Boltzmann constant k.

The evolution of the microstructure is obtained by employing a Monte Carlo sampling of lattice states, i.e. picking a random site and a new orientation at random from the set of allowable values. The change in total energy ΔE for reorienting the site is computed from Equation (42) according to the change of spin state from the origin to another of Q possible spins.

Accepting or rejecting the switch of a spin state depends on a switching probability $\omega_{\text{switch}}(\Delta E)$. The simplified equation is expressed as

$$\omega_{\text{switch}}(\Delta E) = \begin{cases} \omega_0 & \text{if} \quad \Delta E < 0 \\ \frac{1}{2}\omega_0 & \text{if} \quad \Delta E = 0 \\ 0 & \text{if} \quad \Delta E > 0 \end{cases} \tag{43}$$

The problem of this method is that the grain microstructure will be influenced by the underlying lattice, possibly resulting in an undesired faceting of the modelled grain boundaries. The grain boundary kinetics could also be influenced. There are several remedies for this problem: One choice is extending the set of neighbouring sites instead of considering only the nearest sites. Another choice is to consider other lattice arrays such as changing the square lattice to triangular lattice. A third choice is to set the simulation temperature $T_s > 0$ that will serrate the boundaries and a proper simulation temperature can result in equiaxed grains and correct RX kinetics [4].

The Monte Carlo Potts method is lack of length and time scales. Here are two approaches attempting to solve this issue. One option is to map the real microstructure onto the simulation lattice for a matching length scale, then, the simulation is executed until a certain microstructure is achieved which is comparable to the one from experiments. The simulation time can be calibrated against the physical experimental time for reaching the same microstructure [4,161]. Another option is to interpret the parameters of the Monte Carlo Potts model by physical quantities as in Reference [113], leading to correct units to the simulation results. This model can be calibrated and validated by the classical JMAK theory.

B.3 Cellular automata

Cellular automata are 2D or 3D analysis allowing for the simulation of both spatial and temporal evolution of microstructures. The analysis domain is divided into a grid of sub-

regions, i.e. the cells. For each cell, a set of state variables that define the physical state is assigned. The simulation step can be regarded as a time step, identifying a neighbourhood of each cell. The state switching rules are defined in this method to determine the updated state of each cell based on the previous state of the cell and the states of cells in the neighbourhood. These switching rules could be deterministic or probabilistic, based on the probability criterion [71].

The cellular automaton algorithm is very amenable for efficient parallelization, providing excellent scalability. At the begin of the simulation, the cell state variables including the dislocation density, crystallographic orientation and some identification flags are given to define the initial microstructure. The initial state of the cell can be obtained through simulations, e.g. based on crystal plasticity simulations [162] or experimentally measured data from samples. The grain microstructure represented by cells is constituted of different grains. A schematic of a grain boundary in the cellular automata is shown in Figure B2.
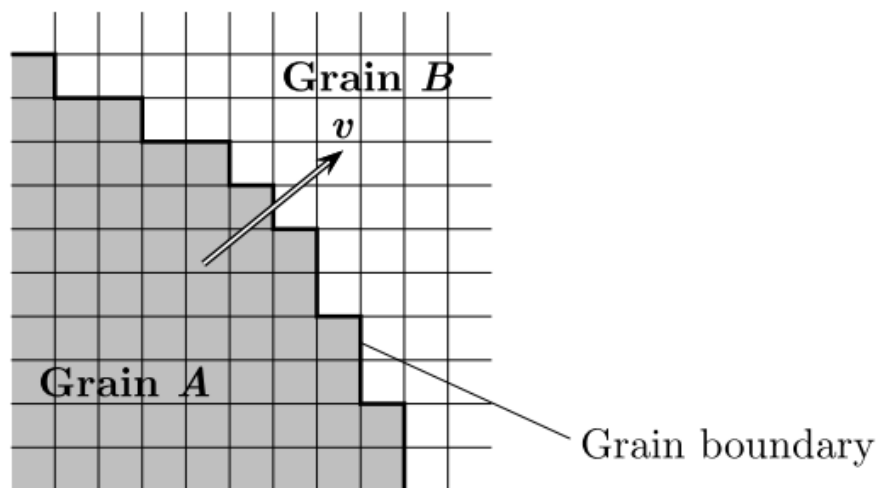

Figure B2 *Schematic of a grain boundary between grain A and grain B in cellular automata. The local boundary velocity v is pointed.*

The grain boundary conditions along the edges of microstructure for cellular automata domain could be periodic, symmetric and mirror boundary [70]. The approach [72] to obtain the microstructural evolution can be achieved by considering a local switching probability ω_{switch} same as that in Equation (43) for the Monte Carlo Potts model.

The probability can be calculated based on the velocity of approaching grain boundary to its neighbour cell as following

$$\omega_{\text{switch}} = \frac{v}{v_{max}} \text{ where } v \leq v_{max} \tag{44}$$

where v is the local grain boundary velocity and v_{max} is the maximum velocity in the analysis domain for the present time step. In each solution step, a random number $\xi \in [0, 1]$ is generated and the switch is accepted if $\xi \leq \omega_{\text{switch}}(\Delta E)$. Cellular automata for RX modelling are discussed in the book [163] and the review paper [76].

B.4 Vertex model

In most current vertex models, a two-dimensional grain structure has been considered. The geometry is represented by grain boundaries, i.e. the line segments shown in Figure B3. The line segments are connected at nodes which are triple (in 2D) and quadruple (in 3D) junctions and possibly at intermediate positions along grain boundaries. Therefore, the grain structure can be defined by the position x of nodes and their velocities **v** [4].
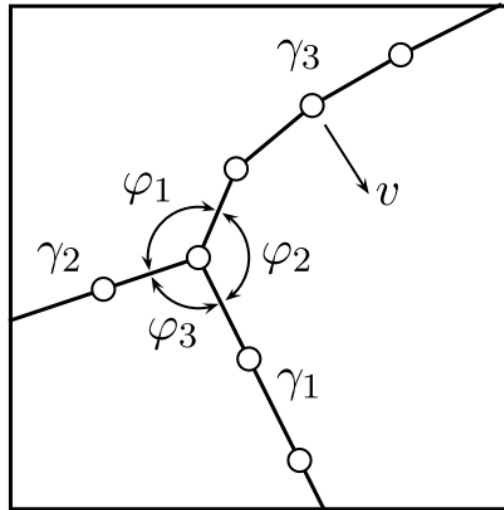

Figure B3 *Schematic of vertex model of a triple junction (in 2D) between three-grain boundaries with the interface energies $\gamma_1, \gamma_2, \gamma_3$ and the separation angles $\varphi_1, \varphi_2, \varphi_3$. Nodes are represented by circles and local velocity **v** of a node is shown in figure* [4].

As the notation in F, where γ_i are the grain boundary energies, the equilibrium separation angles φ_i of each grain can be calculated from the relation below:

$$\frac{\gamma_1}{\sin\varphi_1} = \frac{\gamma_2}{\sin\varphi_2} + \frac{\gamma_3}{\sin\varphi_3} \tag{45}$$

The grain migration is a dissipation process based on the grain boundary segment of two vertices, the grain boundary energy is given by

$$C(\mathbf{x}) = \int_a \gamma \, da \tag{46}$$

The dissipation is given by

$$R(\mathbf{x}, \mathbf{v}) = \int_a \frac{v^2}{m} \, da \tag{47}$$

where v is the local grain boundary velocity, m is grain boundary mobility, γ is the grain boundary energy. To calculate the integral of grain boundary energy and dissipation, a segment between the points $\mathbf{x}_i$ and $\mathbf{x}_j$ is denoted by an index ij with a grain boundary mobility $m_{i,j}$ and a grain boundary energy γ_{ij}. The boundary segment will have a related normal vector $\mathbf{n}_{ij}$. Therefore, the integrals of Equation 46 and 47 which is the sum of all boundary segments are given by

$$C = \frac{1}{2} \sum_{i=1}^{N} \sum_{j}^{(i)} \gamma_{ij} \|\mathbf{x}_{ij}\|$$

$$R = \frac{1}{6} \sum_{i-1}^{N} \sum_{j}^{(i)} \frac{\|\mathbf{x}_{ij}\|}{m_{ij}} \left[(\mathbf{v}_i \mathbf{n}_{ij})^2 + (\mathbf{v}_j \mathbf{n}_{ij})^2 + (\mathbf{v}_i \mathbf{n}_{ij})(\mathbf{v}_j \mathbf{n}_{ij}) \right] \tag{48}$$

where $\sum_{j}^{(i)}$ is applied for all j segments that are connected at vertex i, N is the total number of vertices in the model. The dependence of grain boundary energy and dissipation on many factors, such as the crystallographic misorientation can be included in Equation 48. The motion for a single vertex k can be obtained from

$$\frac{\partial C}{\partial \mathbf{x}_k} + \frac{\partial R}{\partial \mathbf{v}_k} = 0, \quad k = 1 \dots N \tag{49}$$

The velocities of the vertices are obtained from Equation 49, allowing the calculation of new positions of vertices through

$$\mathbf{x}_k(t + \Delta t) = \mathbf{x}_k(t) + \mathbf{v}_k(t)\Delta t, \quad k = 1 \dots N \tag{50}$$

where Δt is the time step. The time step should be scaled with the size of microstructure, i.e. grain size. The maximum allowable time step is favourable, as the time step could be computationally expensive [4].

B.5 Level set model

Compared with cellular automata and Monte Carlo Potts models, the level set models for recrystallization is recently developed. The main concept of this method is to trace the position of a moving interface $\Gamma(t)$ with time. The continuous function $\phi(\mathbf{x}, t)$ is introduced to represent the interface position with respect to space and time. The interface $\Gamma(t)$ is represented as the zero sets of $\phi(\mathbf{x}, t)$ [4]. The $\phi(\mathbf{x}, t)$ is expressed as

$$\begin{cases} \phi(\mathbf{x}, t) > 0 & if \quad \mathbf{x} \ is \ inside \quad \Gamma(t) \\ \phi(\mathbf{x}, t) = 0 & if \quad \mathbf{x} \ is \ at \quad \Gamma(t) \\ \phi(\mathbf{x}, t) > 0 & if \quad \mathbf{x} \ is \ outside \quad \Gamma(t) \end{cases} \tag{51}$$

The motion of the interface, $\Gamma(t)$, is expressed as

$$\frac{\partial \phi}{\partial t} + \mathbf{v} \nabla \phi = 0 \quad given \quad \phi(\mathbf{x}, t = 0) \tag{52}$$

where $\mathbf{v}$ is the interface velocity, corresponding to the scalar grain boundary velocity v. At any time t, the location of the interface (i.e. grain boundary) is given by $\phi(\mathbf{x}, t) = 0$.

For the microstructure with several grains, each grain i is set with an independent level set function $\phi(\mathbf{x}, t)$. The nucleated new grains are added bu introducing additional level set functions. Each level set function evolves separately during a time step in the solution.

An additional correction or smoothing step is employed at the end of each time step for avoiding the overlapping domains or voids between grain boundaries. The corrected level set function, $\phi_i^{corr.}(\mathbf{x}, t)$, is given by

$$\phi_i^{corr.}(\mathbf{x}, t) = \frac{1}{2}\left[\phi_i(\mathbf{x}, t) - \max_{i \neq j}(\phi_j(\mathbf{x}, t))\right] \tag{53}$$

The unit normal to the grain boundary is given by

$$\mathbf{n} = -\frac{\nabla \phi}{\|\nabla \phi\|} \qquad (54)$$

The curvature κ is given by

$$\kappa = -\nabla \mathbf{n} \qquad (55)$$
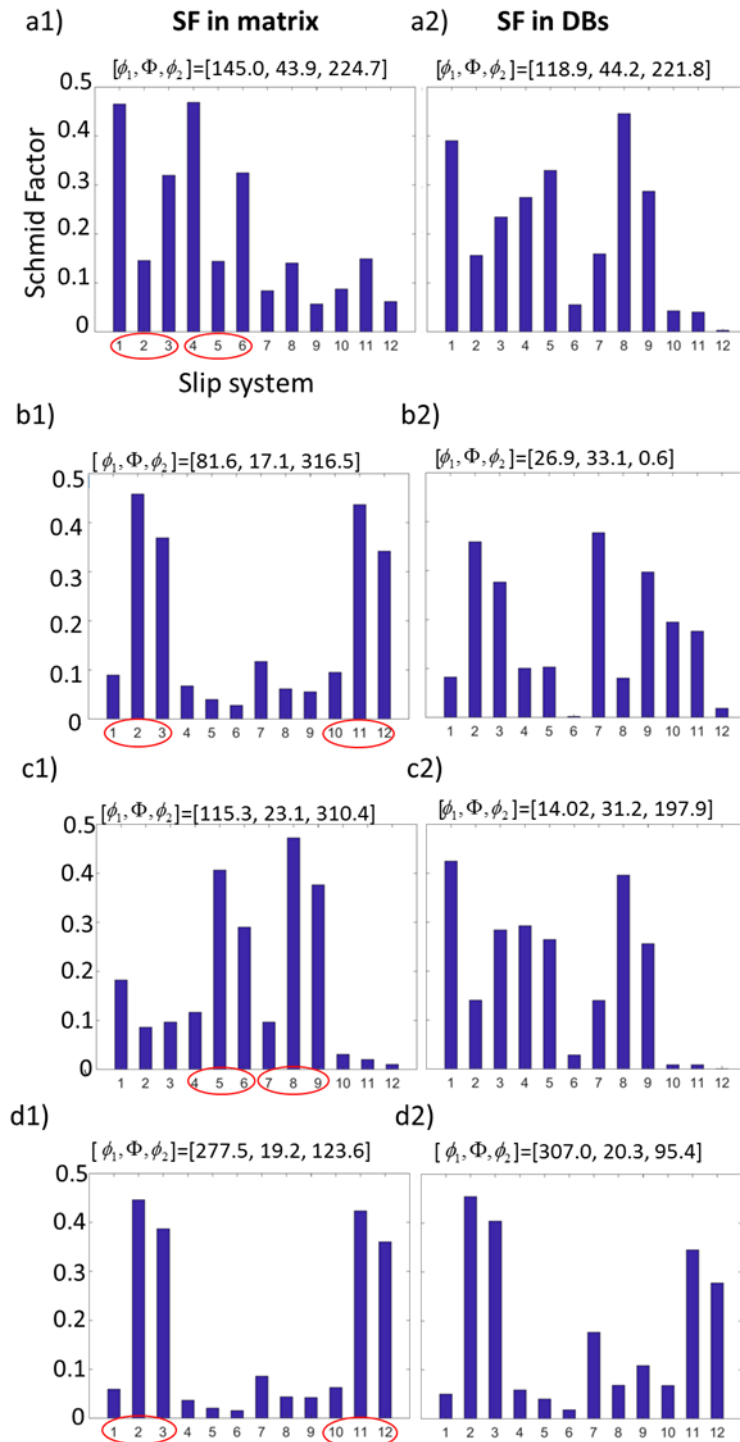
Appendix C. Additional figures

Figure C1 *a1)-d1) are the calculation of Schmid factors for grain orientations of SC I, II, III and IV in the deformed matrix. The most easily activated two slip planes are circled. a2)-d2) are the Schmid factors of 12 slip systems for the orientation in DBs.*
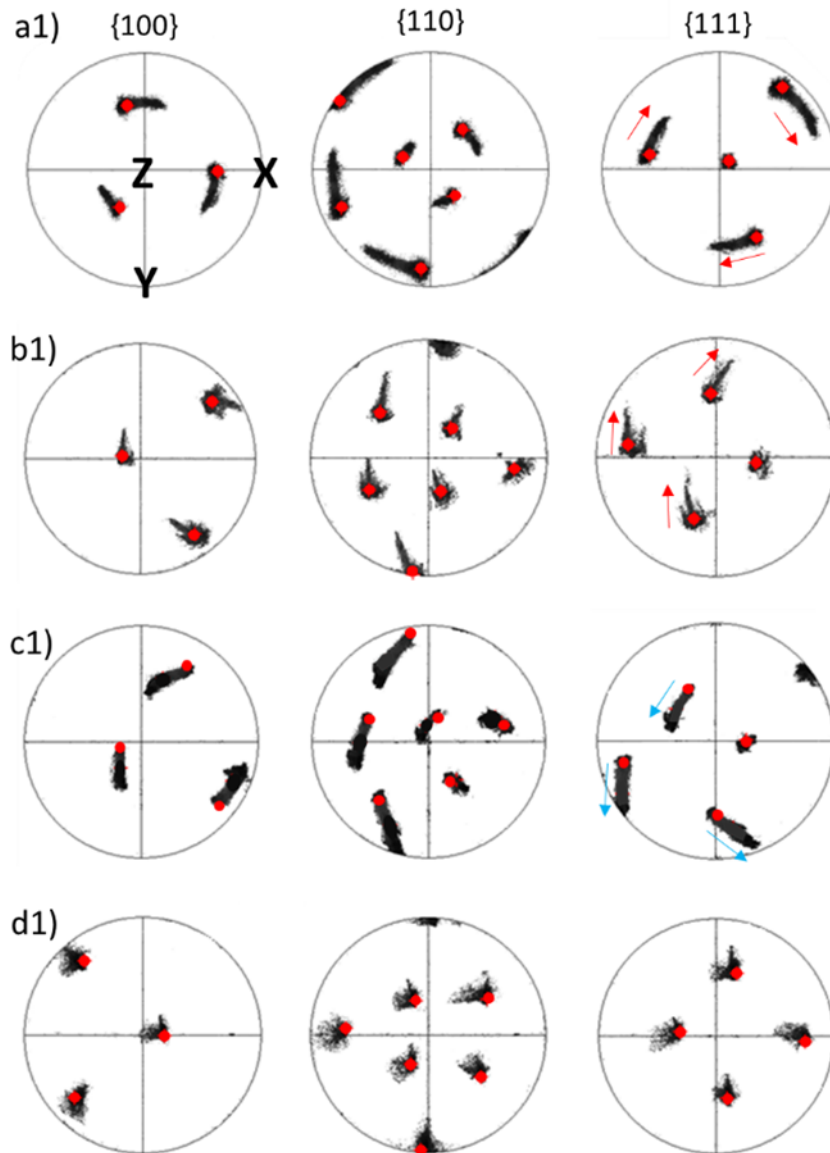
Figure C2 *Pole figures of deformed single crystal I-IV. Red dots show the orientation before compression. Red arrows represent the clockwise rotation and blue arrows represent anti-clockwise rotation around Z-axis.*
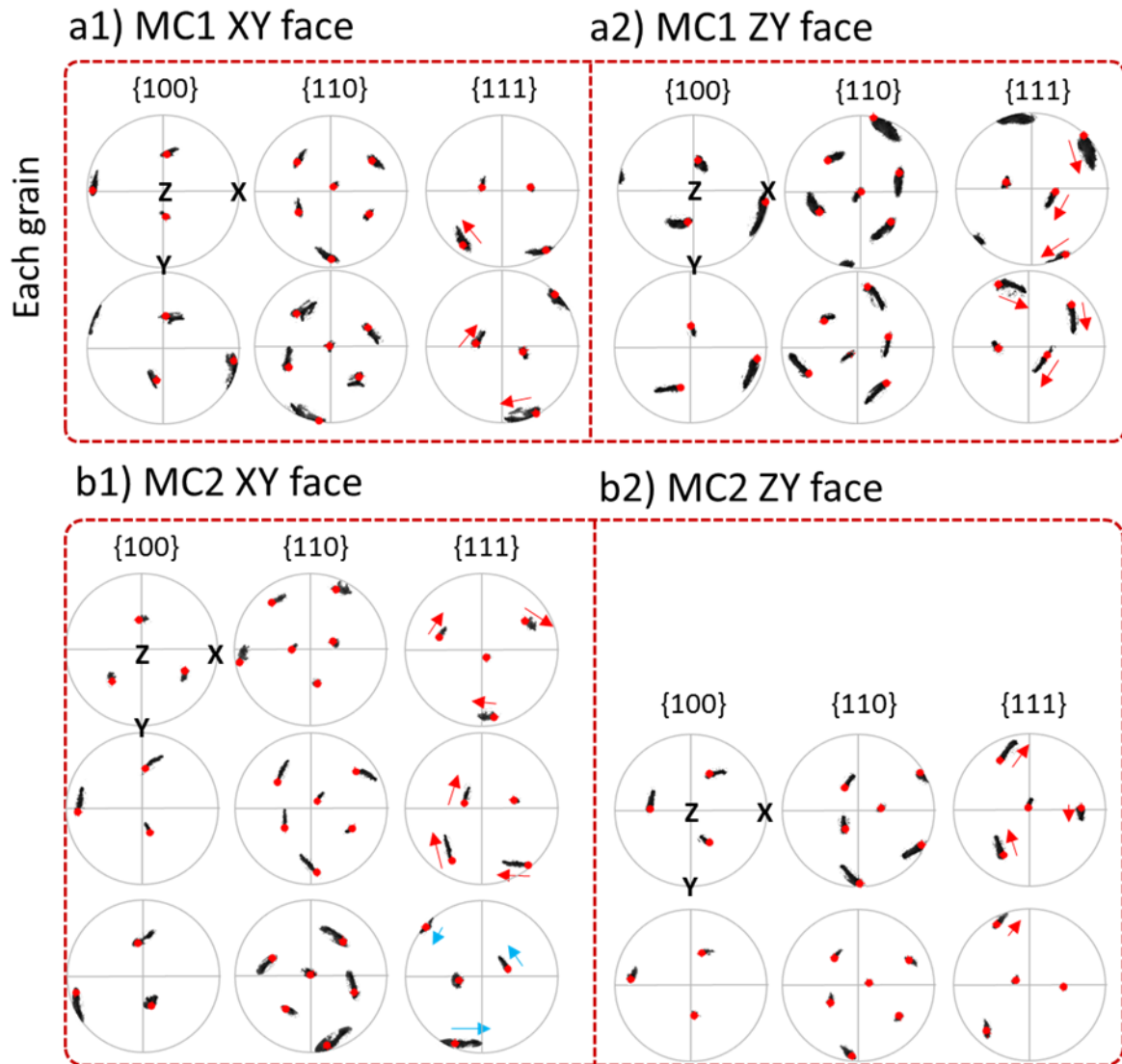
Figure C3 *a1)-a2) and b1)-b2) are PF of each grain in the front and side face of deformed samples. Red dots in PF show the orientation of each grain before compression. Red and blue arrows indicate the clockwise and anti-clockwise rotation of crystal orientation around z-axis during deformation.*
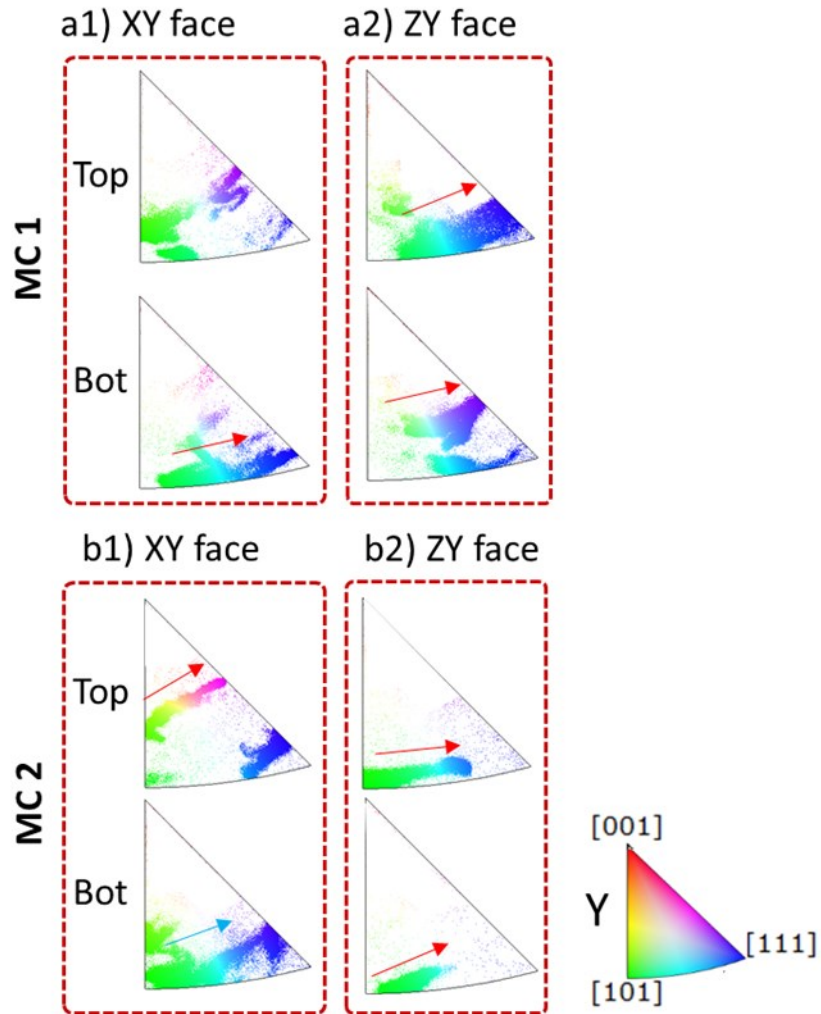
Figure C4 *a1)-a2) and b1)-b2) are the IPF-Y of front and side face on deformed MC 1 and 2. The top and bottom parts are split for the IPF plotting of each face. Colours are consistent with the IPF-Y maps shown in Figure 27.*
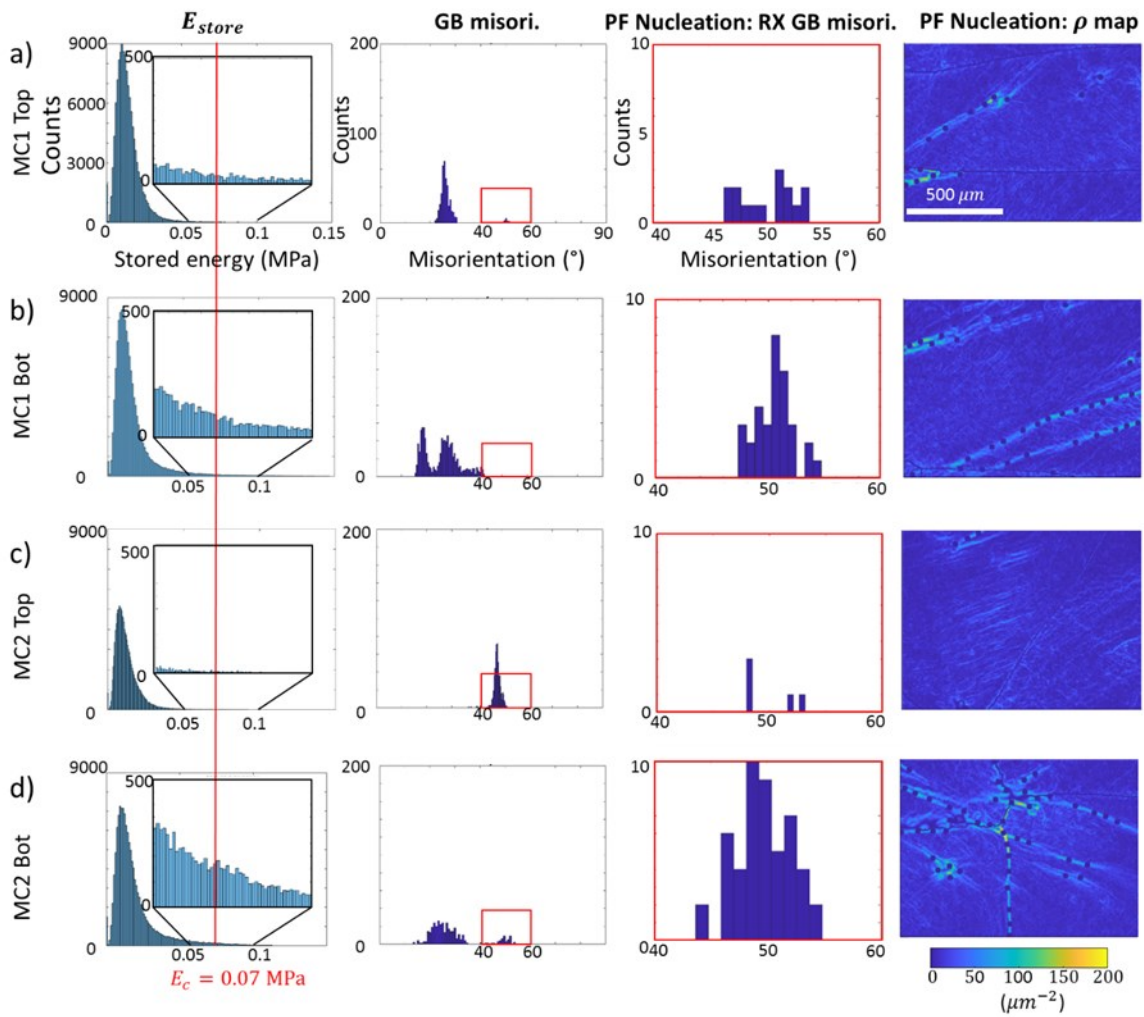
Figure C5 *Schematics to show how grain nucleation conditions applied for the XY faces of deformed MC1 and MC2. The 1ˢᵗ-row shows the stored energy distribution of deformed specimens; 2ⁿᵈ-row shows the misorientation distributions calculated based on EBSD maps; 3ʳᵈ-row shows the misorientation distribution of the simulated nucleated grains following the Gaussian distribution law; 4ᵗʰ-row is the GND distributions after seeding to show the seeding positions.*